

# **Complexation Properties of Upper- and Lower-rim Functionalized Calix[4]arenes**

By

**© Yousif Assiri**

A thesis submitted to the School of Graduate Studies  
in partial fulfillment of the requirement for the degree of  
Master of Science in Chemistry

Department of Chemistry  
Memorial University of Newfoundland  
November, 2014

St. John's

Newfoundland and Labrador

***Dedication***

*To the memory of my late Father*

*To my Mother*

*To my Wife Bashair Alasmari*

*To my Son Mohammad*

*And to all members of my family*

## Abstract

The work described in this thesis is concerned mainly with a study of the complexation properties of some new molecular receptors, which were synthesized by Dr. Shofiur Rahman in the research laboratory of Dr. Paris Georghiou at Memorial University. Their complexation properties with some Group 1, Group 2 and transition metal cation guests were studied.

Chapter 1 provides an overview of calixarenes and supramolecular chemistry and the methods employed herein.

In Chapter 2, as part of the on-going studies on the development of a microcantilever-based real-time device employing modified calixarene-derived sensing layers in a collaborative project with the research group of Dr. Luc Beaulieu in the Department of Physics and Physical Oceanography at MUN, a study was undertaken to determine the solution-phase complexation properties of **5** and its ethyl analogue **6**, using  $^1\text{H-NMR}$  spectroscopic titrations.

The work described in Chapter 3 concerns the study of the supramolecular complexation behaviour of tetra-*n*-butylammonium halides (TBAX: X =  $\text{Cl}^-$ ,  $\text{Br}^-$ ) in different commonly-employed deuterated solvents such as  $\text{CD}_3\text{OD}$ ,  $(\text{CD}_3)_2\text{CO}$ ,  $\text{CD}_2\text{Cl}_2$ ,  $\text{CD}_3\text{CN}$  and  $\text{DMSO-}d_6$ , using  $^1\text{H-NMR}$  spectroscopy.

Chapter 4, describes of new macrocyclic receptors namely, triazolyl-bridged naphthalene-calix[4]arenes, which were succssfully synthesised by Dr. Shofiur Rahman in the research laboratory of Dr. Paris Georghiou at MUN. In the study reported herein, their complexation properties with various metal ions were investigated using both fluorescence spectroscopy and  $^1\text{H-NMR}$  spectroscopy.

## **Acknowledgments**

I would like to extend my sincere admiration and immeasurable thanks to my supervisor, Professor Paris E. Georghiou, for his guidance, encouragement and valuable advice during the course of my research project and the writing of this thesis.

I am also grateful to Dr. S. Rahman for his valuable advice, helpful discussions and guidance. My appreciation is also extended to my supervisory committee, Dr. R. Davis, and Dr. K. Hattenhauer, for proofreading, valuable comment and suggestions. I also would like to thank Dr. Brent Myron for training and support with fluorescence spectroscopy and Dr. Celine Schneider for training and support with NMR spectroscopy.

Thanks are also due to the members of the Georghiou group, both past and present, and the staff in the Chemistry Department for their support, help and friendship. It has been a great joy to me to work together with you all.

Special thanks are also extended to my father, my mother, my wife, my brothers, my sisters. The financial support from Saudi Arabia Cultural Bureau in Canada and The Ministry of Higher Education in Saudi Arabia is gratefully acknowledged.

## **Table of Contents**

<b>Title.....</b>	<b>i</b>
<b>Dedication .....</b>	<b>ii</b>
<b>Abstract.....</b>	<b>iii</b>
<b>Acknowledgments .....</b>	<b>v</b>
<b>Table of Contents .....</b>	<b>vi</b>
<b>List of Figures.....</b>	<b>xii</b>
<b>List of Tables .....</b>	<b>xx</b>
<b>List of Abbreviations .....</b>	<b>xxiii</b>
<b>Appendix.....</b>	<b>xxv</b>

<b>Chapter 1</b> .....	<b>1</b>
1.1 Calixarenes .....	1
1.2 Supramolecular chemistry .....	6
1.3. Noncovalent interactions .....	9
1.3.1. Ion pairing.....	10
1.3.2. Dipole-dipole interactions .....	11
1.3.3. Hydrogen bonding .....	11
1.3.4. Cation- $\pi$ interactions.....	13
1.3.5. Aromatic $\pi$ - $\pi$ interactions .....	14
1.4 Characterization of host-guest complexation.....	15
1.4.1 Nuclear magnetic resonance (NMR) spectroscopy .....	15
1.4.2 Photophysics of Fluorescent chemosensors.....	17
1.4.2.1 Principles of fluorescent chemosensors .....	17
1.4.2.2 Photoinduced electron transfer (PET) .....	19
1.4.2.3 Photoinduced charge-transfer (PCT).....	21
1.4.2.4 Excimer formation .....	22
1.5 Determination of the association constant ( $K_{assoc}$ ) .....	23
1.6 References .....	25

<b>Chapter 2 .....</b>	<b>29</b>
2.1 Introduction.....	29
2.1.1 Gold-supported calixarenes .....	30
2.1.2 Cation sensors .....	31
2.1.3 Anion sensors .....	33
2.1.4 Thiocetate-bearing calix[4]arene.....	33
2.1.4.1 Synthesis of upper- and lower-rim functionalized calix[4]arenes.....	35
2.1.4.2 Microcantilever results.....	36
2.2. Objectives of the work reported in this Chapter .....	37
2.3 Complexation studies.....	37
2.3.1 Complexation of methly ester calixarene <b>5</b> and its corresponding ethly ester <b>6</b> with various calcium salts.....	38
2.3.1.1 Ethly ester <b>6</b> with CaCl <sub>2</sub> .....	38
2.3.1.2 Methly ester <b>5</b> with CaCl <sub>2</sub> .....	41
2.3.1.3 Methly ester <b>5</b> with CaBr <sub>2</sub> .....	45
2.3.1.4 Ethly ester <b>6</b> with CaI <sub>2</sub> .....	47
2.3.1.5 Methyl ester <b>5</b> with CaI <sub>2</sub> .....	49
2.3.2 Complexation of methyl ester calixarene <b>5</b> and its corresponding ethyl ester <b>6</b> with group (1) salts .....	53

2.3.2.1 Ethyl ester <b>6</b> with NaI .....	53
2.3.2.2 Methyl ester <b>5</b> with NaI.....	55
2.3.2.3 Ethyl ester <b>6</b> with KI.....	59
2.3.2.4 Methyl ester <b>5</b> with KI .....	62
2.3.3 Complexation of methyl ester calixarene <b>5</b> and its corresponding ethyl ester <b>6</b> with AgTFA .....	65
2.3.3.1 Ethyl ester <b>6</b> with AgTFA.....	65
2.3.3.2 Methyl ester <b>5</b> with AgTFA .....	68
2.3.4 Comparison between the $K_{assoc}$ values of <b>5</b> and <b>6</b> .....	72
2.4. References .....	74
<b>Chapter 3 .....</b>	<b>76</b>
3.1 Introduction.....	76
3.1.1 NMR studies of the complexation of tetrabutylammonium halides .....	76
3.2 Experimental section.....	81
3.3 Complexation studies of different TBAX halides with different solutions .....	81
3.3.1 Titration of TBACl in acetone- $d_6$ (( $CD_3$ ) $_2$ CO) .....	82
3.3.2 Titration of TBACl in acetonitrile- $d_3$ ( $CD_3$ CN).....	84
3.3.3 Titration of TBACl in DMSO- $d_6$ .....	85
3.2.4 Titration of TBACl in methanol- $d_4$ ( $CD_3$ OD).....	87

3.3.5 Titration of TBACl in DCM- $d_2$ .....	89
3.3.6 Titration of TBABr in acetone- $d_6$ .....	91
3.4. Conclusion and Summary.....	93
3.5 References.....	95
<b>Chapter 4.....</b>	<b>96</b>
4.1 Introduction.....	96
4.1.1 The copper(I)-catalyzed alkyne-azide cycloaddition (CuAAC).....	97
4.1.2 Triazole-bridge based calixarene chemosensors.....	98
4.1.2.1 Metal ions receptor.....	98
4.1.2.2 Anion receptors.....	100
4.2 Objectives of the work reported in this Chapter.....	101
4.3 Complexation studies.....	102
4.3.1 Experimental section.....	102
4.3.2 Complexation studies using fluorescence spectroscopy.....	104
4.3.2.1 Calculation of association constants.....	104
4.3.2.2 Fluorescence complexation studies with hosts <b>6a-6d</b> .....	104
4.3.2.3 Job plot analysis of host <b>6a-6d</b> .....	107
4.3.2.4 Fluorescence quenching of receptors <b>6a-6d</b> with different metal ions...	108

4.3.2.5 Comparison of the association constants of receptors <b>6a-6d</b> with metal ions.....	109
4.3.3 <sup>1</sup> H-NMR complexation studies.....	110
4.3.3.1 Complexation of receptor <b>6d</b> with Fe <sup>3+</sup> .....	110
4.3.4 Computational studies .....	112
4.3.4.1 General description for the computational study.....	112
4.3.4.2 Calculated binding energies .....	112
4.4 Conclusions .....	117
4.5 References .....	118

## List of Figures

Figure 1-1. <i>p</i> -Tert-butyl-calix[4]arene and <i>kalyx krater</i> vase showing resemblance in shape between the two .....	1
Figure 1-2. The two different modes for the phenyl units' inversion.....	2
Figure 1-3. The anatomy of a calix[4]arene in the cone conformation.....	3
Figure 1-4. The four stable conformations of calix[4]arenes .....	4
Figure 1-5. Examples of calixarene-guest complexes .....	5
Figure 1-6. Some calixarene analogues .....	6
Figure 1-7. Comparison between the scope of molecular and supramolecular chemistry. .	8
Figure 1-8. Dipole-dipole interactions between two carbonyl group .....	11
Figure 1-9. Hydrogen bonds between donor D and acceptor A atoms .....	12
Figure 1-10. Schematic representation of cation- $\pi$ interactions showing the contact of $K^+$ ion and benzene. The quadrupolar moment of benzene is represented as the two opposing dipoles .....	14
Figure 1-11. (a) The limiting types of aromatic $\pi$ - $\pi$ interactions: face-to-face (interplanar distance about 3.3–3.8Å) and edge-to-face orientations. (b) The repulsion between negatively charged $\pi$ -electron clouds of facially oriented aromatic rings .....	15
Figure 1-12. Perrin–Jablonski diagram and illustration of the relative positions of absorption, fluorescence and phosphorescence spectra .....	18
Figure 1-13. Diagram of an effective fluorescent chemosensor .....	19
Figure 1-14. Mechanisms for PET (a) and CHEF (b) systems .....	20
Figure 1-15. A PCT system .....	21

Figure 2-1. Two different forms of representations of the structure of a calix[4]arene showing the “upper” and “lower” rims, which can have different functional groups represented as “X” and “R” respectively.....	29
Figure 2-2. gold-supported SAM calixarene with a aniline guest. ....	30
Figure 2-3. (A) A sensor chip configuration. (B) SPR angle shifts with respect to various concentrations of several metal ions. Solid line is the linear fit ( $r^2 = 0.9928$ ). Other lines were used to guide eyes.. ....	31
Figure 2-4. (A) Molecular structure of calix [4] benzocrown co-absorbed with decane-1-thiol on the gold surface of a microcantilever via the SAM technique. (B) Bending deflection response of the SAM-coated microcantilever as a function of the change in the concentration of $\text{Cs}^+$ and $\text{K}^+$ ions .....	32
Figure 2-5. Molecular structure of calix[6]-crown. ....	33
Figure 2-6. Structure of <b>5</b> showing the “anchoring” of the “upper rim” thioacetate grouping onto the gold surface of a gold microcantilever. ....	34
Figure 2-7. Responses to different concentrations of $\text{CaCl}_2$ for microcantilevers functionalized with calix[4]arene <b>5</b> and a reference microcantilever functionalized with 1-decanethiol .....	36
Figure 2-8. Structures of Calix <b>5</b> and <b>6</b> .....	38
Figure 2-9. $^1\text{H}$ NMR (300 MHz) titration spectra for Ar- <i>H</i> ( <i>Top</i> ), $\text{COOCH}_2\text{CH}_3$ ( <i>Middle</i> ), and $\text{SCOCH}_3$ ( <i>Bottom</i> ) of <b>6</b> with $\text{CaCl}_2$ .....	39
Figure 2-10. $^1\text{H}$ NMR (300 MHz) titration curves for Ar- <i>H</i> , $\text{COOCH}_2\text{CH}_3$ , and $\text{SCOCH}_3$ respectively, of <b>6</b> ( $1.50 \times 10^{-3}$ M) with $\text{CaCl}_2$ .....	41

Figure 2-11. <sup>1</sup> H NMR (300 MHz) titration spectra for -OCH <sub>2</sub> COOCH <sub>3</sub> , ( <i>Top</i> ) and COOCH <sub>3</sub> ( <i>Bottom</i> ) of <b>5</b> with CaCl <sub>2</sub> .....	42
Figure 2-12. <sup>1</sup> H NMR (300 MHz) titration spectra for Ar-H ( <i>Top</i> ) and SCOCH <sub>3</sub> ( <i>Bottom</i> ) of <b>5</b> with CaCl <sub>2</sub> .....	43
Figure 2-13. <sup>1</sup> H NMR (300 MHz) titration curves for Ar-H, -OCH <sub>2</sub> COOCH <sub>3</sub> , COOCH <sub>3</sub> , and SCOCH <sub>3</sub> respectively of <b>5</b> (1.5 x 10 <sup>-3</sup> M) with CaCl <sub>2</sub> .....	45
Figure 2-14. <sup>1</sup> H NMR (300 MHz) titration spectra for Ar-H ( <i>Top</i> ), COOCH <sub>3</sub> ( <i>Middle</i> ), and SCOCH <sub>3</sub> ( <i>Bottom</i> ) of <b>5</b> with CaBr <sub>2</sub> .....	46
Figure 2-15. <sup>1</sup> H NMR (300 MHz) titration spectra for Ar-H ( <i>Top</i> ), COOCH <sub>2</sub> CH <sub>3</sub> ( <i>Middle</i> ), and SCOCH <sub>3</sub> ( <i>Bottom</i> ) of <b>6</b> with CaI <sub>2</sub> .....	48
Figure 2-16. <sup>1</sup> H NMR (300 MHz) titration curves for Ar-H, COOCH <sub>2</sub> CH <sub>3</sub> , and SCOCH <sub>3</sub> respectively of <b>6</b> (1.50×10 <sup>-3</sup> M) with CaI <sub>2</sub> .....	49
Figure 2-17. <sup>1</sup> H NMR (300 MHz) titration spectra for Ar-H ( <i>Top</i> ) and COOCH <sub>3</sub> ( <i>Bottom</i> ) of <b>5</b> with CaI <sub>2</sub> .....	50
Figure 2-18. <sup>1</sup> H NMR (300 MHz) titration spectra for -OCH <sub>2</sub> COOCH <sub>3</sub> , ( <i>Top</i> ) and SCOCH <sub>3</sub> ( <i>Bottom</i> ) of <b>5</b> with CaI <sub>2</sub> .....	51
Figure 2-19. <sup>1</sup> H NMR (300 MHz) titration curves for Ar-H, -COOCH <sub>3</sub> , SCOCH <sub>3</sub> , and OCH <sub>2</sub> COOCH <sub>3</sub> , respectively of <b>5</b> (1.50×10 <sup>-3</sup> M) with CaI <sub>2</sub> .....	52
Figure 2-20. <sup>1</sup> H NMR (300 MHz) titration spectra for Ar-H ( <i>Top</i> ), COOCH <sub>2</sub> CH <sub>3</sub> ( <i>Middle</i> ), and SCOCH <sub>3</sub> ( <i>Bottom</i> ) of <b>6</b> with NaI.....	53
Figure 2-21. <sup>1</sup> H NMR (300 MHz) titration curves for Ar-H, SCOCH <sub>3</sub> , and COOCH <sub>2</sub> CH <sub>3</sub> respectively of <b>6</b> (1.50×10 <sup>-3</sup> M) with NaI .....	55

Figure 2-22. <sup>1</sup> H NMR (300 MHz) titration spectra for Ar- <i>H</i> (Top), -OCH <sub>2</sub> COOCH <sub>3</sub> , (Bottom) of <b>5</b> with NaI.....	56
Figure 2-23. <sup>1</sup> H NMR (300 MHz) titration spectra for COOCH <sub>3</sub> (Top), SCOCH <sub>3</sub> (Bottom) of <b>5</b> with NaI.....	57
Figure 2-24. <sup>1</sup> H NMR (300 MHz) titration curves for Ar- <i>H</i> , -OCH <sub>2</sub> COOCH <sub>3</sub> , COOCH <sub>3</sub> , and SCOCH <sub>3</sub> , respectively of <b>5</b> (1.50×10 <sup>-3</sup> M) with NaI.....	58
Figure 2-25. <sup>1</sup> H NMR (300 MHz) titration spectra for Ar- <i>H</i> (Top), COOCH <sub>2</sub> CH <sub>3</sub> (Bottom) of <b>6</b> with KI. ....	59
Figure 2-26. <sup>1</sup> H NMR (300 MHz) titration spectra for SCOCH <sub>3</sub> of <b>6</b> with KI.....	60
Figure 2-27. <sup>1</sup> H NMR (300 MHz) titration curves for Ar- <i>H</i> , SCOCH <sub>3</sub> , and COOCH <sub>2</sub> CH <sub>3</sub> respectively of <b>6</b> (1.50×10 <sup>-3</sup> M) with KI.....	61
Figure 2-28. <sup>1</sup> H NMR (300 MHz) titration spectra for Ar- <i>H</i> (Top) and COOCH <sub>3</sub> (Bottom) of <b>5</b> with KI.....	62
Figure 2-29. <sup>1</sup> H NMR (300 MHz) titration spectra for SCOCH <sub>3</sub> (Top) and OCH <sub>2</sub> COOCH <sub>3</sub> , (Bottom) of <b>5</b> with KI.....	63
Figure 2-30. <sup>1</sup> H NMR (300 MHz) titration curves for Ar- <i>H</i> , -OCH <sub>2</sub> COOCH <sub>3</sub> , COOCH <sub>3</sub> , and SCOCH <sub>3</sub> , respectively of <b>5</b> (1.50×10 <sup>-3</sup> M) with KI.....	65
Figure 2-31. <sup>1</sup> H NMR (300 MHz) titration spectra for Ar- <i>H</i> (Top), COOCH <sub>2</sub> CH <sub>3</sub> (Middle), and SCOCH <sub>3</sub> (Bottom) of <b>6</b> with AgTFA. ....	66
Figure 2-32. <sup>1</sup> H NMR (300 MHz) titration curves for Ar- <i>H</i> , -SCOCH <sub>3</sub> , and COOCH <sub>2</sub> CH <sub>3</sub> respectively of <b>6</b> (1.50×10 <sup>-3</sup> M) with AgTFA.....	67

Figure 2-33. <sup>1</sup> H NMR (300 MHz) titration spectra for Ar- <i>H</i> ( <i>Top</i> ) and COOCH <sub>3</sub> ( <i>Bottom</i> ) of <b>5</b> with AgTFA.....	69
Figure 2-34. <sup>1</sup> H NMR (300 MHz) titration spectra for -OCH <sub>2</sub> COOCH <sub>3</sub> ( <i>Top</i> ) and SCOCH <sub>3</sub> ( <i>Bottom</i> ) of <b>5</b> (1.50×10 <sup>-3</sup> M) with AgTFA .....	70
Figure 2-35. <sup>1</sup> H NMR (300 MHz) titration curves for Ar- <i>H</i> , -OCH <sub>2</sub> COOCH <sub>3</sub> , COOCH <sub>3</sub> , and SCOCH <sub>3</sub> respectively of <b>5</b> (1.50×10 <sup>-3</sup> M) with AgTFA .....	72
Figure 3-1. Proton shielding of 0.1 M CHCl <sub>3</sub> in CH <sub>3</sub> CN as a function of TBABr concentration.....	78
Figure 3-2. Asymmetric unit of TBABr:CHCl <sub>3</sub> .....	79
Figure 3-3. Least-squares linear plots of the CDCl <sub>3</sub> :TBAX titrations.....	80
Figure 3-4. <sup>1</sup> H NMR (500 MHz) expanded titration spectra for the residual proton signal of the (CD <sub>3</sub> ) <sub>2</sub> CO solvent with increasing amounts of TBACl. ....	82
Figure 3-5. Least-squares linear regression plot for the (CD <sub>3</sub> ) <sub>2</sub> CO: TBACl data. ....	83
Figure 3-6. <sup>1</sup> H NMR (500 MHz) expanded titration spectra for the residual proton signal of the (CD <sub>3</sub> ) <sub>2</sub> CO solvent with increasing amounts of TBACl. ....	84
Figure 3-7. Least-squares linear regression plot for the CD <sub>3</sub> CN: TBACl data.....	85
Figure 3-8. <sup>1</sup> H NMR (500 MHz) expanded titration spectra for the residual proton signal of the DMSO solvent with increasing amounts of TBACl. ....	86
Figure 3-9. Least-squares linear regression plot for the DMSO-d <sub>6</sub> : TBACl data.....	87
Figure 3-10. <sup>1</sup> H NMR (500 MHz) expanded titration spectra for the residual proton signal of the CD <sub>3</sub> OD solvent with increasing amounts of TBACl.....	88
Figure 3-11. Least-squares linear regression plot for the CD <sub>3</sub> OD: TBACl data .....	89

Figure 3-12. <sup>1</sup> H NMR (500 MHz) expanded titration spectra for the residual proton signal of the DCM- <i>d</i> <sub>2</sub> solvent with increasing amounts of TBACl.....	90
Figure 3-13. Least-squares linear regression plot for the DCM- <i>d</i> <sub>2</sub> : TBACl data. ....	91
Figure 3-14. Least-squares linear regression plot for the (CD <sub>3</sub> ) <sub>2</sub> CO: TBABr data. ....	92
Figure 3-15. <sup>1</sup> H NMR (500 MHz) expanded titration spectra for the residual proton signal of the (CD <sub>3</sub> ) <sub>2</sub> CO solvent with increasing amounts of TBABr.....	93
Figure 3-16. Slope values of TBACl with different ((CD <sub>3</sub> ) <sub>2</sub> CO, CD <sub>3</sub> CN, CD <sub>3</sub> OD, CD <sub>2</sub> Cl <sub>2</sub> and DMSO- <i>d</i> <sub>6</sub> ) solvents. ....	94
Figure 4-1. Triazole-bridge based calix[4]arenes <b>1a-c</b> .....	98
Figure 4-2. Triazole-modified calix[4]crown as a novel fluorescent on-off switchable chemosensor.....	99
Figure 4-3. Salicylaldimine-appended triazole-linked calix[4]arene.....	100
Figure 4-4. An aryl-triazole receptor capable of strong chloride binding. ....	101
Figure 4-5. <i>Left</i> : Fluorescence spectra of <b>6a</b> (1.64 μM) upon addition of Fe <sup>3+</sup> in acetonitrile/chloroform (v/v= 9:1) solutions. λ <sub>ex</sub> =291 nm. <i>Right</i> : Benesi-Hildebrand plots of 1/( <i>F</i> - <i>F</i> <sub>0</sub> ) versus 1/[Fe(ClO <sub>4</sub> ) <sub>3</sub> ] for <b>6a</b> upon titration with Fe <sup>3+</sup> (0-14 equivalents) .....	105
Figure 4-6. <i>Left</i> : Fluorescence spectra of <b>6b</b> (1.64 μM) upon addition of Fe <sup>3+</sup> in acetonitrile/chloroform (v/v= 9:1) solutions. λ <sub>ex</sub> =291 nm. <i>Right</i> : Benesi-Hildebrand plots of 1/( <i>F</i> - <i>F</i> <sub>0</sub> ) versus 1/[Fe(ClO <sub>4</sub> ) <sub>3</sub> ] for <b>6b</b> upon titration with Fe <sup>3+</sup> (0-14.6 equivalents). ..	106
Figure 4-7. <i>Left</i> : Fluorescence spectra of <b>6c</b> (1.64 μM) upon addition of Fe <sup>3+</sup> in acetonitrile/chloroform (v/v= 9:1) solutions. λ <sub>ex</sub> =291 nm. <i>Right</i> : Benesi-Hildebrand plots of 1/( <i>F</i> - <i>F</i> <sub>0</sub> ) versus 1/[Fe(ClO <sub>4</sub> ) <sub>3</sub> ] for <b>6c</b> upon titration with Fe <sup>3+</sup> (0-14.6 equivalents)....	106

Figure 4-8. <i>Left</i> : Fluorescence spectra of <b>6d</b> (1.64 $\mu$ M) upon addition of $\text{Fe}^{3+}$ in acetonitrile/chloroform (v/v= 9:1) solutions. $\lambda_{\text{ex}} = 291$ nm. <i>Right</i> : Benesi-Hildebrand plots of $1/(F-F_0)$ versus $1/[\text{Fe}(\text{ClO}_4)_3]$ for <b>6d</b> upon titration with $\text{Fe}^{3+}$ (0-14.6 equivalents) ...	107
Figure 4-9. Job plot curves showing 1:1 complexation for <i>Left</i> : <b>6a</b> with $\text{Fe}^{3+}$ . <i>Middle</i> : <b>6c</b> with $\text{Hg}^{2+}$ . <i>Right</i> : <b>6d</b> with $\text{Cu}^{2+}$ .....	107
Figure 4-10. Histogram showing the fluorescence quenching of receptors <b>6a</b> (blue) and <b>6b</b> (red) with different metal ions. ....	108
Figure 4-11. Histogram showing the fluorescence quenching of receptors <b>6c</b> (blue) and <b>6d</b> (red) with different metal ions .....	108
Figure 4-12. Histogram showing the association constants ( $K_{\text{assoc}}$ ) values determined for receptors <b>6a</b> (red) and <b>6b</b> (blue) with different metal ions. ....	109
Figure 4-13. Histogram showing the association constants ( $K_{\text{assoc}}$ ) values determined for receptors <b>6c</b> (red) and <b>6d</b> (blue) with different metal ions .....	110
Figure 4-14. Partial $^1\text{H}$ NMR (300 MHz) spectra of <b>6d</b> ( $1.98 \times 10^{-2}$ M) upon addition of $\text{Fe}(\text{ClO}_4)_3$ (0-2.0 equivalents) in a $\text{CD}_2\text{Cl}_2:\text{CD}_3\text{CN}$ (3:1, v/v) at 298K .....	111
Figure 4-15. Geometry-optimized (ball-and-stick) structures of: <i>Left</i> : <b>6a</b> and <i>Right</i> : $6a \supset \text{Fe}^{3+}$ complex .....	114
Figure 4-16. Geometry-optimized (space fill) structures of: <i>Left</i> : <b>6a</b> and <i>Right</i> : $6a \supset \text{Fe}^{3+}$ complex.....	115
Figure 4-17. Geometry-optimized (ball-and-stick) structures of: <i>Left</i> : <b>6a</b> and <i>Right</i> : $6a \supset \text{Hg}^{2+}$ complex .....	115

Figure 4-18. Geometry-optimized (space fill) structures of: *Left: 6a* and *Right: 6a*⊃ $\text{Hg}^{2+}$  complex.....116

Figure 4-19. Geometry-optimized (ball-and-stick) structures of: *Left: 6a* and *Right: 6a*⊃ $\text{Cu}^{2+}$  complex.....116

## List of Tables

Table 1-1. Classification and some properties of hydrogen bonds [1] .....	13
Table 2-1. $^1\text{H}$ NMR (300 MHz) titration chemical shift data for Ar- <i>H</i> , $\text{COOCH}_2\text{CH}_3$ , and $\text{SCOCH}_3$ of <b>6</b> ( $1.50 \times 10^{-3}$ M) upon the addition of $\text{CaCl}_2$ .....	40
Table 2-2. $^1\text{H}$ NMR (300 MHz) titration chemical shift data for $-\text{OCH}_2\text{COOCH}_3$ , and $\text{COOCH}_3$ of <b>5</b> ( $1.50 \times 10^{-3}$ M) with $\text{CaCl}_2$ .....	42
Table 2-3. $^1\text{H}$ NMR (300 MHz) titration chemical shift data for Ar- <i>H</i> , and $\text{SCOCH}_3$ of <b>5</b> with $\text{CaCl}_2$ .....	44
Table 2-4. $^1\text{H}$ NMR (300 MHz) titration chemical shift data for Ar- <i>H</i> , $\text{COOCH}_3$ , and $\text{SCOCH}_3$ of <b>5</b> ( $1.50 \times 10^{-3}$ M) with $\text{CaBr}_2$ .....	45
Table 2-5. $^1\text{H}$ NMR (300 MHz) titration chemical shift data for Ar- <i>H</i> , $\text{COOCH}_2\text{CH}_3$ , and $\text{SCOCH}_3$ of <b>6</b> ( $1.50 \times 10^{-3}$ M) with $\text{CaI}_2$ .....	47
Table 2-6. $^1\text{H}$ NMR (300 MHz) titration chemical shift data for Ar- <i>H</i> , $\text{COOCH}_3$ of <b>5</b> ( $1.50 \times 10^{-3}$ M) with $\text{CaI}_2$ .....	50
Table 2-7. $^1\text{H}$ NMR (300 MHz) titration chemical shift data for Ar- <i>H</i> and $\text{COOCH}_3$ of <b>5</b> ( $1.50 \times 10^{-3}$ M) with $\text{CaI}_2$ .....	52
Table 2-8. $^1\text{H}$ NMR (300 MHz) titration chemical shift data for Ar- <i>H</i> , $\text{COOCH}_2\text{CH}_3$ , and $\text{SCOCH}_3$ of <b>6</b> ( $1.50 \times 10^{-3}$ M) with $\text{NaI}$ .....	54
Table 2-9. $^1\text{H}$ NMR (300 MHz) titration chemical shift data for Ar- <i>H</i> and $\text{OCH}_2\text{COOCH}_3$ , of <b>5</b> ( $1.50 \times 10^{-3}$ M) with $\text{NaI}$ .....	55
Table 2-10. $^1\text{H}$ NMR (300 MHz) titration chemical shift data for $\text{SCOCH}_3$ and $\text{COOCH}_3$ , of <b>5</b> ( $1.50 \times 10^{-3}$ M) with $\text{NaI}$ .....	58

Table 2-11. $^1\text{H}$ NMR (300 MHz) titration chemical shift data for Ar- <i>H</i> , $\text{COOCH}_2\text{CH}_3$ , and $\text{SCOCH}_3$ of <b>6</b> ( $1.5 \times 10^{-3}$ M) with KI. ....	60
Table 2-12. $^1\text{H}$ NMR (300 MHz) titration chemical shift data for Ar- <i>H</i> , and $\text{COOCH}_3$ of <b>5</b> ( $1.50 \times 10^{-3}$ M) with KI. ....	63
Table 2-13. $^1\text{H}$ NMR (300 MHz) titration chemical shift data for $\text{SCOCH}_3$ , and $-\text{OCH}_2\text{O}-$ of <b>5</b> ( $1.50 \times 10^{-3}$ M) with KI. ....	64
Table 2-14. $^1\text{H}$ NMR (300 MHz) titration chemical shift data for Ar- <i>H</i> , $\text{COOCH}_3$ , and $\text{SCOCH}_3$ of <b>6</b> ( $1.50 \times 10^{-3}$ M) with AgTFA. ....	67
Table 2-15. $^1\text{H}$ NMR (300 MHz) titration chemical shift data for Ar- <i>H</i> , $\text{COCH}_2\text{CH}_3$ , and $\text{SCOCH}_3$ of <b>6</b> ( $1.50 \times 10^{-3}$ M) with AgTFA. ....	68
Table 2-16. $^1\text{H}$ NMR (300 MHz) titration chemical shift data for $\text{SCOCH}_3$ , and $\text{OCH}_2\text{COOCH}_3$ of <b>5</b> ( $1.50 \times 10^{-3}$ M) with AgTFA. ....	71
Table 2-17. $K_{\text{assoc}}$ values for <b>5</b> and <b>6</b> with representative salts. ....	73
Table 3-1. $^1\text{H}$ -NMR (500 MHz) titration data in $(\text{CD}_3)_2\text{CO}$ . ....	83
Table 3-2. $^1\text{H}$ NMR (500 MHz) titration data in $\text{CD}_3\text{CN}$ . ....	85
Table 3-3. $^1\text{H}$ NMR (500 MHz) titration data in $\text{DMSO}-d_6$ . ....	86
Table 3-4. $^1\text{H}$ NMR (500 MHz) titration data in $\text{CD}_3\text{OD}$ . ....	88
Table 3-5. $^1\text{H}$ NMR (500 MHz) titration data in $\text{DCM}-d_2$ . ....	90
Table 3-6. $^1\text{H}$ NMR (500 MHz) titration data for $(\text{CD}_3)_2\text{CO}$ . ....	93
Table 4-1. Calculated binding energies (KJ/mole) for the receptors <b>6a</b> and <b>6c</b> with $\text{Fe}^{3+}$ , $\text{Hg}^{2+}$ and $\text{Cu}^{2+}$ cations. ....	113

Table 4-2. The calculated distance for selected parameters for the Backbones of the receptor **6a** and complex with metal cations ( $M^{n+} = Fe^{3+}$ ,  $Hg^{2+}$  and  $Cu^{2+}$ ) optimized at B3LYP/lanl2dz Level (Distance in Å).....113

Table 4-3. The calculated distance for selected parameters for the Backbones of the receptor **6c** and complex with metal cations ( $M^{n+} = Fe^{3+}$ ,  $Hg^{2+}$  and  $Cu^{2+}$ ) optimized at B3LYP/lanl2dz Level (Distance in Å).....114

## List of Abbreviations

Å	Angstrom unit
AuNPs	Gold nanoparticles
CT	Charge-transfer
$\delta$	Chemical shift in ppm down-field from tetramethylsilane
FS	Fluorescence spectroscopy
Hz	Hertz
$J$	Coupling constant
$K_{assoc}$	Association constant
MS	Mass spectroscopy
MMFF	Merck molecular force field
Me	Methyl
NMR	Nuclear magnetic resonance
$p$	Para-
Ar	Aromatic
Ph	Phenyl
ppm	parts per million
ppb	parts per billion
PET	Photoinduced electron transfer
PTI	Photon Technology International
PMT	photomultiplier tube
PCT	Photoinduced charge transfer

SAM	Self-assembled monolayer
SPR	Surface plasmon resonance
STM	Scanning Tunneling Microscopy
SEM	Scanning Electron Microscopy
TFA	Trifluoroacetate
TMS	Tetramethylsilane (in NMR)
TBAX	Tetra- <i>n</i> -butylammonium salts
UV-Vis	UV-visible spectroscopy
CaBr <sub>2</sub>	Calcium bromide
DMSO- <i>d</i> <sub>6</sub>	Dimethyl Sulfoxide- <i>d</i> <sub>6</sub>
CD <sub>3</sub> CN	Acetonitrile- <i>d</i> <sub>3</sub>
(CD <sub>3</sub> ) <sub>2</sub> CO	Acetone- <i>d</i> <sub>6</sub>
CD <sub>3</sub> OD	Methanol- <i>d</i> <sub>4</sub>
DCM- <i>d</i> <sub>2</sub>	Dichloromethane

## Appendix

- Figure 4-20. *Left:* Fluorescence spectra of **6a** (1.50  $\mu\text{M}$ ) upon addition of  $\text{Cu}^{2+}$  in acetonitrile/ chloroform (v/v= 9:1) solutions.  $\lambda_{\text{ex}} = 284 \text{ nm}$ . *Right:* Benesi-Hildebrand plot of  $1/(\text{F}_0 - \text{F})$  versus  $1/[\text{Cu}(\text{ClO}_4)_2]$  for **6a** upon titration with  $\text{Cu}(\text{ClO}_4)_2$  (0-15 equivalents). The linear fit showed a 1:1 complexation between **6a** and  $\text{Cu}^{2+}$  ions..... 121
- Figure 4-21. *Left:* Fluorescence spectra of **6a** (1.50  $\mu\text{M}$ ) upon addition of  $\text{Fe}^{2+}$  in acetonitrile/ chloroform (v/v= 9:1) solutions.  $\lambda_{\text{ex}} = 284 \text{ nm}$ . *Right:* Benesi-Hildebrand plot of  $1/(\text{F}_0 - \text{F})$  versus  $1/[\text{Fe}(\text{ClO}_4)_2]$  for **6a** upon titration with  $\text{Fe}(\text{ClO}_4)_2$  (0-20 equivalents). The linear fit showed a 1:1 complexation between **6a** and  $\text{Fe}^{2+}$  ions ..... 121
- Figure 4-22. *Left:* Fluorescence spectra of **6a** (1.50  $\mu\text{M}$ ) upon addition of  $\text{Hg}^{2+}$  in acetonitrile/ chloroform (v/v= 9:1) solutions.  $\lambda_{\text{ex}} = 284 \text{ nm}$ . *Right:* Benesi-Hildebrand plot of  $1/(\text{F}_0 - \text{F})$  versus  $1/[\text{Hg}(\text{ClO}_4)_2]$  for **6a** upon titration with  $\text{Hg}(\text{ClO}_4)_2$  (0-14.5 equivalents). The linear fit showed a 1:1 complexation between **6a** and  $\text{Hg}^{2+}$  ions..... 122
- Figure 4-23. *Left:* Fluorescence spectra of **6a** (1.50  $\mu\text{M}$ ) upon addition of  $\text{Mn}^{2+}$  in acetonitrile/ chloroform (v/v= 9:1) solutions.  $\lambda_{\text{ex}} = 284 \text{ nm}$ . *Right:* Benesi-Hildebrand plot of  $1/(\text{F}_0 - \text{F})$  versus  $1/[\text{Mn}(\text{ClO}_4)_2]$  for **6a** upon titration with  $\text{Mn}(\text{ClO}_4)_2$  (0-14.8 equivalents). The linear fit showed a 1:1 complexation between **6a** and  $\text{Mn}^{2+}$  ions ..... 122
- Figure 4-24. *Left:* Fluorescence spectra of **6a** (1.50  $\mu\text{M}$ ) upon addition of  $\text{Pb}^{2+}$  in acetonitrile/ chloroform (v/v= 9:1) solutions.  $\lambda_{\text{ex}} = 284 \text{ nm}$ . *Right:* Benesi-Hildebrand plot of  $1/(\text{F}_0 - \text{F})$  versus  $1/[\text{Pb}(\text{ClO}_4)_2]$  for **6a** upon titration with  $\text{Pb}(\text{ClO}_4)_2$  (0-16.4 equivalents). The linear fit showed a 1:1 complexation between **6a** and  $\text{Pb}^{2+}$  ions..... 123

Figure 4-25. *Left*: Fluorescence spectra of **6a** (1.50  $\mu\text{M}$ ) upon addition of  $\text{Ag}^+$  in acetonitrile/ chloroform (v/v= 9:1) solutions.  $\lambda_{\text{ex}} = 284 \text{ nm}$ . *Right*: Benesi-Hildebrand plot of  $1/(F_0-F)$  versus  $1/[\text{AgClO}_4]$  for **6a** upon titration with  $\text{Ag}(\text{ClO}_4)$  (0-14.2 equivalents). The linear fit showed a 1:1 complexation between **6a** and  $\text{Ag}^+$  ions.....123

Figure 4-26. *Left*: Fluorescence response of chemosensor **6b** (1.50  $\mu\text{M}$ ) to various equivalents of  $\text{Zn}(\text{ClO}_4)_2$  in acetonitrile/chloroform (v/v= 9:1) solutions. The excitation wavelength was  $\lambda = 291 \text{ nm}$ . *Right*: Benesi-Hildebrand plot of  $1/(F_0-F)$  versus  $1/[\text{Zn}(\text{ClO}_4)_2]$  for **6b** upon titration with  $\text{Zn}(\text{ClO}_4)_2$  (0-14.7 equivalents). The linear fit showed a 1:1 complexation between **6b** and  $\text{Zn}^{2+}$  ions .....124

Figure 4-27. *Left*: Fluorescence spectra of **6b** (1.50  $\mu\text{M}$ ) upon addition of  $\text{Cd}^{2+}$  in acetonitrile/ chloroform (v/v= 9:1) solutions.  $\lambda_{\text{ex}} = 291 \text{ nm}$ . *Right*: Benesi-Hildebrand plot of  $1/(F_0-F)$  versus  $1/[\text{M}(\text{ClO}_4)]$  for **6b** upon titration with  $\text{Cd}(\text{ClO}_4)_2$  (0-12 equivalents). The linear fit showed a 1:1 complexation between **6b** and  $\text{Cd}^{2+}$  ions .....124

Figure 4-28. *Left*: Fluorescence response of chemosensor **6c** (1.50  $\mu\text{M}$ ) to various equivalents of  $\text{Hg}(\text{ClO}_4)_2$  in acetonitrile/chloroform (v/v= 9:1) solutions. The excitation wavelength was  $\lambda = 291 \text{ nm}$ . *Right*: Benesi-Hildebrand plot of  $1/(F_0-F)$  versus  $1/[\text{Hg}(\text{ClO}_4)_2]$  for **6c** upon titration with  $\text{Hg}(\text{ClO}_4)_2$  (0-12 equivalents). The linear fit showed a 1:1 complexation between **6c** and  $\text{Hg}^{2+}$  ions .....125

Figure 4-29. *Left*: Fluorescence response of chemosensor **6c** (1.50  $\mu\text{M}$ ) to various equivalents of  $\text{Cu}(\text{ClO}_4)_2$  in acetonitrile/chloroform (v/v= 9:1) solutions. The excitation wavelength was  $\lambda = 291 \text{ nm}$ . *Right*: Benesi-Hildebrand plot of  $1/(F_0-F)$  versus

1/[Cu(ClO<sub>4</sub>)<sub>2</sub>] for **6c** upon titration with Cu(ClO<sub>4</sub>)<sub>2</sub> (0-14 equivalents). The linear fit showed a 1:1 complexation between **6c** and Cu<sup>2+</sup> ions.....125

Figure 4-30. *Left*: Fluorescence response of chemosensor **6c** (1.50 μM) to various equivalents of Pb(ClO<sub>4</sub>)<sub>2</sub> in acetonitrile/chloroform (v/v= 9:1) solutions. The excitation wavelength was λ 291 nm. *Right*: Benesi-Hildebrand plot of 1/(F<sub>o</sub>-F) versus 1/[Pb(ClO<sub>4</sub>)<sub>2</sub>] for **6c** upon titration with Pb(ClO<sub>4</sub>)<sub>2</sub> (0-14 equivalents). The linear fit showed a 1:1 complexation between **6c** and Pb<sup>2+</sup> ions. ....126

Figure 4-31. *Left*: Fluorescence response of chemosensor **6c** (1.50 μM) to various equivalents of Fe(ClO<sub>4</sub>)<sub>2</sub> in acetonitrile/chloroform (v/v= 9:1) solutions. The excitation wavelength was λ 291 nm. *Right*: Benesi-Hildebrand plot of 1/(F<sub>o</sub>-F) versus 1/[Fe(ClO<sub>4</sub>)<sub>2</sub>] for **6c** upon titration with Fe(ClO<sub>4</sub>)<sub>2</sub> (0-14 equivalents). The linear fit showed a 1:1 complexation between **6c** and Fe<sup>2+</sup> ions .....126

Figure 4-32. *Left*: Fluorescence response of chemosensor **6c** (1.50 μM) to various equivalents of Cd(ClO<sub>4</sub>)<sub>2</sub> in acetonitrile/chloroform (v/v= 9:1) solutions. The excitation wavelength was λ 291 nm. *Right*: Benesi-Hildebrand plot of 1/(F<sub>o</sub>-F) versus 1/[Cd(ClO<sub>4</sub>)<sub>2</sub>] for **6c** upon titration with Cd(ClO<sub>4</sub>)<sub>2</sub> (0-14 equivalents). The linear fit showed a 1:1 complexation between **6c** and Cd<sup>2+</sup> ions.....127

Figure 4-33. *Left*: Fluorescence response of chemosensor **6c** (1.50 μM) to various equivalents of Ca(ClO<sub>4</sub>)<sub>2</sub> in acetonitrile/chloroform (v/v= 9:1) solutions. The excitation wavelength was λ 291 nm. *Right*: Benesi-Hildebrand plot of 1/(F<sub>o</sub>-F) versus 1/[Ca(ClO<sub>4</sub>)<sub>2</sub>] for **6c** upon titration with Ca(ClO<sub>4</sub>)<sub>2</sub> (0-14 equivalents). The linear fit showed a 1:1 complexation between **6c** and Ca<sup>2+</sup> ions.....127

Figure 4-34. *Left:* Fluorescence response of chemosensor **6c** (1.50  $\mu\text{M}$ ) to various equivalents of  $\text{Zn}(\text{ClO}_4)_2$  in acetonitrile/chloroform (v/v= 9:1) solutions. The excitation wavelength was  $\lambda$  291 nm. *Right:* Benesi-Hildebrand plot of  $1/(F_o-F)$  versus  $1/[\text{Zn}(\text{ClO}_4)_2]$  for **6c** upon titration with  $\text{Zn}(\text{ClO}_4)_2$  (0-14 equivalents). The linear fit showed a 1:1 complexation between **6c** and  $\text{Zn}^{2+}$  ions.....128

Figure 4-35. *Left:* Fluorescence response of chemosensor **6c** (1.50  $\mu\text{M}$ ) to various equivalents of  $\text{CsClO}_4$  in acetonitrile/chloroform (v/v= 9:1) solutions. The excitation wavelength was  $\lambda$  291 nm. *Right:* Benesi-Hildebrand plot of  $1/(F_o-F)$  versus  $1/[\text{CsClO}_4]$  for **6c** upon titration with  $\text{CsClO}_4$  (0-14 equivalents). The linear fit showed a 1:1 complexation between **6c** and  $\text{Cs}^+$  ions.....128

Figure 4-36. *Left:* Fluorescence response of chemosensor **6c** (1.50  $\mu\text{M}$ ) to various equivalents of  $\text{Sr}(\text{ClO}_4)_2$  in acetonitrile/chloroform (v/v= 9:1) solutions. The excitation wavelength was  $\lambda$  291 nm. *Right:* Benesi-Hildebrand plot of  $1/(F_o-F)$  versus  $1/[\text{Sr}(\text{ClO}_4)_2]$  for **6c** upon titration with  $\text{Sr}(\text{ClO}_4)_2$  (0-12 equivalents). The linear fit showed a 1:1 complexation between **6c** and  $\text{Sr}^{2+}$  ions.....129

Figure 4-37. *Left:* Fluorescence response of chemosensor **6c** (1.50  $\mu\text{M}$ ) to various equivalents of  $\text{Mn}(\text{ClO}_4)_2$  in acetonitrile/chloroform (v/v= 9:1) solutions. The excitation wavelength was  $\lambda$  291 nm. *Right:* Benesi-Hildebrand plot of  $1/(F_o-F)$  versus  $1/[\text{Mn}(\text{ClO}_4)_2]$  for **6c** upon titration with  $\text{Mn}(\text{ClO}_4)_2$  (0-14 equivalents). The linear fit showed a 1:1 complexation between **6c** and  $\text{Mn}^{2+}$  ions.....129

Figure 4-38. *Left:* Fluorescence response of chemosensor **6c** (1.50  $\mu\text{M}$ ) to various equivalents of  $\text{Hg}(\text{ClO}_4)_2$  in acetonitrile/chloroform (v/v= 9:1) solutions. The excitation

wavelength was  $\lambda$  291 nm. *Right*: Benesi-Hildebrand plot of  $1/(F_o-F)$  versus  $1/[Hg(ClO_4)_2]$  for **6d** upon titration with  $Hg(ClO_4)_2$  (0-14 equivalents). The linear fit showed a 1:1 complexation between **6d** and  $Hg^{2+}$  ions .....130

Figure 4-39. *Left*: Fluorescence response of chemosensor **6c** (1.50  $\mu$ M) to various equivalents of  $Cu(ClO_4)_2$  in acetonitrile/chloroform (v/v= 9:1) solutions. The excitation wavelength was  $\lambda$  291 nm. *Right*: Benesi-Hildebrand plot of  $1/(F_o-F)$  versus  $1/[Cu(ClO_4)_2]$  for **6d** upon titration with  $Cu(ClO_4)_2$  (0-12 equivalents). The linear fit showed a 1:1 complexation between **6d** and  $Cu^{2+}$  ions .....130

Figure 4-40. *Left*: Fluorescence response of chemosensor **6c** (1.50  $\mu$ M) to various equivalents of  $Ca(ClO_4)_2$  in acetonitrile/chloroform (v/v= 9:1) solutions. The excitation wavelength was  $\lambda$  291 nm. *Right*: Benesi-Hildebrand plot of  $1/(F_o-F)$  versus  $1/[Ca(ClO_4)_2]$  for **6d** upon titration with  $Ca(ClO_4)_2$  (0-14 equivalents). The linear fit showed a 1:1 complexation between **6d** and  $Ca^{2+}$  ions .....131

Figure 4-41. *Left*: Fluorescence response of chemosensor **6c** (1.50  $\mu$ M) to various equivalents of  $Ba(ClO_4)_2$  in acetonitrile/chloroform (v/v= 9:1) solutions. The excitation wavelength was  $\lambda$  291 nm. *Right*: Benesi-Hildebrand plot of  $1/(F_o-F)$  versus  $1/[Ba(ClO_4)_2]$  for **6d** upon titration with  $Ba(ClO_4)_2$  (0-14 equivalents). The linear fit showed a 1:1 complexation between **6d** and  $Ba^{2+}$  ions .....131

Figure 4-42. *Left*: Fluorescence response of chemosensor **6c** (1.50  $\mu$ M) to various equivalents of  $Zn(ClO_4)_2$  in acetonitrile/chloroform (v/v= 9:1) solutions. The excitation wavelength was  $\lambda$  291 nm. *Right*: Benesi-Hildebrand plot of  $1/(F_o-F)$  versus

1/[Zn(ClO<sub>4</sub>)<sub>2</sub>] for **6d** upon titration with Zn(ClO<sub>4</sub>)<sub>2</sub> (0-9.7 equivalents). The linear fit showed a 1:1 complexation between **6d** and Zn<sup>2+</sup> ions .....132

Figure 4-43. *Left*: Fluorescence response of chemosensor **6c** (1.50 μM) to various equivalents of Cd(ClO<sub>4</sub>)<sub>2</sub> in acetonitrile/chloroform (v/v= 9:1) solutions. The excitation wavelength was λ 291 nm. *Right*: Benesi-Hildebrand plot of 1/(F<sub>o</sub>-F) versus 1/[Cd(ClO<sub>4</sub>)<sub>2</sub>] for **6d** upon titration with Cd(ClO<sub>4</sub>)<sub>2</sub> (0 -12 equivalents). The linear fit showed a 1:1 complexation between **6d** and Cd<sup>2+</sup> ions .....132

Figure 4-44. *Left*: Fluorescence response of chemosensor **6c** (1.50 μM) to various equivalents of Pb(ClO<sub>4</sub>)<sub>2</sub> in acetonitrile/chloroform (v/v= 9:1) solutions. The excitation wavelength was λ 291 nm. *Right*: Benesi-Hildebrand plot of 1/(F<sub>o</sub>-F) versus 1/[Pb(ClO<sub>4</sub>)<sub>2</sub>] for **6d** upon titration with Pb(ClO<sub>4</sub>)<sub>2</sub> (0-12equivalents). The linear fit showed a 1:1 complexation between **6d** and Pb<sup>2+</sup> ions.....133

Figure 4-45. *Left*: Fluorescence response of chemosensor **6c** (1.50 μM) to various equivalents of Mg(ClO<sub>4</sub>)<sub>2</sub> in acetonitrile/chloroform (v/v= 9:1) solutions. The excitation wavelength was λ 291 nm. *Right*: Benesi-Hildebrand plot of 1/(F<sub>o</sub>-F) versus 1/[Mg(ClO<sub>4</sub>)<sub>2</sub>] for **6d** upon titration with Mg(ClO<sub>4</sub>)<sub>2</sub> (0-12 equivalents). The linear fit showed a 1:1 complexation between **6d** and Mg<sup>2+</sup> ions .....133

Figure 4-46. *Left*: Fluorescence response of chemosensor **6c** (1.50 μM) to various equivalents of CsClO<sub>4</sub> in acetonitrile/chloroform (v/v= 9:1) solutions. The excitation wavelength was λ 291 nm. *Right*: Benesi-Hildebrand plot of 1/(F<sub>o</sub>-F) versus 1/[ CsClO<sub>4</sub>] for **6d** upon titration with CsClO<sub>4</sub> (0-12 equivalents). The linear fit showed a 1:1 complexation between **6d** and Cs<sup>+</sup> ions .....134

Figure 4-47. *Left:* Fluorescence response of chemosensor **6c** (1.50  $\mu\text{M}$ ) to various equivalents of  $\text{Co}(\text{ClO}_4)_2$  in acetonitrile/chloroform (v/v= 9:1) solutions. The excitation wavelength was  $\lambda$  291 nm. *Right:* Benesi-Hildebrand plot of  $1/(F_0-F)$  versus  $1/[\text{Co}(\text{ClO}_4)_2]$  for **6d** upon titration with  $\text{Co}(\text{ClO}_4)_2$  (0-14 equivalents). The linear fit showed a 1:1 complexation between **6d** and  $\text{Co}^{2+}$  ions .....134

Figure 4-48. *Left:* Fluorescence response of chemosensor **6c** (1.50  $\mu\text{M}$ ) to various equivalents of  $\text{Fe}(\text{ClO}_4)_2$  in acetonitrile/chloroform (v/v= 9:1) solutions. The excitation wavelength was  $\lambda$  291 nm. *Right:* Benesi-Hildebrand plot of  $1/(F_0-F)$  versus  $1/[\text{Fe}(\text{ClO}_4)_2]$  for **6d** upon titration with  $\text{Fe}(\text{ClO}_4)_2$  (0-14 equivalents). The linear fit showed a 1:1 complexation between **6d** and  $\text{Fe}^{2+}$  ions .....135

Figure 4-49. *Left:* Fluorescence response of chemosensor **6c** (1.50  $\mu\text{M}$ ) to various equivalents of  $\text{Ni}(\text{ClO}_4)_2$  in acetonitrile/chloroform (v/v= 9:1) solutions. The excitation wavelength was  $\lambda$  291 nm. *Right:* Benesi-Hildebrand plot of  $1/(F_0-F)$  versus  $1/[\text{Ni}(\text{ClO}_4)_2]$  for **6d** upon titration with  $\text{Ni}(\text{ClO}_4)_2$  (0-10 equivalents). The linear fit showed a 1:1 complexation between **6d** and  $\text{Ni}^{2+}$  ions .....135

Figure 4-50. *Left:* Fluorescence response of chemosensor **6c** (1.50  $\mu\text{M}$ ) to various equivalents of  $\text{AgClO}_4$  in acetonitrile/chloroform (v/v= 9:1) solutions. The excitation wavelength was  $\lambda$  291 nm. *Right:* Benesi-Hildebrand plot of  $1/(F_0-F)$  versus  $1/[\text{AgClO}_4]$  for **6d** upon titration with  $\text{AgClO}_4$  (0-14 equivalents). The linear fit showed a 1:1 complexation between **6d** and  $\text{Ag}^+$  ions .....136

Figure 4-51. *Left:* Fluorescence response of chemosensor **6c** (1.50  $\mu\text{M}$ ) to various equivalents of  $\text{Mn}(\text{ClO}_4)_2$  in acetonitrile/chloroform (v/v= 9:1) solutions. The excitation

wavelength was  $\lambda$  291 nm. *Right:* Benesi-Hildebrand plot of  $1/(F_0-F)$  versus  $1/[\text{Mn}(\text{ClO}_4)_2]$  for **6d** upon titration with  $\text{Mn}(\text{ClO}_4)_2$  (0-14 equivalents). The linear fit showed a 1:1 complexation between **6d** and  $\text{Mn}^{2+}$  ions .....136

## Chapter 1

### Introduction

#### 1.1 Calixarenes

Calixarenes are among the best-known members of the class of synthetic macrocyclic receptors which include cyclodextrins, crown ethers, and cucurbiturils.<sup>1-7</sup> Gustche<sup>8</sup> was the first person to introduce the name “calixarenes” for the cyclic oligomers obtained from condensing formaldehyde with *p-tert*-butylphenol under alkaline conditions. The word “calix” is derived from the Greek word “*Kalyx*” since the shape of the tetramer, which can adopt either a bowl or a vase-like conformation resembles that of a *kalyx krater* vase (Figure 1-1).

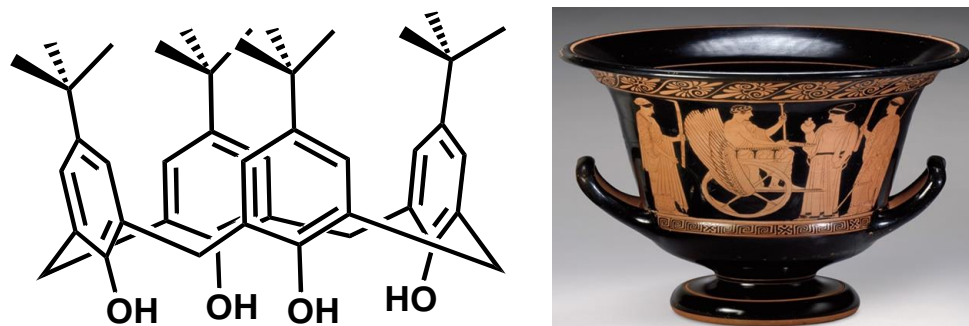


**Figure 1-1.** *p-tert*-butylcalix[4]arene and *kalyx krater* vase showing the resemblance in shape between the two. [Adapted with permission from Reference 8]

Calixarenes whose molecular structures, in general, consist of a cyclic array of methylene-bridged phenolic units have numerous conformational isomers since there are two main possible modes by which one, or more of the phenolic units can rotate through the annulus of the macrocycle, as shown in Figure 1-2 below. These two possible rotational modes are the “*para*-substituent-through-the annulus rotation” and the “oxygen-through-the annulus rotation”.

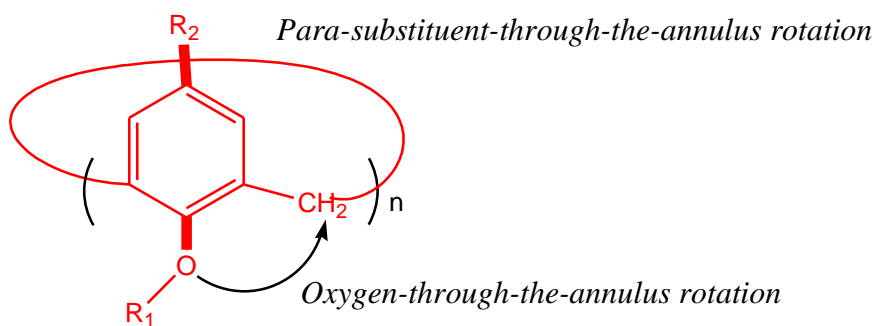


**Figure 1-2.** The two different modes for the inversion of the phenyl units.

In calixarenes, there are two distinguishable regions. These regions are the *para* positions of the aromatic rings and the phenolic OH groups. These regions are referred to as the “upper rim” (or “wide rim”) and the “lower rim” (or “narrow rim”), respectively (Figure 1-3). Each of these rims can be selectively functionalized. The adjacent units in calix[4]arene are referred to as the “proximal” (1,2) positions while the opposite nuclei are said to be the “distal” or “diametrical” (1,3) positions.

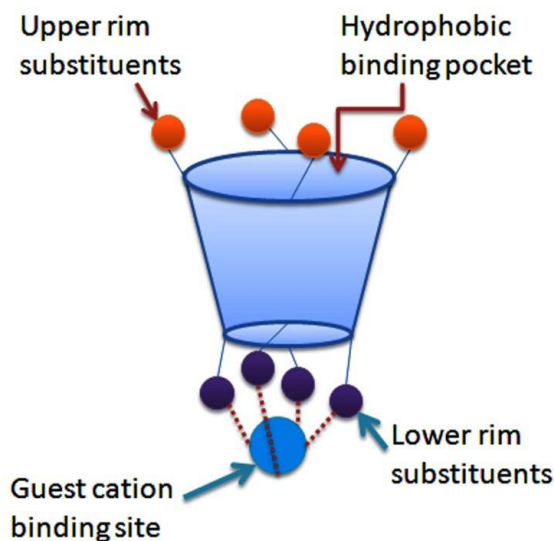


**Figure 1-3.** The anatomy of a calix[4]arene in the *cone* conformation. [Adapted with permission from Reference 1]

One of the main structural features of calixarenes is that they can have several conformations that result from the free rotation about the  $\sigma$ -bonds of the Ar-CH<sub>2</sub>-Ar groups. As shown in Figure 1-4, there can be at least four orientations for the phenol units for calix[4]arenes. There are four terms used for these four basic conformations. These terms are “*cone*”, “*partial cone*”, “*1,2-alternate*”, and “*1,3-alternate*”. The four conformations differ with respect to the orientation of the positions of the phenolic OH groups as well as the molecular planes (which are defined by the carbon atoms of the methylene bridges). In the case of calix[5]arene, a reference plane is also defined but this is not the case for larger oligomers.<sup>10</sup>

Although the phenolic units may rotate using the oxygen-through-the annulus rotation mechanism, the *cone* conformation is favorably adopted due to the stabilization derived from intramolecular hydrogen-bonding interactions among the OH groups when

these groups are not functionalized.<sup>9</sup> This implies that  $C_{4v}$ -symmetry is adopted for the *cone* conformer of *p-tert-butylcalix[4]arene* and that a cavity exists defined by the upper rim. The temperature, the solvent, and the *para* substituents of the calixarenes as well as the reactivity of the electrophile and the base used in functionalizing the lower rim are some of the factors that influence the conformations of the calix[4]arene derivatives.

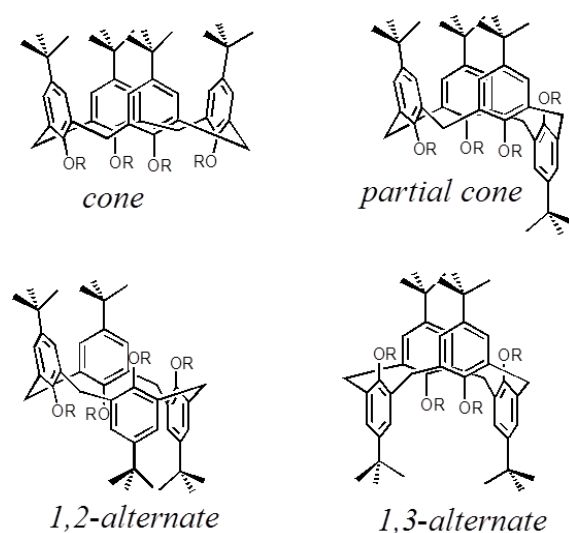


**Figure 1-4.** The four stable conformations of calix[4]arenes. [Adapted with permission from Reference 3]

Calixarenes have highly versatile frameworks and, therefore, they may act as hosts for anions, cations, and neutral molecules, depending on the degree of their functionality (Figure 1-5). Several factors have been shown to influence the ionophoric ability and cation selectivity of calixarene-based carriers and receptors. These factors include the size of the ring of the calixarene skeleton, its lipophilicity, its conformation

and conformational mobility, its chemical nature (donor ability), the spatial arrangement of the binding functionalities, as well as the degree of its preorganization.<sup>10</sup>

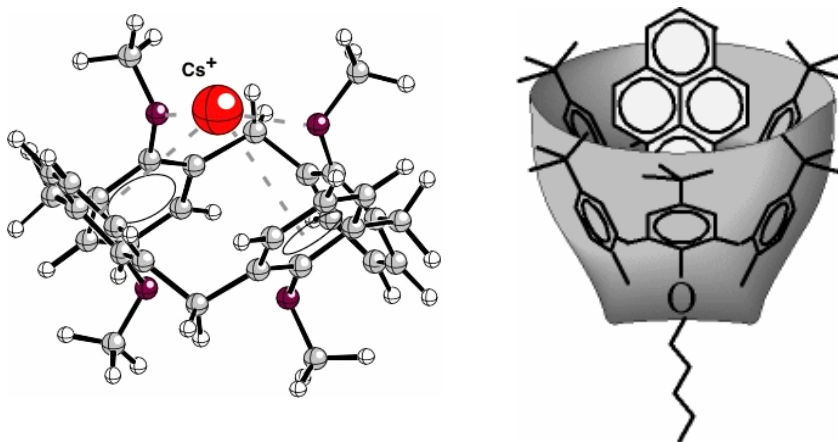


**Figure 1-5.** Examples of calixarene-guest complexes. [Adapted with permission from Reference 4]

Calixarenes are therefore able to encapsulate smaller molecules and ions in a reversible ("supramolecular") manner within their cavities. In the solid state, inclusion compounds can form with different "guest" compounds such as the solvents acetone, benzene, anisole, pyridine, toluene, acetonitrile, chloroform, methanol, or water. Not only does the chemical modification of calixarenes through the introduction of other functional groups enable the synthesis of new host molecules, it also facilitates the control of the calixarene's conformation. Calixarenes are highly superior in this function as compared to other macrocyclic molecules such as cyclodextrins or crown ethers.

When there is a partial or total change in the nature of the methylene groups of the bridge linkage then calixarene analogues such as those shown in Figure 1-6 are obtained. Three such calixarene analogues are shown in Figure 1-6; homotrioxacalix[3]arene(A),

hexahomoazacalix[3]arene(**B**), and tetrathiacalix[4]arene (**C**). Homotrioxacalix[3]arenes comprise a class of macrocyclic receptors that are analogous to calixarenes<sup>12</sup> in which some or all of the methylene bridges between the aromatic rings are replaced by -CH<sub>2</sub>OCH<sub>2</sub>- moieties. The bridge linkage can be -CH<sub>2</sub>CH<sub>2</sub>- or -CH<sub>2</sub>CH<sub>2</sub>CH<sub>2</sub>- for trihomocalixarenes<sup>13</sup>- or hexahomocalixarenes<sup>14</sup> while hetero analogues have -CH<sub>2</sub>OCH<sub>2</sub>-, or -CH<sub>2</sub>NRCH<sub>2</sub>-<sup>15</sup> (where R= alkyl groups, etc.), or sulfur as the bridge linkages.<sup>16</sup> These calixarene analogues have similar features to those of the classical calixarenes having only -CH<sub>2</sub>- bridges but yet also have differing properties that are due to these changed linkage group.

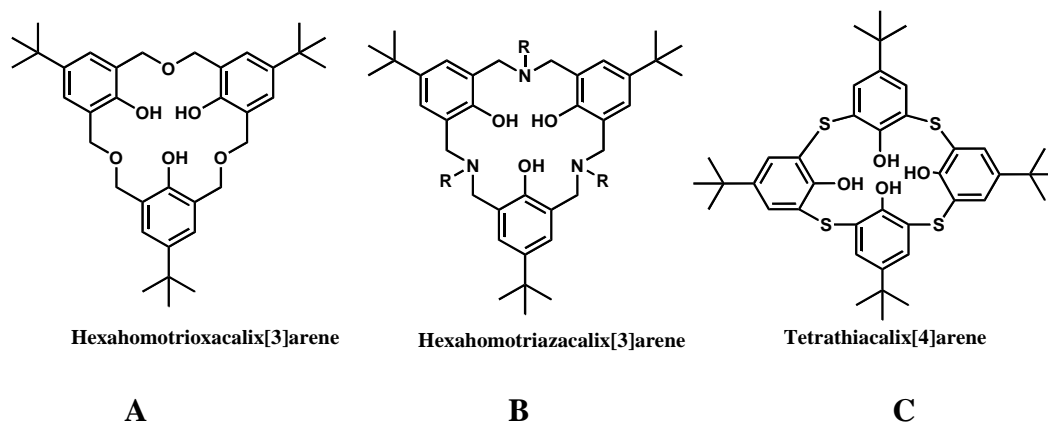


**Figure 1-6.** Some calixarene analogues.

## 1.2 Supramolecular chemistry

Supramolecular chemistry has advanced from studies with biological systems that mimicked weak non-covalent interactions, and is concerned with the phenomenon of

molecular recognition.<sup>17</sup> Supramolecular chemistry is characterized by the phenomenon in which target molecules are recognized by carefully-designed synthetic structures to form supramolecular complexes through non-covalent interactions. One of the leading proponents of supramolecular chemistry is Jean-Marie Lehn who, together with Charles J. Pedersen and Donald J. Cram, won the 1987 Nobel Prize in chemistry for “their development and use of molecules with structure-specific interactions of high selectivity” contributions to the field of supramolecular or host-guest chemistry. Lehn was particularly recognized for developing the chemistry of the cryptands as well as his efforts on the synthesis of artificial enzymes. In a more colloquial manner, supramolecular chemistry has been described as the “chemistry beyond the molecule”. In other definitions, phrases such as “non-molecular chemistry” and “the chemistry of the noncovalent bond” are also widely used. These definitions are demonstrated in Figure 1-7, which shows the relationship between molecular and supramolecular chemistry in both structure and function.

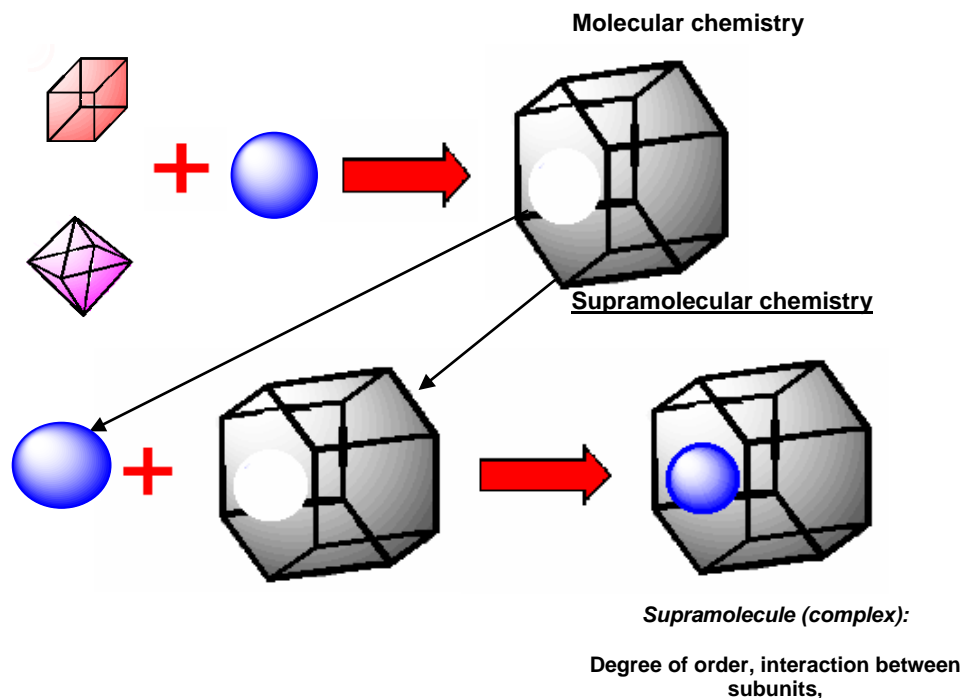


**Figure 1-7.** Comparison between the scope of molecular and supramolecular chemistry. [Adapted with permission from Reference 18]

In its simplest form, supramolecular chemistry may be regarded as involving some kind of noncovalent binding or a form of complexation event. On the basis of that consideration, the “host” molecule may then be considered as binding with another molecule or ionic moiety (“guest”) with the result being the formation of a “host-guest” complex or “supramolecule” or “supramolecular complex”. In most cases, the host is a large molecule or aggregate such as an enzyme or synthetic macrocyclic compound with a sizeable, central hole or cavity. On the other hand, the guest is usually a monoatomic cation, a simple inorganic anion, or a more sophisticated molecule such as a pheromone,

hormone, or neurotransmitter. The host can be defined as the molecular entity that possesses the convergent binding sites such as hydrogen-bond donors and Lewis basic donor atoms for the guest. On the other hand, the guest possesses the divergent binding sites such as spherical Lewis acidic metal cations or hydrogen-bond acceptor halide anions.<sup>18</sup>

### **1.3. Noncovalent interactions**

J. D. van der Waals was the first scientist to recognize noncovalent interactions (named van der Waals interactions after him) in the nineteenth century.<sup>19</sup> The role of van der Waals interactions in nature has been defined in greater detail during the past two decades. Unlike typical classical covalent interactions that are predominant in molecules, van der Waals interactions are weak, but nevertheless can bind together different kinds of building blocks into supramolecular entities.<sup>20</sup> Another difference between the two types of forces is that covalent bonds are shorter than 2 Å while the noncovalent interactions function within a range of up to several angstroms. Covalent bond formation involves the overlapping of partially-occupied orbitals of interacting atoms that share a pair of electrons. In contrast, noncovalent interactions do not always require overlapping orbitals because the attraction originates from the electrical properties of the building blocks.

The van der Waals forces or noncovalent interactions that are involved in supramolecular entities usually consist of a combination of several different types of interactions. These interactions may include hydrogen bonding, ion-pairing, cation- $\pi$ , and  $\pi$ - $\pi$  interactions, among others. The term “noncovalent” therefore can include a wide range of repulsive or attractive forces.<sup>19</sup> These include interactions between a permanent

multipole and an induced multipole, between two permanent multipoles, and between a time-variable multipole and an induced multipole. The stabilizing energy of the noncovalent complexes generally comprises several energy contributions which include induction, electrostatic (or Coulombic), charge–transfer, and dispersion. The repulsive contribution, (also referred to as exchange-repulsion) helps in preventing the subsystems from drawing too close together. The term “induction” is used to refer to the ability of charged molecules to polarize the neighboring species. Dispersion (London) interactions emanate from the interactions between two fluctuating multipoles. The charge-transfer (CT) interactions involve the flow of electrons from the donor to the acceptor. The term van der Waals forces is often employed in describing the dispersion and exchange-repulsion contributions. However, other long-range contributions may be included in the definition of van der Waals forces. A common feature of all these interactions is that they involve the host, the guest and their surroundings.<sup>19,20</sup>

### **1.3.1. Ion pairing**

Electrostatic (Coulombic) interactions are the driving forces in ion pairing. Electrostatic interactions also play an important role in natural and in supramolecular systems. In organic ions, charges are heavily delocalized and this complicates the theoretical analysis of ion pairing. In order to make the understanding of ion pairs easy, theoretical interpretations of the association constant ( $K_{assoc}$ ) based on Debye–Hückel theory have been described by Bjerrum (spherical ions with point charges) and Fuoss (contact ion pairs). Poisson introduced a numerical method that allows the consideration

of solvent molecules while Manning's counterion condensation theory satisfactorily describes the salt effect.<sup>21</sup>

### 1.3.2. Dipole-dipole interactions

The interactions between permanently polar molecules or groups are described as dipole-dipole interactions. In molecules with carbonyl groups, for instance, the alignment of one dipole with another may result in the occurrence of significant attractive interactions due to the matching of a single pair of poles on adjacent molecules ("Type I"). The attractions may also result from the opposing alignment of one dipole with another ("Type II").<sup>17</sup> It has been shown through calculations that Type II interactions have energy of about 20 kJ/mol when they are in the solid state (Figure 1-8). However, they are relatively weaker when in solution.

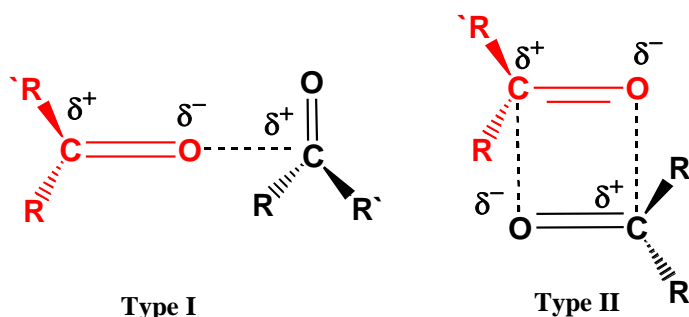


**Figure 1-8.** Dipole-dipole interactions between two carbonyl group. [Adapted with permission from Reference 17]

### 1.3.3. Hydrogen bonding

Hydrogen bonding is perhaps the most important noncovalent interaction.<sup>17</sup> It is one of the most important sources of stabilizing forces for supramolecular complexes.

Hydrogen bonding is the interaction that exists between a hydrogen atom that is covalently bonded to a strongly electronegative donor such as oxygen, nitrogen, or fluorine.<sup>18</sup> Hydrogen bonds also contain an electronegative atom (hydrogen-bond acceptor) such as chlorine, oxygen, and fluorine, which have at least a single lone electron pair. A hydrogen bond may be represented as **D–H...A**, with **D** and **A** representing the hydrogen bond donor and acceptor respectively.<sup>19</sup> The hydrogen bond strength depends on the angle between **D–H...A** as well as the distance between **A** and **H**. For hydrogen bonding to occur it is thought that the distance between **A** and **H** should not exceed the sum of the van der Waals radii of the hydrogen atom and the acceptor atom. Figure 1-9 shows the different types of hydrogen bonds. The last two (bifurcated and three-centered bifurcated) hydrogen bonds are less frequent.<sup>20</sup>

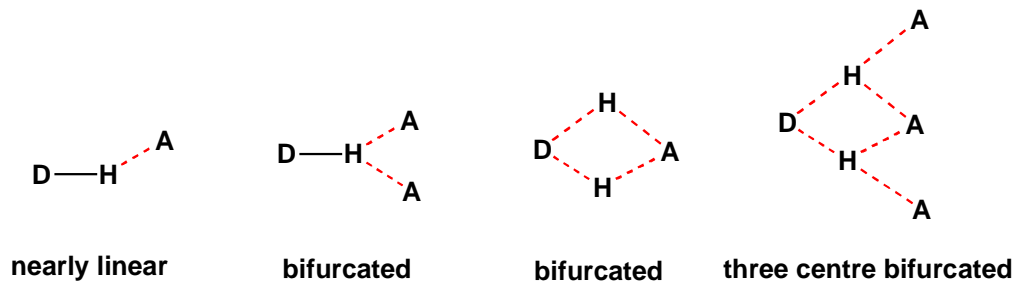


**Figure 1-9.** Hydrogen bonds between donor D and acceptor A atoms. [Adapted with permission from Reference 19]

The table below shows the common classification of hydrogen bonds based on their strengths as well as their properties (Table 1-1)

**Table 1-1.** Classification and some properties of hydrogen bonds. [Adapted with permission from Reference 19]

D-H-----A interaction	Strong	Moderate	Weak
	Mainly covalent	Mainly Electrostatic	Electrostatic
Bond energy (kJmol <sup>-1</sup> )	60–120	16–60	< 12
Bond lengths (Å): H-----A	1.2–1.5	1.5–2.2	2.2–3.2
Bond lengths (Å): D-----A	2.2–2.5	2.5–3.2	3.2–4.0
Bond angle	175–180	130–180	90–150
Examples	Gas phase dimers with strong acids/bases, HF complexes	Acids, Biological molecules	C-H--N/O and N/O--H-- <i>p</i> hydrogen bonds

The concept of hydrogen bonding has been extended to describe weaker C–H ...O types of interactions such as (CH<sub>3</sub>)<sub>2</sub>CO...HCCl<sub>3</sub> in solutions of acetone and chloroform. However, these concepts have been systematically studied only in the recent past.<sup>22-26</sup>

#### 1.3.4. Cation– $\pi$ interactions

These are the strong forces which exist between the cations and the  $\pi$ -face of an aromatic structure.<sup>23</sup> Electrostatic forces seem to play a dominant role in these interactions although modern theories also suggest that polarizability, induced dipole, dispersion, and charge-transfer are also important. Figure 1-10 illustrates the roles played by the charge distribution in an aromatic ring and electrostatic interactions. With K<sup>+</sup> the quadrupole moment of benzene is shown as the two opposing dipoles.<sup>24</sup>

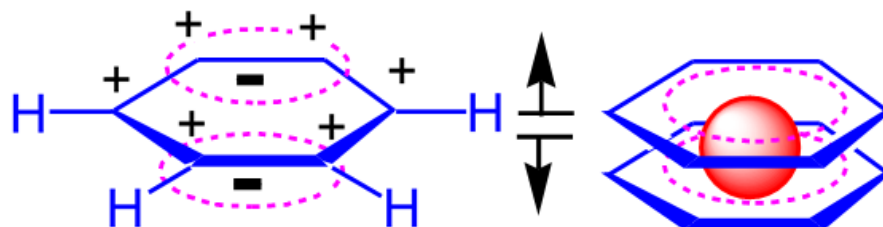


**Figure 1-10.** Schematic representation of cation- $\pi$  interactions showing the contact of  $K^+$  ion and benzene. The quadrupolar moment of benzene is represented as the two opposing dipoles. [Adapted with permission from Reference 24]

### 1.3.5. Aromatic $\pi$ - $\pi$ interactions

The weak electrostatic interactions that exist between aromatic rings are referred to as  $\pi$ - $\pi$  stacking interactions. In these interactions, one aromatic ring is electron-poor while the other one is electron-rich.<sup>20,27-28</sup> The induced dipole and dispersion contributions are also part of the stabilizing energy existing in  $\pi$ - $\pi$  interactions. Two types of  $\pi$ - $\pi$  stacking interactions, the face-to-face and edge-to-face interactions are shown (Figure 1-11a). The edge-to-face interactions are actually C-H- $\pi$  interactions but with the C-H bond having a smaller dipole moment. The attractions in the face-to-face and edge-to-face interactions originate from the interactions between slightly positively-charged hydrogen atoms and the negatively-charged  $\pi$ -face of the aromatic system. It is unlikely to have a perfect facial alignment for the face-to-face orientation due to the electrostatic repulsion that exists between the two negatively-charged  $\pi$ -systems of the aromatic rings, as shown in Figure 1-11b. The two aromatic  $\pi$ - $\pi$  faces have a distance of about 3.3–3.8 Å between them.<sup>20,28</sup>

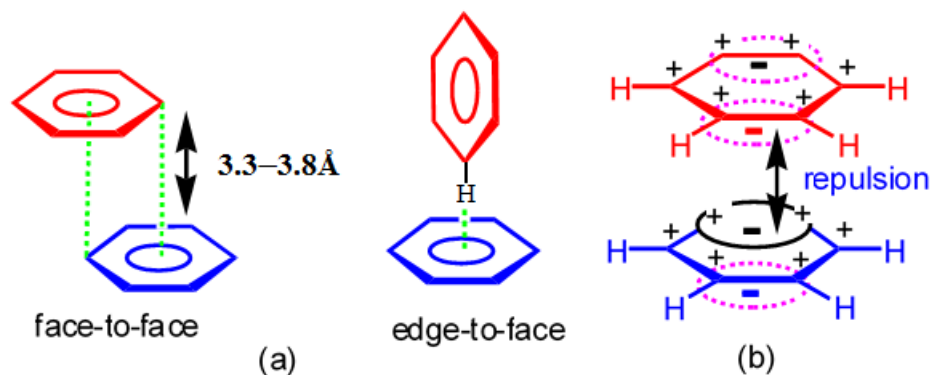


**Figure 1-11.** (a) The limiting types of aromatic  $\pi$ - $\pi$  interactions: face-to-face (interplanar distance about 3.3–3.8 Å) and edge-to-face orientations. (b) The repulsion between negatively charged  $\pi$ -electron clouds of facially oriented aromatic rings. [Adapted with permission from Reference 27]

## 1.4 Characterization of host-guest complexation

The determination of host-guest complexation may involve several analytical techniques including mass spectroscopy (MS), fluorescence spectroscopy (FS), nuclear magnetic resonance (NMR) spectroscopy, single crystal X-ray diffraction, and UV-visible spectroscopy (UV-vis). The most commonly used techniques are the FS and NMR spectroscopy because they offer the benefit of being able to characterize the complexation through detection of spectroscopic feature changes of the guest and or the host. In addition, these techniques generate information about the stoichiometry of the host-guest complexation, the binding constant, and the host-guest binding location.

### 1.4.1 Nuclear magnetic resonance (NMR) spectroscopy

NMR spectroscopy is among the most commonly used techniques of detecting and measuring host-guest complexation. The method is used for detecting the chemical

shift changes ( $\Delta\delta$  ppm) that occur as a result of changes in the respective protons' environment that shield or deshield the host and the guest.<sup>29</sup> Therefore, important information about the location of the interaction between the host and the guest may be obtained. In addition, the observed chemical shift changes ( $\Delta\delta$  ppm) can be employed in determining the binding constants between host and guest. The variations seen in the chemical shift changes  $\Delta\delta$  of the host and guest protons are affected by the speed of the exchange between the host and the guest with regard to the NMR time-scale. The NMR time-scale is the difference in frequency (Hz) between the two exchanging sites. The NMR time-scale is dependent on the spectrometer frequency as well as the nucleus considered (for instance,  $^1\text{H}$ ,  $^{13}\text{C}$ , and so on). The system exchange are of two different cases.<sup>30</sup>

- a) *Slow exchange system* where the rate of nucleus exchange between the guest/host-guest states is slower than the timescale of the NMR ( $K_{assoc} < \delta\nu$ ).
- b) *The fast exchange system* in which the rate of nucleus exchange between the two states is faster than the NMR time-scale ( $K_{assoc} > \delta\nu$ ).

$^1\text{H}$ -NMR spectroscopy is a more useful technique for studying host-guest complexation compared to  $^{13}\text{C}$  and  $^{31}\text{P}$ -NMR because the subject protons e.g. in the host, are closer to the molecule's exterior and, therefore are more exposed to other guest molecules or ionic species; in particular, the  $^{13}\text{C}$ -NMR chemical shifts are less responsive to intermolecular interactions. Longer acquisition times are also required since the  $^{13}\text{C}$  nucleus has a relatively poor sensitivity, with a natural abundance of only 1.1%.<sup>31</sup>

## **1.4.2 Photophysics of fluorescent chemosensors**

### **1.4.2.1 Principle of fluorescent chemosensors**

The Perrin–Jablonski diagram (Figure 1-12) is convenient for visualization of the possible photophysical processes which occur in fluorescence spectroscopy.<sup>32</sup> These processes include internal conversion(IC), photon absorption, intersystem crossing (ISC), fluorescence, delayed fluorescence, phosphorescence and triplet–triplet transitions. The singlet electronic states are denoted as  $S_0$  (the fundamental electronic state),  $S_1$ ,  $S_2$  and so on while the triplet states are denoted as  $T_1$ ,  $T_2$ , and so on. For each electronic state, there is a corresponding set of vibrational levels associated with it. The emission of photons that is accompanied by  $S_1 \rightarrow S_0$  relaxation is referred to as fluorescence. Due to the strong influence of the surrounding medium on fluorescence emission, the fluorescent molecules are usually used as probes in investigations of biochemical and biological systems, where they are commonly referred to as fluorescent probes.<sup>33</sup>

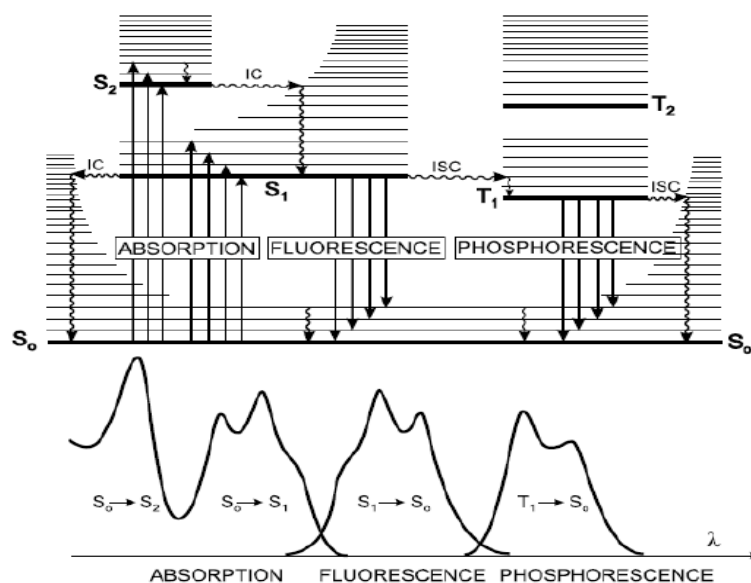


**Figure 1-12.** Perrin–Jablonski diagram and illustration of the relative positions of absorption, fluorescence and phosphorescence spectra. [Adapted with permission from Reference 33]

One of the major issues in the design of an effective chemosensor is the association of a selective molecular recognition event with a physical signal that is highly sensitive to its occurrence as shown in Figure 1-13. An effective fluorescent chemosensor usually consists of an ion recognition unit (ionophore) and a fluorogenic unit (fluorophore). Both of these moieties may be independent species but may also be covalently linked by a spacer.<sup>34</sup> For selective binding of the substrate to occur, the ionophore is required while the fluorophore acts as a means of monitoring the potential inhibition by the guest species. The response of a fluorophore to substrate binding is controlled by several mechanisms, which include photoinduced electron transfer (PET),<sup>35</sup> photoinduced charge transfer (PCT),<sup>36</sup> and excimer formation or extinction.

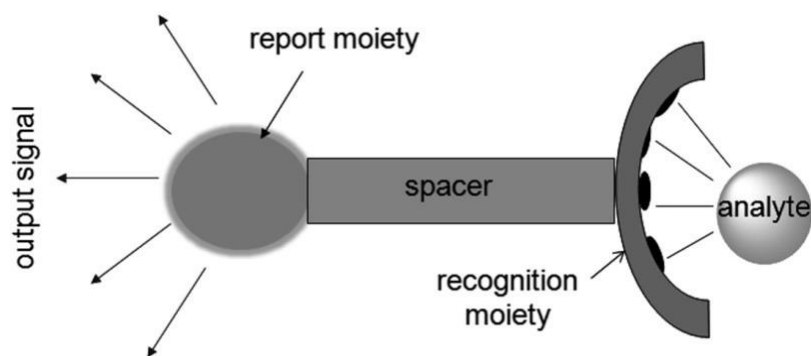


**Figure 1-13.** Diagram of an effective fluorescent chemosensor. [Adapted with permission from Reference 34]

Changes in the absorption and emission of light may be utilized as signals. However, appropriate chromophores or fluorophores must be available in addition to two important classes of sensors, the fluorimetric and optical absorption types. Fluorimetry is usually considered superior compared to absorption spectrophotometry although both methods are relatively simple techniques that are performed rapidly, are nondestructive and suited to multicomponent analysis. The superiority of fluorimetry over absorption spectrophotometry is due to its greater sensitivity.<sup>37</sup> Usually, absorbance measurements are best determined at concentrations lower than  $1 \times 10^{-7}$  M. Another advantage of fluorimetry is that it makes discrimination between analytes possible by time-resolved measurements.<sup>38</sup>

#### 1.4.2.2 Photoinduced electron transfer (PET)

In the simplest case, fluorescence (emission of a photon) follows a HOMO-to-LUMO excitation of electrons in a molecule. If the emission is efficient, then the molecule is termed a fluorophore. A “Stokes shift” may arise from the vibrational

deactivation of the excited state prior to emission. The “Stokes shift” occurs when the wavelength of the emitted radiation is longer than that of the exciting radiation.<sup>39</sup> There are various other interactions that may affect the emission process. Such interactions are of considerable importance with respect to the analytical applications of fluorescence. Therefore, when a single electron pair occupies a fluorophore orbital or is located on an adjacent molecule and the energy of the orbital lies between the energies of the HOMO and LUMO, there may be an efficient electron transfer of one of the electrons in the pair to the hole in the HOMO that is created by light absorption. The transfer of the initially excited electron to the lone pair orbital follows. The PET provides a mechanism for nonradiative deactivation of the excited state as shown in Figure 1-14. This leads to a decrease in the emission intensity or “quenching” of fluorescence.<sup>40</sup>

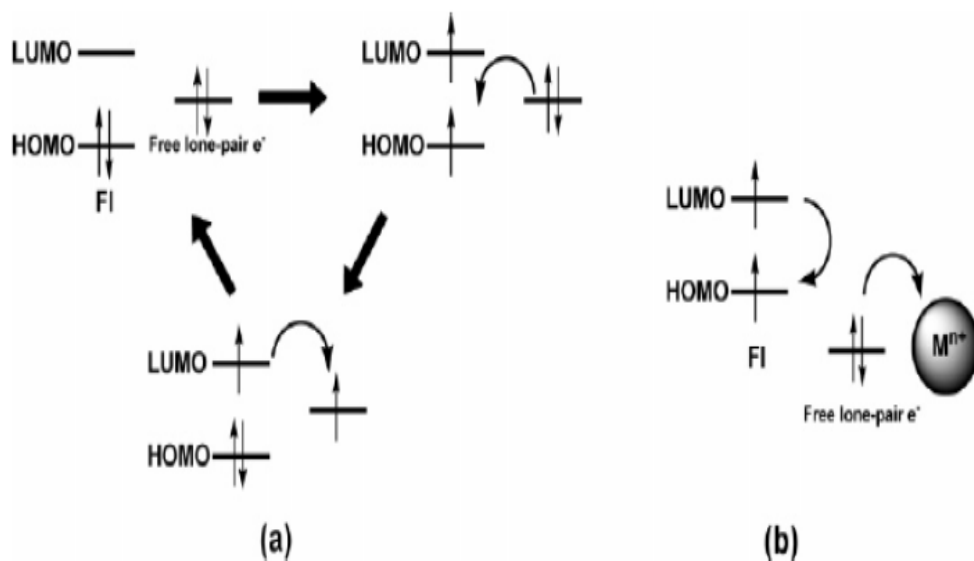


**Figure 1-14.** Mechanisms for PET (a) and CHEF (b) systems. [Adapted with permission from Reference 40]

The fluorescence that is lost due to PET can be recovered if the lone pair in the

bonding reaction can be involved. Therefore, the protonation or binding of a metal ion is effective in placing the electron pair in an orbital that is of lower energy and that inhibits the process of electron-transfer. The energy of the excited state may then be lost through radiative emission. This effect is known as chelation-enhanced fluorescence (CHEF) <sup>41</sup> when it occurs for a metal ion binding case.

### 1.4.2.3 Photoinduced charge-transfer (PCT)

Some degree of charge-transfer is involved for electronic excitation to take place. However, this charge-transfer may occur over long distances and be associated with major dipole moment changes in fluorophores containing both electron-withdrawing and electron-donating substituents. This makes the process sensitive to the fluorophore's microenvironment. Therefore, it may be expected that anions or cations that are close enough to interaction with the donating or accepting moiety will change the fluorophore's photophysical properties.<sup>42</sup>

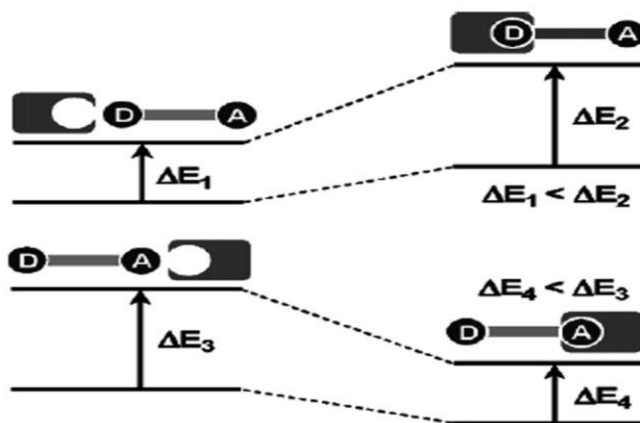


**Figure 1-15.** A PCT system. [Adapted with permission from Reference 43]

The electron-donating character of a donor group is usually reduced upon cation complexation of an electron donor group within a fluorophore. The conjugation that results from the complexation causes a blue shift in the absorption spectrum along with a reduction in the molar absorptivity. In contrast, the binding of the metal ion to the acceptor group causes an enhancement of its electron-withdrawing character. Therefore, the absorption spectrum becomes red-shifted with an increase in molar absorptivity (Figure 1-15).<sup>43</sup> The fluorescence spectra usually shift in the same direction as the absorption spectra. In addition to these shifts, changes in the quantum yields and lifetimes may be observed. The charge and the size of the cation are the key determining factor for these photophysical effects, and therefore, some selectivity is expected.

#### **1.4.2.4 Excimer formation**

In cases where aromatic rings are involved in weak interactions such as  $\pi$ -stacking which bring them to within van der Waals contact distances, the electronic excitation of one of the rings may result in enhanced interaction with its neighbor. This causes a condition termed an excited state dimer or “excimer.”<sup>44</sup> By definition, an excimer is a complex that is formed through the interaction between an excited fluorophore and another fluorophore that is in its ground state. Excimer emission usually gives a broad fluorescence band without vibrational structure. For most aromatic molecules, the maximum shift is about  $6000\text{ cm}^{-1}$  to lower energies, as compared to that of the uncomplexed (“monomer”) fluorophore emission.<sup>45</sup> If interaction develops within the lifetime of an excited monomer, then an excimer may form under such circumstances. Therefore, it is expected that excimers should be more likely to be produced by relatively

long-lived monomer excited states.<sup>46</sup> The rates of fluorophore diffusion, particularly in viscous solvents, are therefore an important limitation on excimer formation.<sup>47</sup> It is possible to control the separation and relative orientation of multiple fluorophore units attached to ligands through metal ion coordination. This facilitates the monitoring of the recognition by employing the monomer excimer fluorescence intensity ratio.

### 1.5 Determination of the association constant ( $K_{assoc}$ )

As stated earlier, the most commonly used methods for the quantitative measurement of the relative strength of the complexations in host-guest solution chemistry, are NMR spectroscopy, and spectrophotometry. In general, higher host-guest interactions in solution are associated with higher association, binding, or stability constants.<sup>48</sup> These are given as  $K_{assoc}$  values. A method of determining the stoichiometry of host-guest binding was elucidated by Job<sup>49</sup> in 1928. In this method, the guest's mole fraction may be plotted against the observed UV-vis absorbance changes at a specific wavelength. Alternatively, the mole fraction of the guest may be plotted using the NMR observed chemical shift changes of the guest or host protons ( $\Delta\delta$ ). The stoichiometry of binding may be determined from the shape of the titration curves that result. In order to calculate the free host's  $K_{assoc}$  concentrations, several factors are taken into account including the free guest and the host-guest complex. For a binding involving a 1:1 ratio, the equilibrium state may be presented as follows:



In the equilibrium equation, **H** and **G** represent the host and guest respectively

while the H:G represent the host-guest complex. For such a system, the  $K_{assoc}$  may be calculated as shown in the equation below:

$$K_{assoc} = [\text{H:G}] / ([\text{H}] \times [\text{G}]) \quad \text{Equation 1.2}$$

For the above Equation 1.2, [H] and [G] represent the concentrations of the host and guest at equilibrium respectively while [H:G] represent the concentration of the host-guest complex at the equilibrium state. Where one more host has the ability to bind to the guest, the equilibrium in such a case is represented by Equation 1.1 and Equation 1.3 as follows:



The  $K_{assoc}$  of such a system may be calculated as shown in the equation below:

$$K_{assoc} = [\text{H}_2\text{G}] / ([\text{H}] \times [\text{H:G}]) \quad \text{Equation 1.4}$$

Using the <sup>1</sup>H-NMR titration data, it is possible to determine  $K_{assoc}$  by plotting the concentration of the host ([H]) or guest ([G]) against the changes in the chemical shifts and using a non-linear curve 1:1 binding constant isotherm according to Connors.<sup>48</sup> In a Benesi-Hildebrand treatment, the calculation involves plotting (1/[G]) or (1/[H]) against (1/Δδ) to obtain a linear curve. The  $K_{assoc}$  of such a system is calculated as shown in the equation below.<sup>50</sup>

$$K_{assoc} = \text{intercept/slope} \quad \text{Equation 1.5}$$

## 1.6 References

1. Vicens, J.; Böhmer, V. *Calixarenes: A Versatile Class of Macrocyclic Compounds*, Eds.; Kluwer Academic: Dordrecht, 1991.
2. Ikeda, A.; Shinkai, S. *Chem. Rev.* **1997**, *97*, 1713-1718.
3. Gutsche, C. D. *Calixarenes, An Introduction*, Royal Society of Chemistry: Cambridge, U.K., 2008.
4. Asfari, Z.; Böhmer, V.; Harrowfield, J.; Vicens, J. *Calixarenes 2001*, Eds; Kluwer Academic: Dordrecht, 2001.
5. Morohashi, N.; Narumi, F.; Iki, N.; Hattori, T.; Miyano, S. *Chem. Rev.* **2006**, *106*, 5291-5316.
6. Kim, J. S.; Quang, D. T. *Chem. Rev.* **2007**, *107*, 3780-3788.
7. Coquière, D.; Le Gac, S.; Darbost, U.; Sénèque, O.; Jabin, I.; Reinaud, O. *Org. Biomol. Chem.* **2009**, *7*, 2485-2495.
8. Gutsche, C. D. *In Calixarenes Revisited*. Royal Society of Chemistry, Cambridge, 1998.
9. Gutsche, C. D. *Acc. Chem. Res.* **1993**, *16*, 161-169.
10. Vicens, J.; Böhmer, V. *In Calixarenes: A Versatile Class of Macrocyclic Compounds*, Kluwer Academic Publishers, Cambridge, 1990.
11. Andreetti, G. D.; Ungaro, R.; Pochini, A. *J. Chem. Soc., Chem. Commun.* **1979**, *22*, 1005-1014.
12. Gutsche, C. D. *Calixarenes, Monographs in Supramolecular Chemistry*; Stoddart, J. F.

Ed. The Royal Society of Chemistry: London, 1989, Vol. 1.

13. Vögtle, F.; Schmitz, J.; Nieger, M. *Chem. Ber.* **1992**, *125*, 2523-2532.
14. Yamato, T.; Sakaue, N.; Tanaka, K.; Tsuzuki, H. *New J. Chem.* **2001**, *25*, 434-444. (b)  
Yamato, T.; Saruwatari, Y.; Yasumatsu, M. *J. Chem. Soc. Perkin Trans. 1* **1997**, 1731-1739.
15. Hampton, P. D.; Tong, W.; Wu, S.; Duesler, E. N. *J. Chem. Soc. Perkin Trans.* **1996**, *2*, 1127-1133.
16. Lhoták, P.; Himl, M.; Pakhomova, S.; Stibor, I. *Tetrahedron Lett.* **1998**, *39*, 8915-8923.
17. Steed, J. W.; Atwood, J. L. *Supramolecular Chemistry*, John Wiley & Sons Ltd, Chichester, England, 2002.
18. Lehn, J. M. *Science*, **1985**, *227*, 849-855.
19. Müller-Dethlefs, K.; Hobza, P. *Chem. Rev.* **2000**, *100(1)*, 143-168.
20. Schneider, H. J.; Yatsimirsky, A. In *Principles and methods in supramolecular chemistry*, John Wiley & Sons Ltd, Chichester, England, 2000.
21. Hossain, M. A.; Schneider, H. J. *Chem. Eur. J.* **1999**, *5*, 1284-1290.
22. Steiner, T. *Chem. Commun.* **1997**, 727-734.
23. Steiner, T. *New J. Chem.* **1998**, 1099-1103.
24. Steiner, T.; Desiraju R. *Chem. Commun.* **1998**, 891-892.
25. De Wall, S. L.; Meadows, E.S.; Barbour, L. J.; Gokel, G. W. *Chem. Commun.* **1999**, 1553-1554.
26. Ma, J. C.; Dougherty, D. A. *Chem. Rev.* **1997**, *97*, 1303-1324.

27. Lämsä, M.; Raitamaa, K.; Pursiainen, J. *J. Phys. Org. Chem.* **1999**, *12*, 557-563. (b)  
Lämsä, M.; Pursiainen, J.; Rissanen, K.; Huuskonen, J. *Acta. Chem. Scand.* **1998**, *52*, 563-570.
28. Jeong, K. S.; Cho, Y. L.; Pyun, S. Y. *Tetrahedron Lett.* **1995**, *36*, 2827-2830.
29. Schneider, H. J.; Yatsimirsky, A. K. *Principles and Methods in Supramolecular Chemistry*, John Wiley & Sons Ltd.: Chichester, 2000.
30. Sanders, J. K. M.; Hunter, B.K. *Modern NMR Spectroscopy. A Guide for Chemists*, Oxford University Press: Oxford, 1988.
31. Moser, A.; Detellier, C. *Nuclear Magnetic Resonance Spectroscopy, In Encyclopedia Of Supramolecular Chemistry*, Marcel Dekker Inc.: New York, 2004.
32. Ford, G. W.; Weber, W. H. *Phys. Rep.* **1984**, *113*, 195-287.
33. Strianese, M.; Staiano, M.; Ruggiero, G.; Labella, T.; Pellicchia, C.; D'Auria, S. *Methods Mol Biol.* **2012**; *875*, 193-216.
34. Wiskur, S. L.; Ait-Haddou, H.; Lavigne, J. J.; Anslyn, E. V. *Acc. Chem. Res.* **2001**, *34*, 963-970.
35. Jin, T.; Ichikawa, K.; Koyama, T. *J. Chem. Soc., Chem. Commun.* **1992**, 499, 378-386.
36. Ungaro, R.; Pochini, A. In *Frontiers in Supramolecular Organic Chemistry and Photochemistry*; Schneider, H.-J., Ed.; VCH: Weinheim, Germany, 1991.
37. Valeur, B.; Leray, I. *Inorg. Chim. Acta* **2007**, *360*, 765.
38. Valeur, B. *Molecular Fluorescence*; Wiley-VCH: Weinheim, Germany, 2001.
39. Lakowicz, J. R. *Principles of Fluorescence Spectroscopy*, Ed. Plenum Publishers Corp.: New York, 1999.
40. Kim, J. S.; Noh, K. H.; Lee, S. H.; Kim, S. K.; Kim, S. K.; Yoon, J. *J. Org. Chem.* **2003**,

- 68, 597-604.
41. Kim, J. S.; Shon, O. J.; Rim, J. A.; Kim, S. K.; Yoon, J. *J. Org. Chem.* **2002**, *67*, 2348-2356.
42. Rettig, W.; Lapouyade, R. In *Probe Design and Chemical Sensing*; Lakowicz, J. R., Ed.; Topics in Fluorescence Spectroscopy; Plenum: New York, 1994; Vol. 4, p 109.
43. Löhr, H. G.; Vögtle, F. *Acc. Chem. Res.* **1985**, *18*, 65-73.
44. Birks, J. B. *Photophysics of Aromatic Molecules*; John Wiley: New York, 1970; Chapter 7.
45. Birks, J. B.; Lumb, M. D.; Munro, I. H. *Proc. R. Soc. London* **1964**, *A280*, 289-297.
46. Lee, J. Y.; Kim, S. K.; Jung, J. H.; Kim, J. S. *J. Org. Chem.* **2005**, *70*, 1463-1471.
47. Winnik, M. A. *Chem. Rev.* **1981**, *81*, 491-498.
48. Connors, K. A. *Binding Constants*, Wiley: New York, 1987.
49. Job, P. *Ann. Chim.* **1928**, *9*, 113-203.
50. Fielding, L. *Tetrahedron* **2000**, *56*, 6151-6170.

## Chapter 2

# Complexation Properties of Upper- and Lower-rim Functionalized Calix[4]arene

### 2.1 Introduction

The nanotechnological applications of calixarenes have attracted significant interest and much research work is ongoing in this field.<sup>1a-c</sup> One of the key structural features of calixarenes is that their basic molecular architectures are robust due to the presence of the four phenyl rings, and for the case of calix[4]arenes, these rings are linked to form a bowl-like array (Figure 2-1). Selective chemical modification of both the lower- and upper rims of calixarenes is possible to produce a huge number of derivatives<sup>2</sup> with molecular receptor or “host-guest” properties that may be fine-tuned. Calixarenes that are so modified may selectively bind or complex with a variety of neutral, cationic or anionic “guests”.

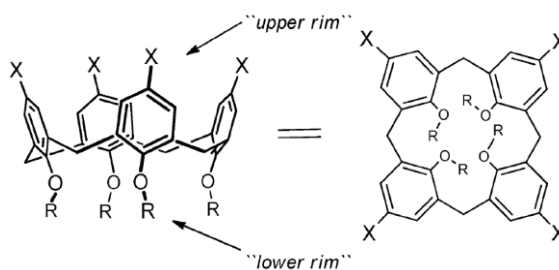


**Figure 2-1.** Two different forms of representations of the structure of a calix[4]arene showing the “upper” and “lower” rims, which can have different functional groups represented as “X” and “R” respectively. [Adapted with permission from Reference 14]

Many studies have been reported on the complexation of modified calixarenes in solution-phase with different ionic and non-ionic guests.<sup>3</sup> Recently, attention has been directed towards the calixarenes' host-guest sensing properties on solid surfaces.<sup>4,5</sup>

### 2.1.1 Gold-supported calixarenes

In the construction of most devices and systems with applications in the nanotechnology field,<sup>6,7</sup> a self-assembled monolayer (SAM) of thiols on gold forms the key elements. Figure 2-2 shows an example of a calixarene narrow rim thiol-functionalized derivative on a SAM onto gold surface. The reduction of gold to nanoscale gold particles changes the optical properties which now become dominated by the collective oscillation of the gold surface electrons that resonate with incident electromagnetic radiation. This phenomenon is known as the surface plasmon resonance (SPR). Consequently, the SPR absorption band and the color of an AuNP solution depends on several parameters, which include the type of gold, the size and shape of the particle, the medium's dielectric properties as well as the distance between the particles.<sup>8-10</sup>

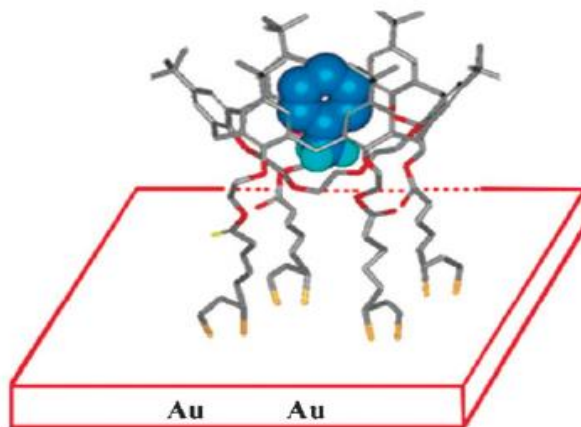


**Figure 2-2.** Gold-supported single calixarene from a SAM, with an aniline guest. [Adapted with permission from Reference 13].

### 2.1.2 Cation sensors

The method developed by Chen et al. based on SPR measurements is very useful for  $K^+$  sensing with high sensitivity as well as selectivity using SAMs of a calix[4]-crown-5 derivative-modified gold chip.<sup>11</sup> A more sensitive and selective sensing is exhibited by the compound monolayer towards the  $K^+$  ion over other alkali metal cations and alkaline earth metal cations. The SPR angle shift at the highest concentration of the  $K^+$  ion (0.01 M) is 0.381 as shown in Figure 2-3. These observations may be attributed to strong host-guest interactions that occur between the preorganized calix[4]crown-5 derivative monolayer and the  $K^+$  ion.

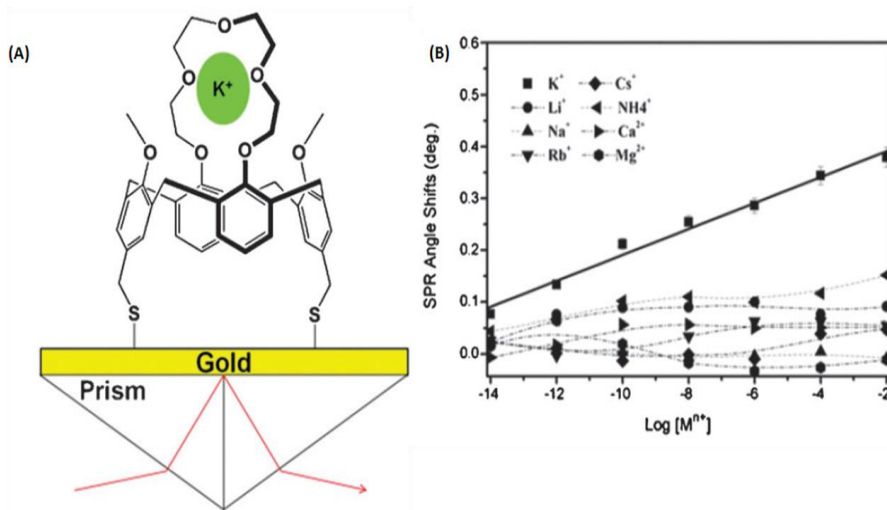


**Figure 2-3.** (A) A sensor chip configuration. (B) SPR angle shifts with respect to various concentrations of several metal ions. Solid line is the linear fit ( $r^2 = 0.9928$ ). Other lines were used to guide eyes. [Adapted with permission from Reference 11].

Dabestani and coworkers<sup>12</sup> reported using calix[4]-benzocrown-6 as an example of an ion-selective SAM-modified microcantilever receptor. Cesium ions in the concentration range of  $10^{-12}$ – $10^{-7}$  M could be detected by the sensor. This finding showed

the potential for developing a new family of real-time *in situ* metal ion sensors for chemical and biological applications that would have the potential benefits of low cost and high sensitivity/selectivity. When the concentration of cesium ions are in the range of  $10^{-7}$ – $10^{-11}$  M, Figure 2-4 shows the most impressive microcantilever deflection response reported.<sup>12</sup> In contrast, there is only a small response to potassium ions at the same concentration range. These authors further demonstrated that it is possible to apply the concept of an ion-selective SAM-coated cantilever to sense with remarkable sensitivity, trace amounts (ppb) of cesium ions (*in situ*) when high concentrations of  $K^+$  and  $Na^+$  ions are present.

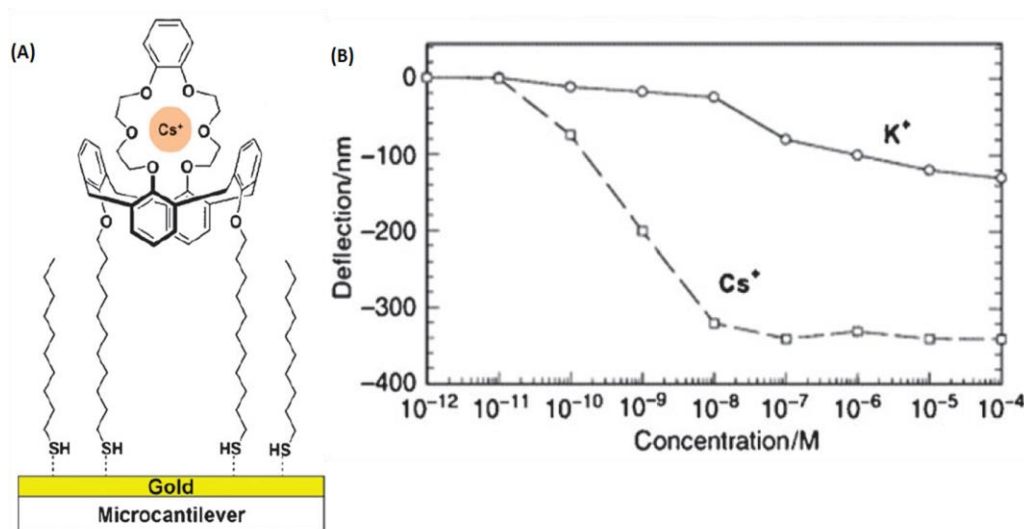


**Figure 2-4.** (A) Molecular structure of calix[4]benzocrown-6 co-absorbed with decane-1-thiol on the gold surface of a microcantilever via the SAM technique. (B) Bending deflection response of the SAM-coated microcantilever as a function of the change in the concentration of  $Cs^+$  and  $K^+$  ions. [Adapted with permission from Reference 12]

### 2.1.3 Anion sensors

Echegoyen and coworkers<sup>13</sup> synthesized and characterized the anion receptor based on the calix[6]crown-4 architecture shown in Figure 2-5. In their study, they obtained insights into the binding mode of the receptor with fluoride ions by <sup>1</sup>H NMR spectroscopy. The results of their study demonstrated that the receptor evidenced the highest binding affinity for fluoride ions over other anions, including Cl<sup>-</sup>, NO<sub>3</sub><sup>-</sup>, H<sub>2</sub>PO<sub>4</sub><sup>-</sup>, HSO<sub>4</sub><sup>-</sup>, Br<sup>-</sup>, and AcO<sup>-</sup>.

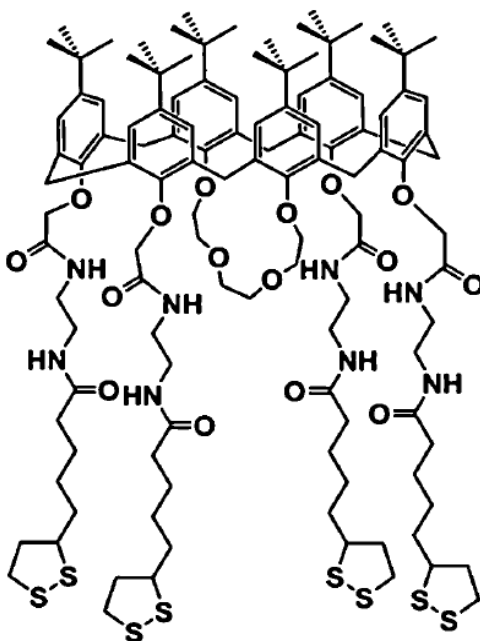


**Figure 2-5.** Molecular structure of calix[6]-crown. [Adapted with permission from Reference 13]

### 2.1.4 Thioacetate-bearing calix[4]arene

Georghiou *et al.*<sup>14</sup> reported the synthesis and application of a thioacetate-bearing calix[4]arene, **5** (Scheme 2.1) which, in the solid state, was found to be in a *pinched-cone* conformation.<sup>15</sup> This new calixarene was capable of forming a SAM on gold (Figure 2-6),

which could be confirmed using both Scanning Tunneling Microscopy (STM) and Scanning Electron Microscopy (SEM). This finding established that the conversion of the thioacetate to a thiol which was initially presumed to be a necessary prerequisite for binding to gold was not needed, thereby saving several difficult additional synthetic steps. Calcium ions using aqueous  $\text{CaCl}_2$  solution with concentrations as low as  $10^{-11}$  M could be detected by the calixarene-SAM on a gold microcantilever. By employing the mathematical treatment used by Dabestani and coworkers a comparable complexation constant value could be determined.<sup>14</sup>

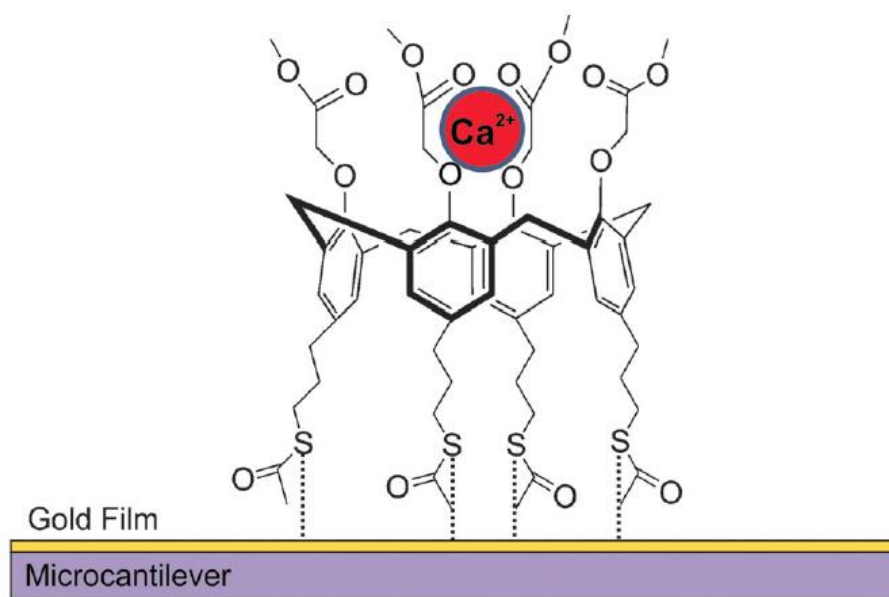
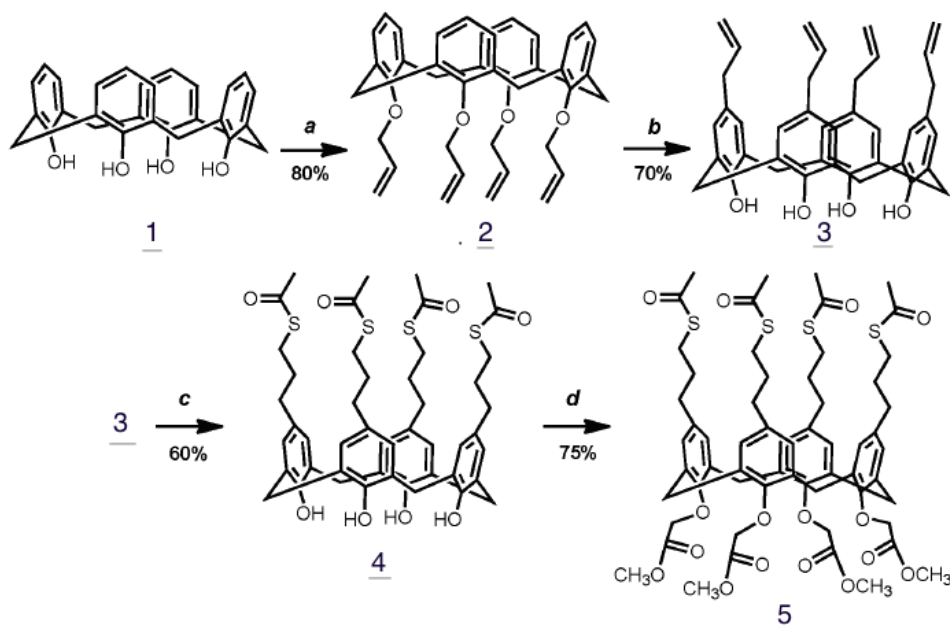


**Figure 2-6.** Structure of **5** showing the “anchoring” of the “upper rim” thioacetate grouping onto the gold surface of a gold microcantilever. [Adapted with permission from Reference 14]

### 2.1.4.1 Synthesis of upper- and lower-rim functionalized calix[4]arene

Scheme 2.1 outlines the process by which **5** was synthesized (by G. Valluru and S. Rahman at Memorial University). The de-*tert*-butylated calix[4]arene **1**<sup>16</sup> was used as the starting material in the synthetic process. A Claisen rearrangement<sup>17</sup> resulted in the formation of **3** via the tetra-*O*-allyl calixarene **2**.<sup>18</sup> The next step in the synthesis is the thioacetylation<sup>19</sup> of the terminal alkene with thioacetic acid in dioxane, which results in formation of **4**. Finally, **4** was converted to the desired product, tetrakis-[*O*-(methoxycarbonyl)methoxy]calix[4]-arene **5**.



**Scheme 2.1.** Synthesis of upper- and lower-rim functionalized calix[4]arene **5**.

*Conditions:* (a) CH<sub>2</sub>=CHCH<sub>2</sub>Br, NaH/THF, reflux, 24 h; (b) *N,N*-dimethylaniline, 210°C, 24 h; (c) CH<sub>3</sub>COSH/AIBN, dioxane, reflux, 24 h; (d) BrCH<sub>2</sub>CO<sub>2</sub>CH<sub>3</sub>, NaH/THF, reflux, 48 h. [Adapted with permission from reference 14].

### 2.1.4.2 Microcantilever results

The deflection of the functionalized cantilevers reported by Georghiou *et al*<sup>14</sup> as a function of different concentrations of various calcium salts e.g. CaCl<sub>2</sub> is shown in Figure 2-7. It can be seen that higher concentrations of CaCl<sub>2</sub> solutions result in larger deflections. The reference cantilever is not surface-coated with **5** but only with 1-decanethiol as shown in the red curve. The reference cantilever had no deflection when it was exposed to the CaCl<sub>2</sub> solution because it does not have binding sites for Ca<sup>2+</sup> or Cl<sup>-</sup> ions. Ca<sup>2+</sup> cation concentrations as low as 10<sup>-11</sup> M may easily detect by calix[4]arene **5**-coated micro cantilever sensors, as seen from the Figure 2-7.

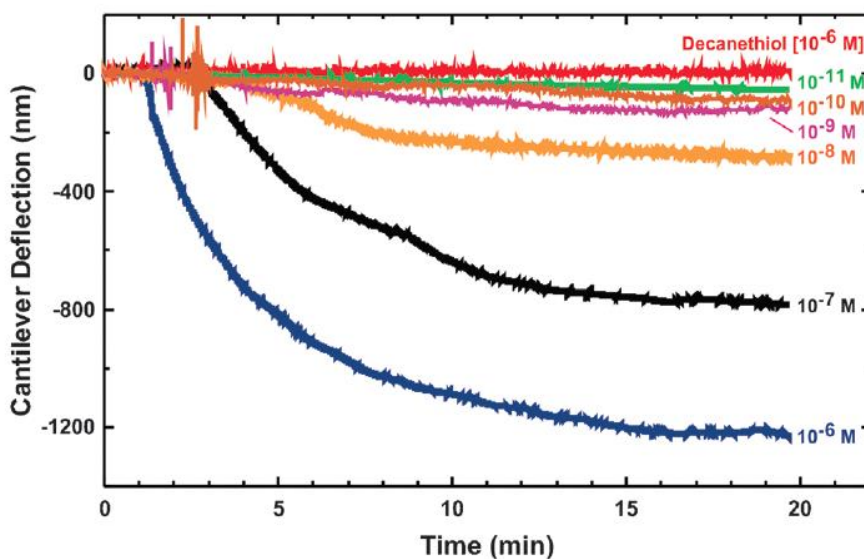


**Figure 2-7.** Responses to different concentrations of CaCl<sub>2</sub> for microcantilevers functionalized with calix[4]arene **5** and a reference microcantilever functionalized with 1-decanethiol. [Adapted with permission from reference 14]

## 2.2. Objectives of the work reported in this Chapter

As part of the on-going studies on the development of a microcantilever-based real time device employing modified calixarene-derived sensing layers in a collaborative project with the Dr. Beaulieu group in the Department of Physics at Memorial University, a study was undertaken to determine solution-phase complexation properties of **5** and its ethoxy analogue **6**. Initially it was envisioned that a parallel study could be undertaken with similar aqueous solution concentrations of the salts with **5** and **6** and using fluorescence spectroscopy. However this proved to be unfeasible since the host molecules were neither water-soluble nor Uv-active. Instead, experiments were designed using <sup>1</sup>H-NMR spectroscopic titrations in a CD<sub>3</sub>OD:CDCl<sub>3</sub> solvent mixture since this solvent system enabled both **5** and **6** (Figure 2-8) calcium salts to be dissolved in the minimum concentrations required to conduct the titration studies.

## 2.3 Complexation studies

Stock solutions ( $\sim 1.50 \times 10^{-3}$  M) of **5** and **6** were prepared in a 4:1 CD<sub>3</sub>OD:CDCl<sub>3</sub> solvent mixture. From concentrated ( $\sim 2.00 \times 10^{-1}$  M) stock solutions of the respective metal salts e.g. CaCl<sub>2</sub>; CaBr<sub>2</sub>; CaI<sub>2</sub>; Ca(ClO<sub>4</sub>)<sub>2</sub>; Ca(NO<sub>3</sub>)<sub>2</sub>; Ca(TFA)<sub>2</sub>; LiI; NaI; KI, and AgTFA, small aliquots ( $\sim 5.0$   $\mu$ L) of the metal salt solutions were added to 0.60 mL of the respective calix solution in a NMR tube. After shaking for 5 min, following each addition, the resulting <sup>1</sup>H NMR spectra were recorded at 24 $\pm$ 1 $^{\circ}$ C. Each titration experiment was conducted in duplicate. From the resulting chemical shift changes measured, the

association constants ( $K_{\text{assoc}}$ ) were calculated using a 1:1 non-linear binding curve fitting program with Origin Program6.<sup>20</sup>

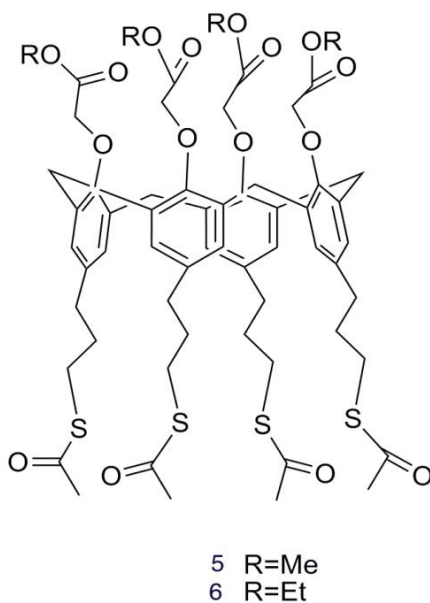


**Figure 2-8.** Structures of Calix **5** and **6**.

### **2.3.1 Complexation of methyl ester calixarene **5** and its corresponding ethyl ester **6** with various calcium salts**

#### **2.3.1.1 Ethyl ester **6** with $\text{CaCl}_2$**

Figure 2-9 shows the  $^1\text{H-NMR}$  titration spectra of **6** with successive additions of aliquots of a  $\text{CaCl}_2$  solution. It can be seen that by increasing the amounts of  $\text{CaCl}_2$  to the solution of **6**, downfield changes result in the chemical shifts of the calixarene aromatic (*Ar-H*) singlet and  $-\text{COOCH}_2\text{CH}_3$  triplet signals. Upfield changes in the chemical shifts however can also be seen for the  $\text{SCOCH}_3$  proton singlet from  $\delta$  2.325 to 2.177 ppm. The *Ar-H* and  $\text{COOCH}_2\text{CH}_3$  proton chemical shifts moved downfield from  $\delta$  6.523 to 7.059

ppm, and from  $\delta$  1.310 to 1.411 ppm respectively (Table 2-1), confirming that complexation occurred between **6** and  $\text{CaCl}_2$ .

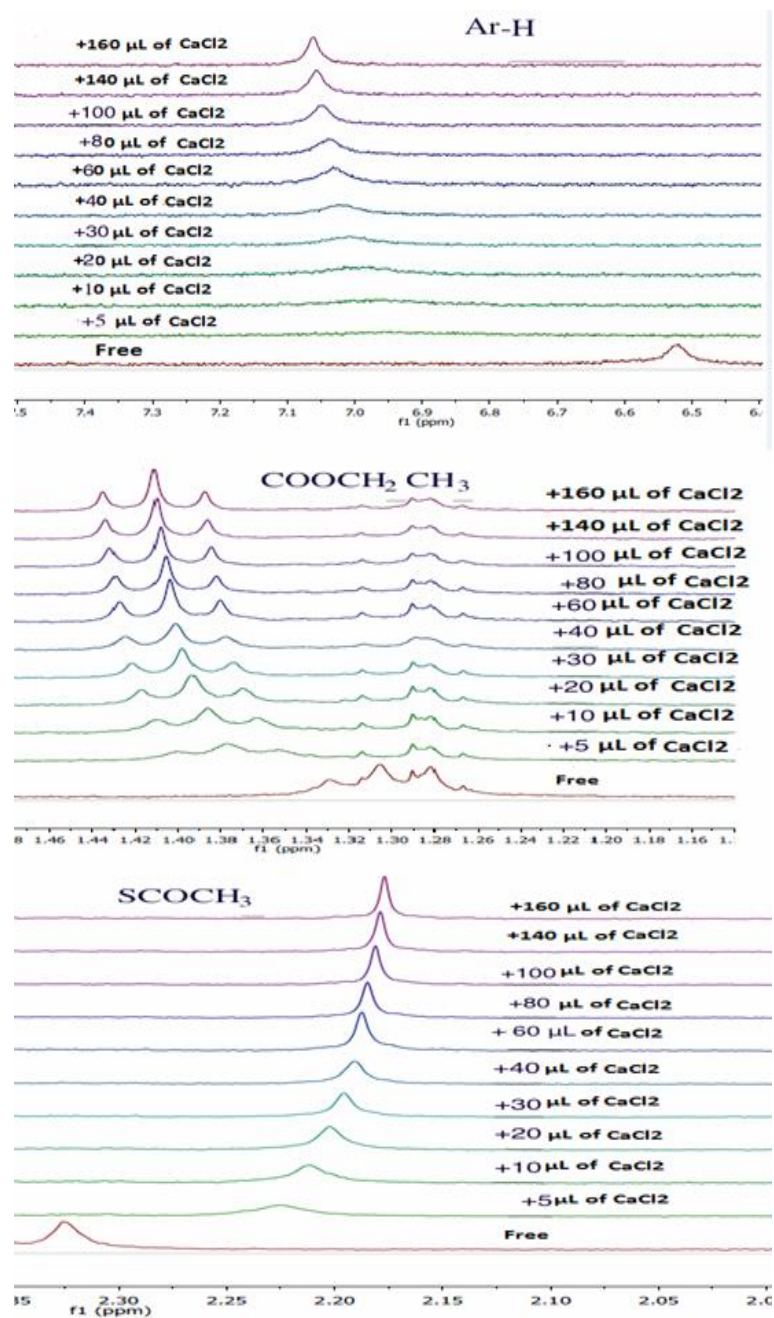


**Figure 2-9.**  $^1\text{H}$  NMR (300 MHz) titration spectra for Ar-H (Top) and  $-\text{COOCH}_2\text{CH}_3$  (Middle), and  $\text{SCOCH}_3$  (Bottom) of **6** with  $\text{CaCl}_2$ .

The extent of this complexation was determined by measuring the binding, or association constant ( $K_{assoc}$ ), using a non-linear 1:1 binding isotherm for the Ar-H, COOCH<sub>2</sub>CH<sub>3</sub>, and SCOCH<sub>3</sub> chemical shift changes as a function of the concentration of the added CaCl<sub>2</sub> (Table 2-1).

**Table 2-1.** <sup>1</sup>H NMR (300 MHz) titration chemical shift data for Ar-H, COOCH<sub>2</sub>CH<sub>3</sub>, and SCOCH<sub>3</sub> of **6** (1.50×10<sup>-3</sup> M) upon the addition of CaCl<sub>2</sub>.

[CaCl <sub>2</sub> ]	G/H	Ar-H δ(ppm)	Δδ(Hz)	-OOCH <sub>2</sub> CH <sub>3</sub> δ(ppm)	Δδ (Hz)	-SCOCH <sub>3</sub> Δ(ppm)	Δδ(Hz)
0		<b>6.523</b>		<b>1.310</b>		<b>2.325</b>	
1.19E-02	2.80	6.940	125.4	1.377	20.1	2.225	30.0
1.47E-02	5.59	6.958	130.5	1.386	22.8	2.212	33.9
1.75E-02	11.18	6.984	138.3	1.393	24.9	2.202	36.9
2.02E-02	22.36	7.005	144.6	1.398	26.4	2.196	38.7
2.28E-02	33.55	7.018	148.5	1.401	27.3	2.191	40.2
2.54E-02	44.73	7.028	151.5	1.404	28.2	2.187	41.4
2.80E-02	55.91	7.037	154.2	1.406	28.8	2.185	42.0
3.29E-02	67.09	7.047	157.2	1.408	29.4	2.181	43.2
3.76E-02	78.27	7.055	159.6	1.410	30.0	2.179	43.8
4.22E-02	89.46	7.059	160.8	1.411	30.3	2.177	44.4

Using the Origin program developed in the Georghiou lab for 1:1 binding, the association constants values were determined to be 176±5, 111±10 and 104±14 M<sup>-1</sup> respectively, based on the aromatic (Ar-H), -SCOCH<sub>3</sub> and -COOCH<sub>2</sub>CH<sub>3</sub> protons chemical shift changes (Figure 2-10).

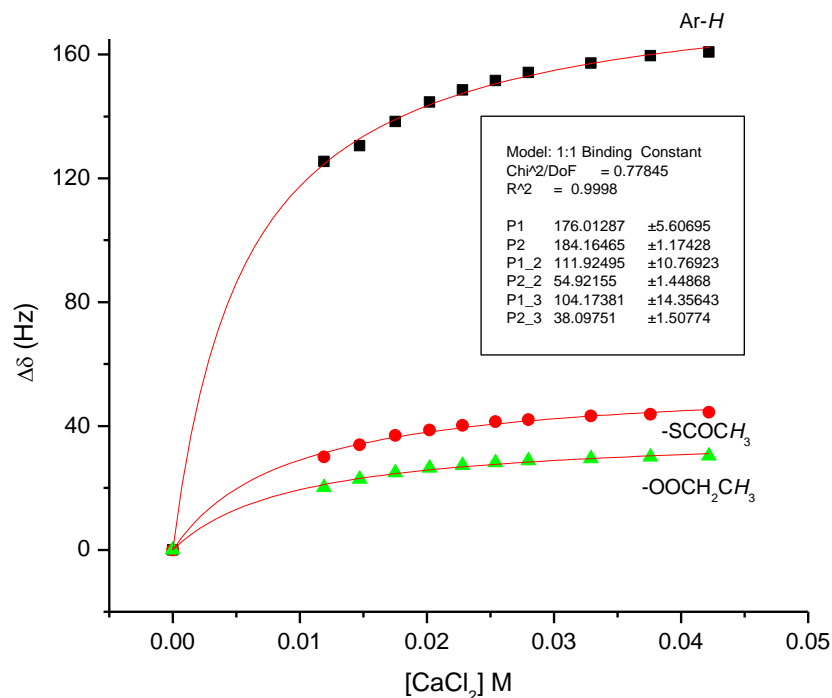


**Figure 2-10.**  $^1\text{H}$  NMR (300 MHz) titration curves for Ar-H,  $\text{COOCH}_2\text{CH}_3$ , and  $-\text{SCOCH}_3$  respectively, of **6** ( $1.50 \times 10^{-3}$  M) with  $\text{CaCl}_2$ .

### 2.3.1.2 Methyl ester **5** with $\text{CaCl}_2$

Figure 2-11 shows the  $^1\text{H}$ -NMR titration spectra of **5** with successive additions of aliquots of a  $\text{CaCl}_2$  solution. It can be seen that by increasing the amounts of  $\text{CaCl}_2$  to the solution of **5**, downfield chemical shift change occurs for the singlet signals due to the  $-\text{COOCH}_3$  protons. However, the  $-\text{OCH}_2\text{COOCH}_3$  proton singlet signals are shifted upfield. The  $\text{COOCH}_3$  signals shifted downfield from  $\delta$  3.776 to 3.927 ppm, whereas the  $\text{OCH}_2\text{COOCH}_3$  proton singlet shifted upfield from  $\delta$  4.730 to 4.578 ppm (Table 2-2), indicating that complexation occurred between **5** and  $\text{CaCl}_2$ .

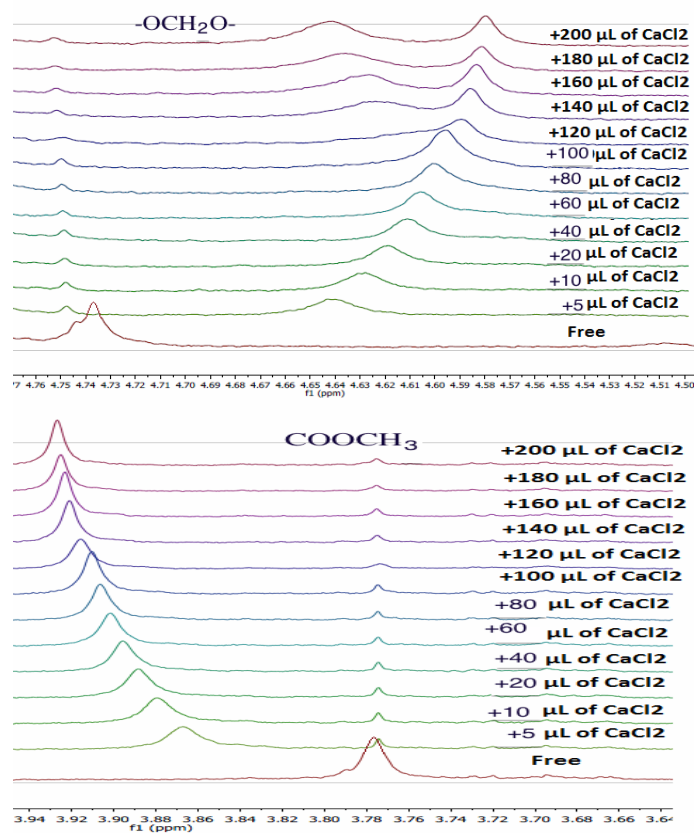


**Figure 2-11.** <sup>1</sup>H NMR (300 MHz) titration spectra for -OCH<sub>2</sub>COOCH<sub>3</sub> (Top) and COOCH<sub>3</sub> (Bottom) of **5** with CaCl<sub>2</sub>.

**Table 2-2.** <sup>1</sup>H NMR (300 MHz) titration chemical shift data for -OCH<sub>2</sub>COOCH<sub>3</sub>, and COOCH<sub>3</sub> of **5** (1.50×10<sup>-3</sup> M) with CaCl<sub>2</sub>.

[Guest]	G/H	COOCH <sub>3</sub> δ(ppm)	Δδ(Hz)	- OCH <sub>2</sub> COOCH <sub>3</sub> δ(ppm)	Δδ(Hz)
		<b>3.776</b>		<b>4.737</b>	
1.54E-03	2.80	3.867	27.3	4.639	29.4
3.07E-03	5.59	3.879	30.9	4.627	33.0
6.08E-03	11.18	3.888	33.6	4.617	36.0
1.19E-02	22.36	3.895	35.7	4.609	38.4
1.75E-02	33.55	3.902	37.8	4.603	40.2
2.28E-02	44.73	3.906	39.0	4.597	42.0
2.80E-02	55.91	3.910	40.2	4.594	42.9
3.29E-02	67.09	3.916	42.0	4.588	44.7
3.76E-02	78.27	3.921	43.5	4.584	45.9
4.22E-02	89.46	3.923	44.1	4.582	46.5
4.66E-02	98.27	3.925	44.7	4.580	47.1
5.08E-02	110.46	3.927	45.3	4.578	47.7

Figure 2-12 shows the  $^1\text{H}$ -NMR titration spectra of **5** with successive additions of aliquots of a  $\text{CaCl}_2$  solution. It can be seen that by increasing the amounts of  $\text{CaCl}_2$  to the solution of **5**, downfield changes result in the chemical shifts of the calixarene aromatic (*Ar-H*) singlet signals (*Ar-H*) from 6.523 ppm to 7.064 ppm, whereas the upfield change in chemical shift occurs for  $\text{SCOCH}_3$  proton from 2.326 ppm to 2.176 ppm.

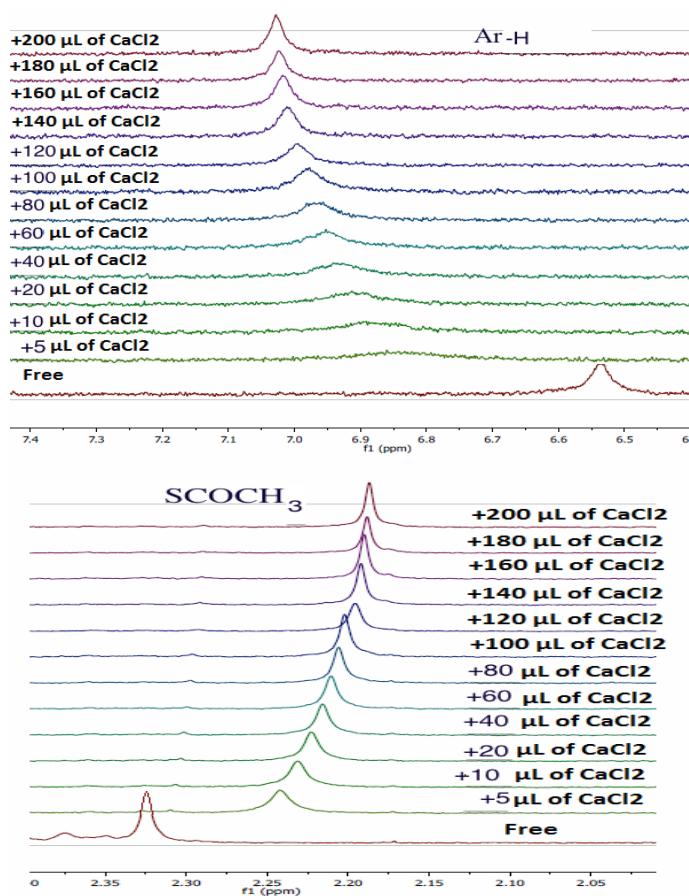


**Figure 2-12.**  $^1\text{H}$  NMR (300 MHz) titration spectra for *Ar-H* (*Top*) and  $\text{SCOCH}_3$  (*Bottom*) of **5** with  $\text{CaCl}_2$ .

**Table 2-3.**  $^1\text{H}$  NMR (300 MHz) titration chemical shift data for Ar-*H*, and  $\text{SCOCH}_3$  of **5** with  $\text{CaCl}_2$ .

[ $\text{CaCl}_2$ ]	G/H	Ar- <i>H</i> $\delta$ (ppm)	$\Delta\delta$ (Hz)	$\text{SCOCH}_3$ $\delta$ (ppm)	$\Delta\delta$ (Hz)
		<b>6.84</b>		<b>2.324</b>	
1.54E-03	2.80	6.878	90.6	2.242	24.6
3.07E-03	5.59	6.908	102.6	2.231	27.9
6.08E-03	11.18	6.927	111.6	2.223	30.3
1.19E-02	22.36	6.951	117.3	2.216	32.4
1.75E-02	33.55	6.963	124.5	2.21	34.2
2.28E-02	44.73	6.976	128.1	2.206	35.4
2.80E-02	55.91	6.993	132.0	2.202	36.6
3.29E-02	67.09	7.009	137.1	2.196	38.4
3.76E-02	78.27	7.016	141.9	2.192	39.6
4.22E-02	89.46	7.022	144.1	2.19	40.2
4.66E-02	98.27	7.026	145.8	2.188	40.8

The association constants ( $K_{assoc}$ ), were determined using the non-linear 1:1 binding isotherms for the aromatic singlet signals (Ar-*H*),  $-\text{OCH}_2\text{COOCH}_3$ ,  $-\text{COOCH}_3$  and  $\text{SCOCH}_3$  (Tables 2-2, 2-3). Using the Origin program the molar concentrations of the guest [Guest] were plotted against the observed chemical shift changes ( $\Delta\delta$ ) in Hz. The resulting  $K_{assoc}$  values were determined to be  $78\pm 2$ ,  $72\pm 5$ ,  $77\pm 5$  and  $69\pm 5$   $\text{M}^{-1}$  respectively, based on the aromatic singlet signals (Ar-*H*),  $-\text{OCH}_2\text{COOCH}_3$ ,  $\text{COOCH}_3$  and  $-\text{SCOCH}_3$  proton chemical shift changes (Figure 2-13).

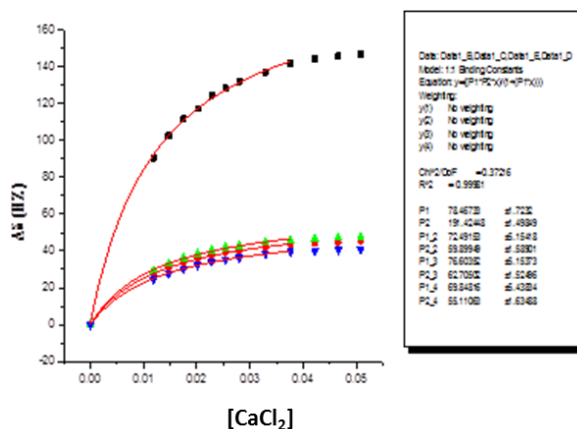


**Figure 2-13.**  $^1\text{H}$  NMR (300 MHz) titration curves for Ar-*H*,  $-\text{OCH}_2\text{COOCH}_3$ ,  $-\text{COOCH}_3$ , and  $-\text{SCOCH}_3$  respectively of **5** ( $1.50 \times 10^{-3}$  M) with  $\text{CaCl}_2$ .

### 2.3.1.3 Methyl ester **5** with $\text{CaBr}_2$

Figure 2-14 shows the  $^1\text{H}$ -NMR titration spectra of **5** with successive additions of aliquots of a  $\text{CaBr}_2$  solution. It can be seen that by increasing the amounts of  $\text{CaBr}_2$  to the solution of **5**, downfield changes result in the chemical shifts of the calixarene aromatic (Ar-*H*) singlet,  $-\text{SCOCH}_3$  and  $-\text{COOCH}_3$  triplet signals. (Table 2-4) indicating complexation between **5** and  $\text{CaBr}_2$ .

**Table 2-4.**  $^1\text{H}$  NMR (300 MHz) titration chemical shift data for Ar-*H*,  $-\text{COOCH}_3$ , and  $\text{SCOCH}_3$  of **5** ( $1.50 \times 10^{-3}$  M) with  $\text{CaBr}_2$ .

[ $\text{CaBr}_2$ ]	G/H	Ar- <i>H</i> $\delta$ (ppm)	$\Delta\delta$ (Hz)	$\text{COOCH}_3$ $\delta$ (ppm)	$\Delta\delta$ (Hz)	$\text{SCOCH}_3$ $\delta$ (ppm)	$\Delta\delta$ (Hz)
		<b>6.525</b>		<b>3.783</b>		<b>2.338</b>	
1.08E-02	2.80	6.534	2.7	3.785	0.6	2.328	3.0
3.19E-02	8.40	6.540	4.5	3.785	0.6	2.327	3.3
5.23E-02	16.80	6.542	5.1	3.786	0.9	2.326	3.6
8.17E-02	28.36	6.544	5.7	3.786	0.9	2.326	3.6
1.19E-01	39.55	6.545	6.0	3.787	1.2	2.326	3.6
1.70E-01	50.73	6.545	6.0	3.788	1.5	2.326	3.6

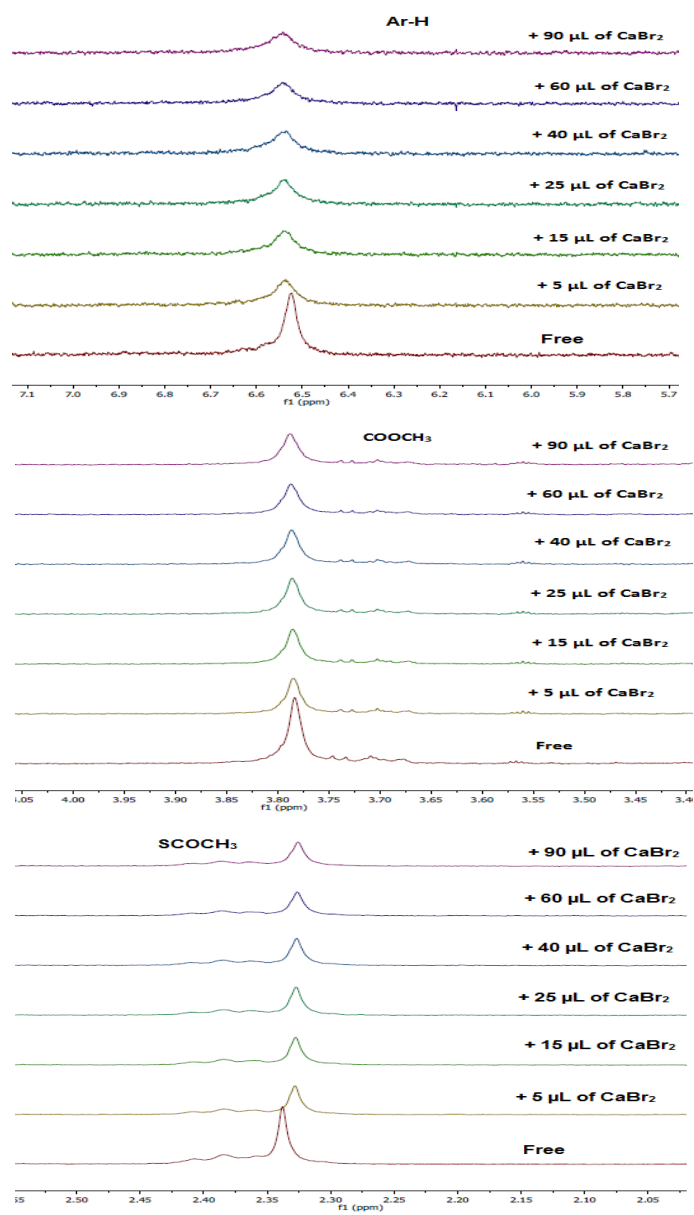


**Figure 2-14.** <sup>1</sup>H NMR (300 MHz) titration spectra for Ar-H (*Top*) and -COOCH<sub>3</sub> (*Middle*), and -SCOCH<sub>3</sub> (*Bottom*) of **5** with CaBr<sub>2</sub>.

### 2.3.1.4 Ethyl ester **6** with CaI<sub>2</sub>

Figure 2-15 shows the <sup>1</sup>H-NMR titration spectra of **6** with successive additions of aliquots of a CaI<sub>2</sub> solution. It can be seen that by increasing the amounts of CaI<sub>2</sub> to the solution of **6**, downfield changes result in the chemical shifts of -COOCH<sub>2</sub>CH<sub>3</sub> triplet signals from δ 3.783 to 3.788 ppm, and calixarene aromatic (Ar-H) singlet from δ 6.525 to 6.545 ppm. However, upfield changes in the chemical shift occurs for the -SCOCH<sub>3</sub> proton from δ 2.338 to 2.326 ppm (Table 2-5) indicating again, complexation between **6** and CaI<sub>2</sub>.

**Table 2-5.** <sup>1</sup>H NMR (300 MHz) titration chemical shift data for Ar-H, -COOCH<sub>2</sub>CH<sub>3</sub>, and SCOCH<sub>3</sub> of **6** (1.50×10<sup>-3</sup> M) with CaI<sub>2</sub>.

[CaI <sub>2</sub> ]	G/H	Ar-H δ(ppm)	Δδ(Hz)	-COOCH <sub>2</sub> CH <sub>3</sub> δ(ppm)	Δδ (Hz)	SCOCH <sub>3</sub> δ(ppm)	Δδ (Hz)
		<b>6.525</b>		<b>1.306</b>		<b>2.323</b>	
2.16E-03	1.74	6.534	2.7	1.396	27.0	2.199	37.2
6.38E-03	5.15	6.540	4.5	1.406	30.0	2.184	41.7
1.24E-02	10.05	6.542	5.1	1.416	33.0	2.171	45.6
2.01E-02	17.40	6.544	5.7	1.420	34.2	2.166	47.1
2.73E-02	24.36	6.545	6.0	1.423	35.1	2.164	47.7

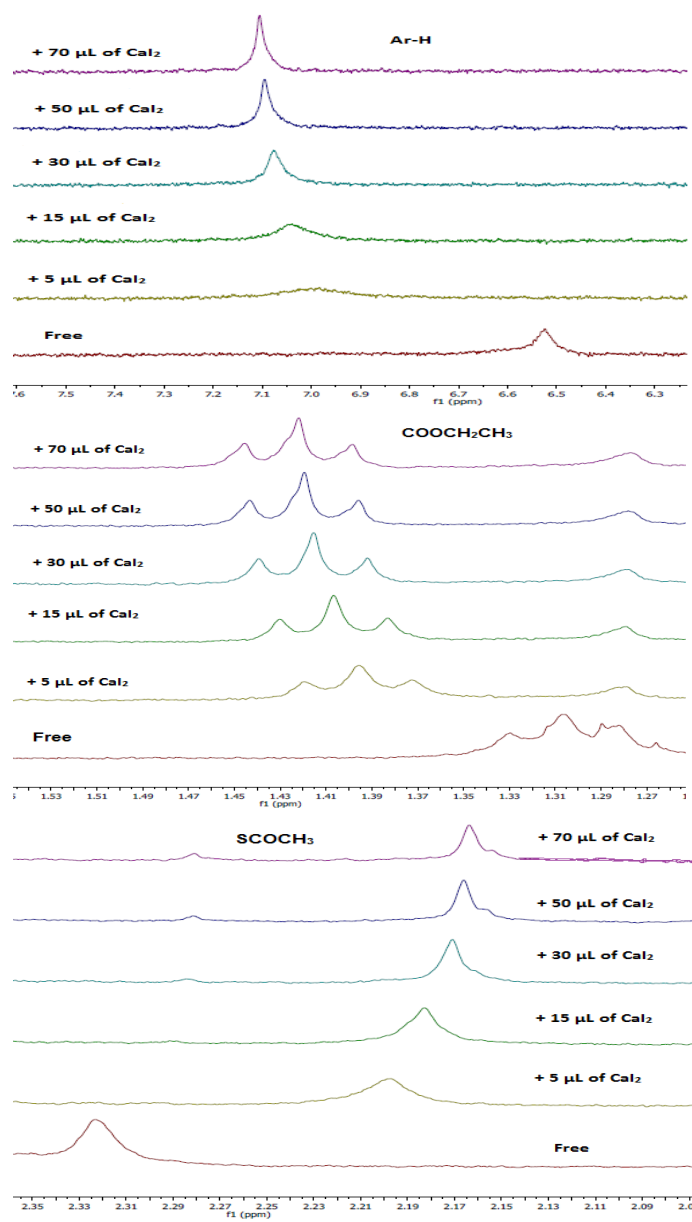


**Figure 2-15.**  $^1\text{H}$  NMR (300 MHz) titration spectra for *Ar-H* (Top),  $-\text{COOCH}_2\text{CH}_3$  (Middle), and  $-\text{SCOCH}_3$  (Bottom) of **6** with  $\text{CaI}_2$ .

The extent of this complexation was determined as before by the respective  $K_{\text{assoc}}$  values, and were determined to be,  $20 \pm 1$ ,  $16 \pm 2$  and  $15 \pm 2 \text{ M}^{-1}$  respectively, based on the aromatic singlet signals (*Ar-H*),  $-\text{COOCH}_2\text{CH}_3$  and  $-\text{SCOCH}_3$  proton chemical shift changes (Figure 2-16).

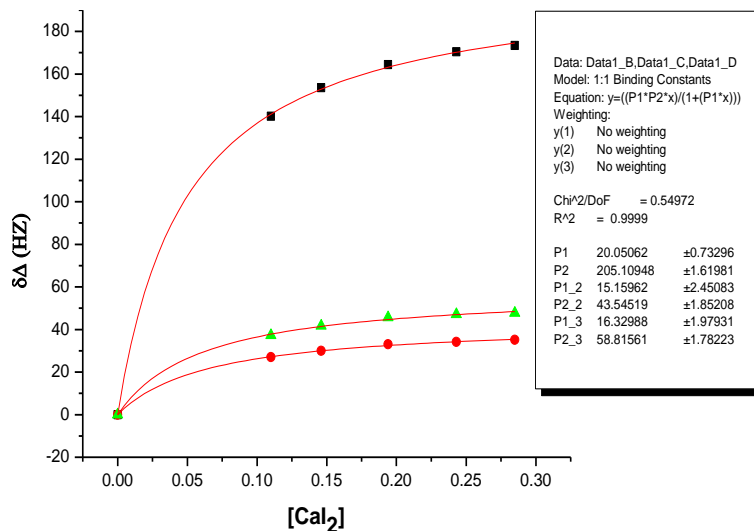


**Figure 2-16.**  $^1\text{H}$  NMR (300 MHz) titration curves for Ar-*H*,  $\text{COOCH}_2\text{CH}_3$ , and  $\text{SCOCH}_3$  respectively of **6** ( $1.50 \times 10^{-3}$  M) with  $\text{CaI}_2$ .

### 2.3.1.5 Methyl ester **5** with $\text{CaI}_2$

Figure 2-17 shows the  $^1\text{H}$ -NMR titration spectra of **5** with successive additions of aliquots of a  $\text{CaI}_2$  solution. It can be seen that by increasing the amounts of  $\text{CaI}_2$  to the solution of **5**, downfield chemical shift changes for both the singlet Ar-*H* and  $-\text{COOCH}_3$  proton singlet signals from  $\delta$  6.542 to 7.042 ppm and  $\delta$  3.770 to 3.925 ppm, respectively.

Table 2-6 indicates complexation between **5** and  $\text{CaI}_2$ .

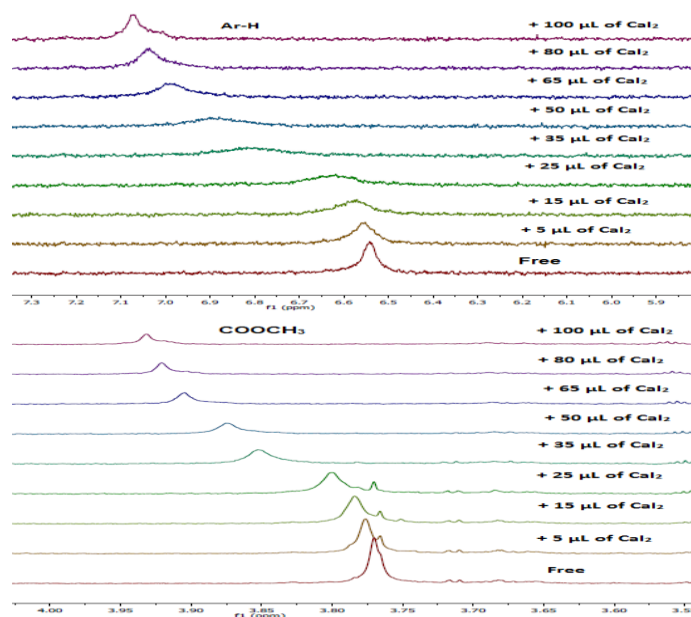


**Figure 2-17.**  $^1\text{H}$  NMR (300 MHz) titration spectra for Ar-H (Top) and  $-\text{COOCH}_3$  (Bottom) of **5** with  $\text{CaI}_2$ .

**Table 2-6.**  $^1\text{H}$  NMR (300 MHz) titration chemical shift data for Ar-H,  $-\text{COOCH}_3$  of **5** ( $1.50 \times 10^{-3}$  M) with  $\text{CaI}_2$ .

[ $\text{CaI}_2$ ]	G/H	Ar-H $\delta$ (ppm)	$\Delta\delta$ (Hz)	$-\text{COOCH}_3$ $\delta$ (ppm)	$\Delta\delta$ (Hz)
		<b>6.542</b>		<b>3.770</b>	
2.16E-03	1.74	6.556	4.2	3.776	1.8
6.38E-03	5.15	6.577	10.5	3.784	4.2
1.05E-02	8.70	6.625	24.9	3.800	9.0
1.44E-02	12.18	6.807	79.5	3.851	24.3
2.01E-02	17.23	6.884	102.6	3.874	31.2
2.55E-02	22.62	6.983	132.3	3.905	40.5
3.08E-02	27.84	7.035	147.9	3.920	45.0
3.73E-02	34.84	7.042	158	3.925	48.0

Figure 2-18 shows the  $^1\text{H}$ -NMR titration spectra of **5** with successive additions of aliquots of a  $\text{CaI}_2$  solution. It can be seen that by increasing the amounts of  $\text{CaI}_2$  to the solution of **5**, downfield chemical shift changes for  $-\text{OCH}_2\text{COOCH}_3$ , and  $-\text{SCOCH}_3$  proton singlet signals from  $\delta$  4.732 to 4.593 ppm and  $\delta$  2.315 to 2.163 ppm, respectively.

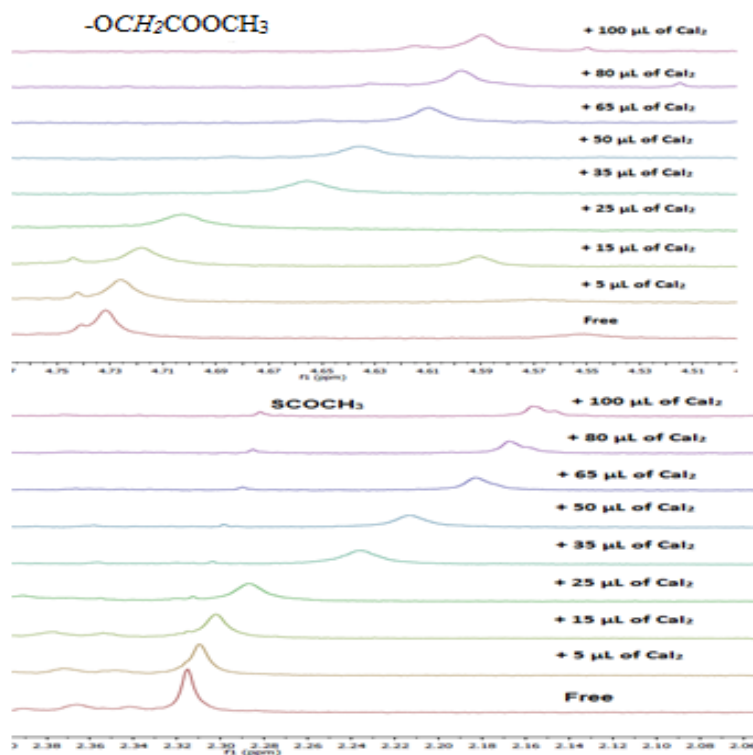


**Figure 2-18.**  $^1\text{H}$  NMR (300 MHz) titration spectra for  $-\text{OCH}_2\text{COOCH}_3$  (Top) and  $\text{SCOCH}_3$  (Bottom) of **5** with  $\text{CaI}_2$ .

It can be seen that by increasing the amounts of  $\text{CaI}_2$  to the solution of **5**, upfield chemical shift changes for both the singlet  $-\text{OCH}_2\text{COOCH}_3$  and Ar-*H* and  $-\text{SCOCH}_3$  proton singlet signals from  $\delta$  4.732 to 4.593 ppm and  $\delta$  2.315 to 2.163 ppm, respectively. Table 2-7 indicates complexation between **5** and  $\text{CaI}_2$ . The extent of this complexation were determined to be  $12 \pm 1$ ,  $14 \pm 5$ ,  $18 \pm 5$  and  $13 \pm 4 \text{ M}^{-1}$  respectively, based on the

respective signals for the Ar-H, -COOCH<sub>3</sub>, SCOCH<sub>3</sub> and -OCH<sub>2</sub>COOCH<sub>3</sub> proton chemical shift changes (Figure 2-19).

**Table 2-7.** <sup>1</sup>H NMR (300 MHz) titration chemical shift data for -OCH<sub>2</sub>COOCH<sub>3</sub> and SCOCH<sub>3</sub> of **5** (1.50×10<sup>-3</sup> M) with CaI<sub>2</sub>.

[CaI <sub>2</sub> ]	G/H	-OCH <sub>2</sub> COOCH <sub>3</sub> δ(ppm)	Δδ (Hz)	SCOCH <sub>3</sub> δ(ppm)	Δδ (Hz)
		<b>4.732</b>		<b>2.315</b>	
2.16E-03	1.74	4.726	1.8	2.31	1.5
6.38E-03	5.15	4.718	4.2	2.302	3.9
1.05E-02	8.70	4.703	8.7	2.287	8.4
1.44E-02	12.18	4.656	22.8	2.236	23.7
2.01E-02	17.23	4.635	29.1	2.213	30.6
2.55E-02	22.62	4.610	36.6	2.182	39.9
3.08E-02	27.84	4.597	40.5	2.167	44.4
3.73E-02	34.84	4.593	43.0	2.163	47.0

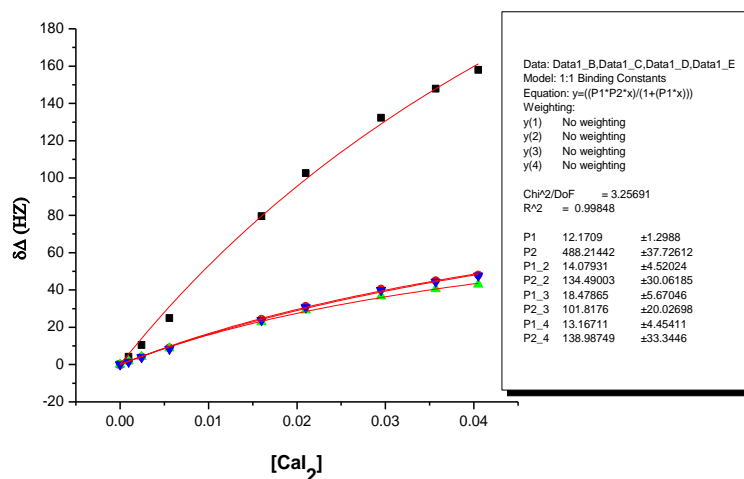


**Figure 2-19.** <sup>1</sup>H NMR (300 MHz) titration curves for Ar-H, -COOCH<sub>3</sub>, -SCOCH<sub>3</sub>, and OCH<sub>2</sub>COOCH<sub>3</sub> respectively of **5** (1.50×10<sup>-3</sup> M) with CaI<sub>2</sub>.

## 2.3.2 Complexation of methyl ester calixarene **5** and its corresponding ethyl ester **6**

with various with group (1) salts

### 2.3.2.1 Ethly ester **6** with NaI

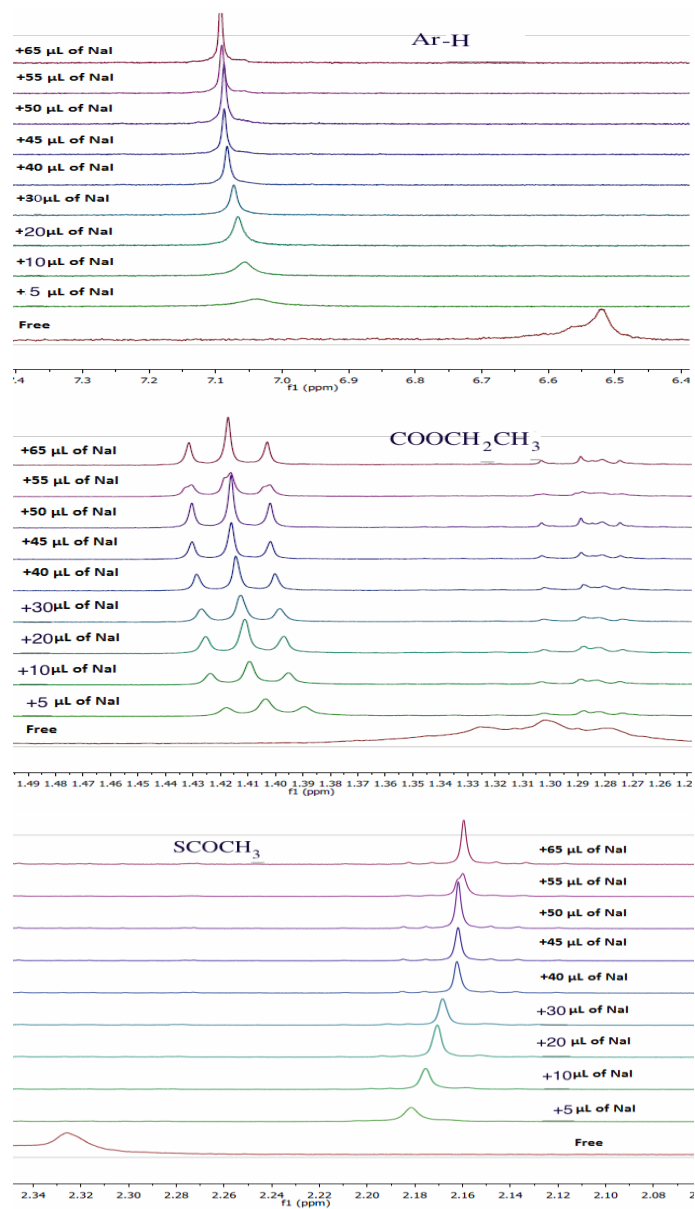


**Figure 2-20.** <sup>1</sup>H NMR (300 MHz) titration spectra for Ar-H (Top) and -COOCH<sub>2</sub>CH<sub>3</sub> (Middle), and -SCOCH<sub>3</sub> (Bottom) of **6** with NaI.

Figure 2-20 shows the  $^1\text{H}$ -NMR titration spectra of **6** with successive additions of aliquots of a NaI solution. It can be seen that by increasing the amounts of NaI to the solution of **6**, downfield chemical shift changes for Ar-*H* and  $-\text{COOCH}_2\text{CH}_3$  proton singlet signals from  $\delta$  6.522 to 7.087 ppm and  $\delta$  1.306 to 1.416 ppm, respectively. On the other hand, upfield chemical shift change occurs for singlet signals due to the  $-\text{SCOCH}_3$  protons from 2.327 ppm to 2.162 ppm. (Table 2-8), indicating that complexation occurred between **6** and NaI. The extent of this complexation was determined as before, by measuring the  $K_{\text{assoc}}$  values using the non-linear 1:1 binding isotherm for all chemical shift changes in **6** (Table 2-8). The resulting  $K_{\text{assoc}}$  values were  $611\pm 35$ ,  $397\pm 97$ , and  $399\pm 57$   $\text{M}^{-1}$  respectively, based on the Ar-*H*,  $-\text{SCOCH}_3$ , and  $-\text{COOCH}_2\text{CH}_3$  proton chemical shift changes (Figure 2-21).

**Table 2-8.**  $^1\text{H}$  NMR (300 MHz) titration chemical shift data for Ar-*H*,  $\text{COOCH}_2\text{CH}_3$ , and  $\text{SCOCH}_3$  of **6** ( $1.5 \times 10^{-3}$  M) with NaI.

[NaI]	G/H	Ar- <i>H</i> $\delta$ (ppm)	$\Delta\delta$ (Hz)	$\text{COOCH}_2\text{CH}_3$ $\delta$ (ppm)	$\Delta\delta$ (Hz)	$-\text{SCOCH}_3$ $\delta$ (ppm)	$\Delta\delta$ (Hz)
		<b>6.522</b>		<b>1.306</b>		<b>2.327</b>	
2.70E-03	1.61	7.038	154.8	1.403	25.8	2.182	43.2
5.36E-03	3.18	7.057	160.5	1.409	27.6	2.175	45.3
1.05E-02	6.26	7.067	163.5	1.411	28.2	2.171	46.5
1.56E-02	9.25	7.073	165.3	1.413	28.8	2.168	47.4
2.04E-02	12.14	7.083	168.3	1.414	29.1	2.162	49.2
2.28E-02	13.55	7.087	169.5	1.416	29.7	2.162	49.2
2.51E-02	16.94	7.087	169.5	1.416	29.7	2.162	49.2
2.74E-02	17.71	7.087	169.5	1.416	29.7	2.162	49.2
3.19E-02	20.93	7.087	169.5	1.416	29.7	2.162	49.2

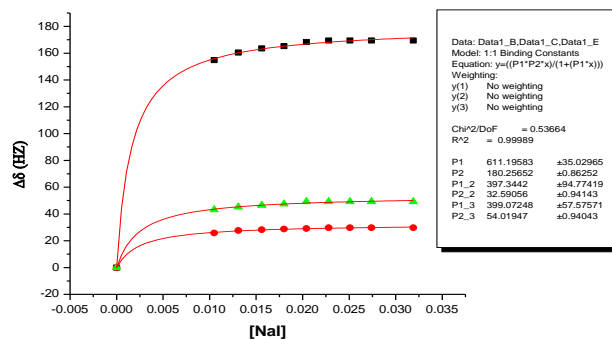


**Figure 2-21.** <sup>1</sup>H NMR (300 MHz) titration curves for Ar-*H*, SCOCH<sub>3</sub>, and COOCH<sub>2</sub>CH<sub>3</sub> respectively of **6** ( $1.50 \times 10^{-3}$  M) with NaI.

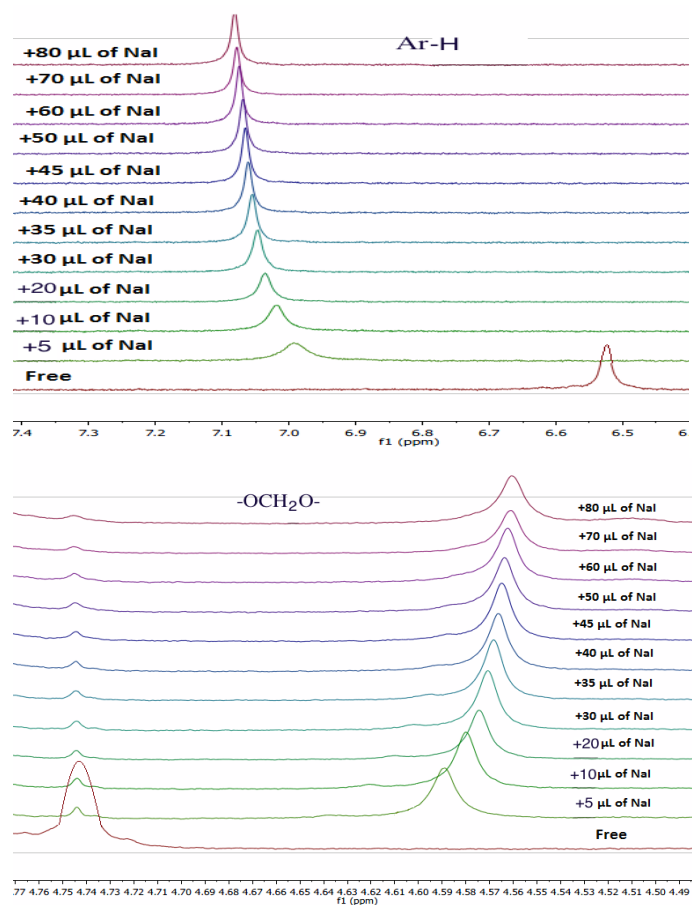
### 2.3.2.2 Methyl ester **5** with NaI

The extent of the complexation between **5** and NaI was determined by measuring the binding, or association constant ( $K_{\text{assoc}}$ ), using the non-linear 1:1 binding isotherm for the aromatic singlet signals (Ar-*H*), -OCH<sub>2</sub>COOCH<sub>3</sub>, -COOCH<sub>3</sub> and -SCOCH<sub>3</sub>, (Table 2-9 and 2-10).

**Table 2-9.** <sup>1</sup>H NMR (300 MHz) titration chemical shift data for Ar-*H*, -OCH<sub>2</sub>COOCH<sub>3</sub>, of **5** ( $1.50 \times 10^{-3}$  M) with NaI.

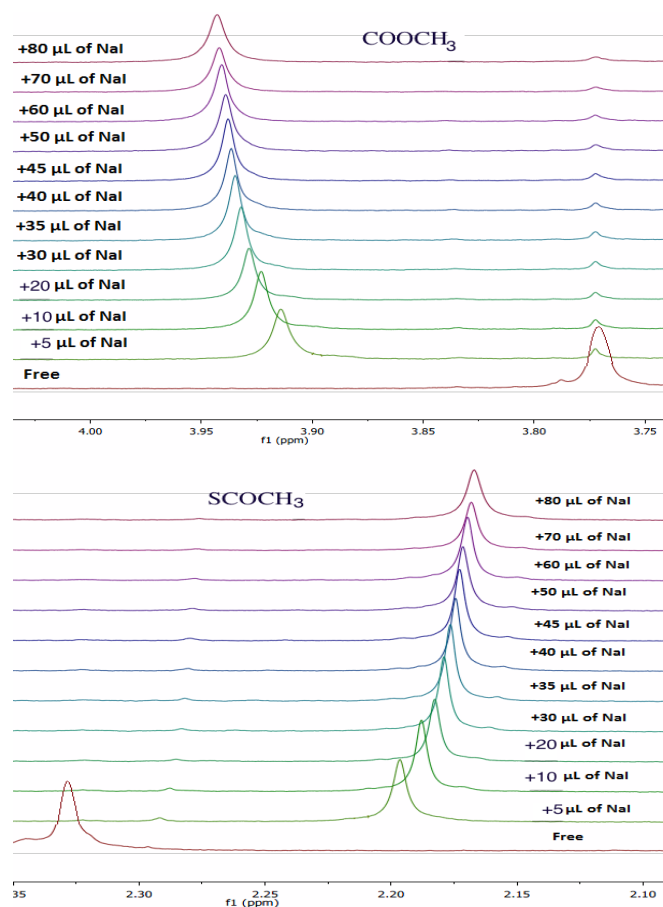
[NaI]	G/H	Ar- <i>H</i> $\delta$ (ppm)	$\Delta\delta$ (Hz)	-OCH <sub>2</sub> COOCH <sub>3</sub> $\delta$ (ppm)	$\Delta\delta$ (Hz)
		6.525		4.742	
2.70E-03	1.82	6.942	125.1	4.606	40.8
5.36E-03	3.64	6.99	139.8	4.589	45.9
1.05E-02	7.28	7.019	148.2	4.580	48.6
1.56E-02	10.47	7.036	153.3	4.575	50.1
1.80E-02	12.12	7.047	156.6	4.571	51.3
2.04E-02	13.74	7.055	159.0	4.569	51.9
2.28E-02	15.34	7.062	161.1	4.566	52.8
2.51E-02	16.91	7.065	162.0	4.565	53.1
2.97E-02	19.98	7.069	163.2	4.564	53.4
3.41E-02	25.97	7.075	165.0	4.563	53.7
3.85E-02	29.86	7.078	165.9	4.561	54.3

Figure 2-22 shows the  $^1\text{H}$ -NMR titration spectra of **5** with successive additions of aliquots of a NaI solution. It can be seen that by increasing the amounts of NaI to the solution of **5**, downfield chemical shift changes for Ar-H and upfield shifted for  $-\text{OCH}_2\text{COOCH}_3$  proton singlet signals from  $\delta$  6.525 to 7.078 ppm and  $\delta$  4.742 to 4.561 ppm, respectively.



**Figure 2-22.**  $^1\text{H}$  NMR (300 MHz) titration spectra for Ar-H (Top) and  $-\text{OCH}_2\text{COOCH}_3$  (Bottom) of **5** with NaI.

The titration spectra of the  $-\text{COOCH}_3$  and  $-\text{SCOCH}_3$  are shown in Figure 2-23. It can be seen that by increasing the amounts of NaI to the solution of **5**, downfield chemical shift changes for  $-\text{COOCH}_3$  and upfield shifted for  $-\text{SCOCH}_3$  proton singlet signals from  $\delta$  3.771 to 3.942 ppm and  $\delta$  2.329 to 2.169 ppm, respectively.



**Figure 2-23.** <sup>1</sup>H NMR (300 MHz) titration spectra for  $-\text{COOCH}_3$  (Top) and  $-\text{SCOCH}_3$  (Bottom) of **5** with NaI.

The 1:1  $K_{assoc}$  values were determined using the non-linear binding isotherms for the chemical shift changes for the Ar-H,  $-\text{OCH}_2\text{COOCH}_3$ ,  $\text{COOCH}_3$  and  $\text{SCOCH}_3$  protons. The molar concentrations of the guest were plotted against the observed

chemical shift changes ( $\Delta\delta$ ) in Hz. The resulting  $K_{assoc}$  values were  $295\pm 11$ ,  $278\pm 33$ ,  $260\pm 32$  and  $296\pm 34$  M<sup>-1</sup> respectively (Figure 2-24).

**Table 2-10.** <sup>1</sup>H NMR (300 MHz) titration chemical shift data for -SCOCH<sub>3</sub>, -COOCH<sub>3</sub>, of **5** ( $1.50\times 10^{-3}$  M) with NaI.

[NaI]	G/H	SCOCH <sub>3</sub> $\delta$ (ppm)	$\Delta\delta$ (Hz)	COOCH <sub>3</sub> $\delta$ (ppm)	$\Delta\delta$ (Hz)
		<b>2.329</b>		<b>3.771</b>	
2.70E-03	1.82	2.212	35.1	3.898	38.1
5.36E-03	3.64	2.196	39.9	3.914	42.9
1.05E-02	7.28	2.188	42.3	3.923	45.6
1.56E-02	10.47	2.183	43.8	3.928	47.1
1.80E-02	12.12	2.179	45.0	3.932	48.3
2.04E-02	13.74	2.177	45.6	3.935	49.2
2.28E-02	15.34	2.174	46.5	3.936	49.5
2.51E-02	16.91	2.173	46.8	3.938	50.1
2.97E-02	19.98	2.171	47.4	3.939	50.4
3.41E-02	25.97	2.17	47.7	3.941	51.0
3.85E-02	29.86	2.169	48.0	3.942	51.3

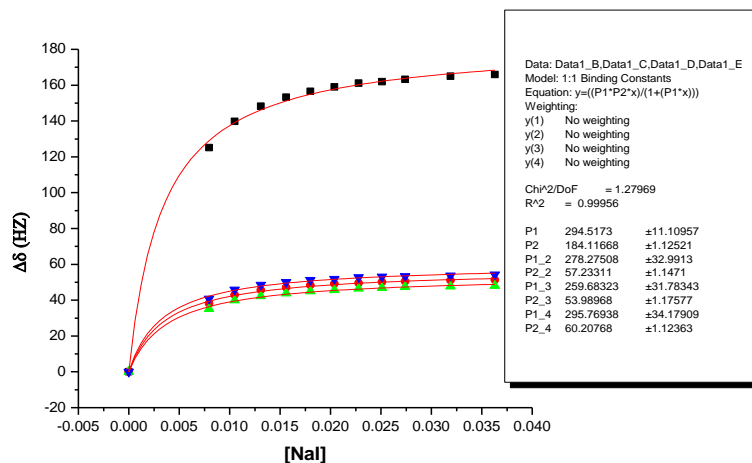


**Figure 2-24.** <sup>1</sup>H NMR (300 MHz) titration curves for Ar-H, -OCH<sub>2</sub>COOCH<sub>3</sub>, -COOCH<sub>3</sub>, and -SCOCH<sub>3</sub>, of **5** ( $1.5\times 10^{-3}$  M) with NaI.

### 2.3.2.3 Ethyl ester **6** with KI

Figure 2-25 shows the  $^1\text{H}$ -NMR titration spectra of **6** with successive additions of aliquots of a KI solution. It can be seen that by increasing the amounts of KI to the solution of **6**, downfield chemical shift changes for Ar-H and  $-\text{OCH}_2\text{COOCH}_2\text{CH}_3$  proton singlet signals from  $\delta$  6.546 to 6.770 ppm and  $\delta$  1.306 to 1.368 ppm, respectively. Whereas the figure 2-26 shows the upfield change in chemical shift occurs for  $-\text{SCOCH}_3$  proton from 2.326 ppm to 2.240 ppm. Table 2-11, indicating that complexation occurred between **6** and KI.

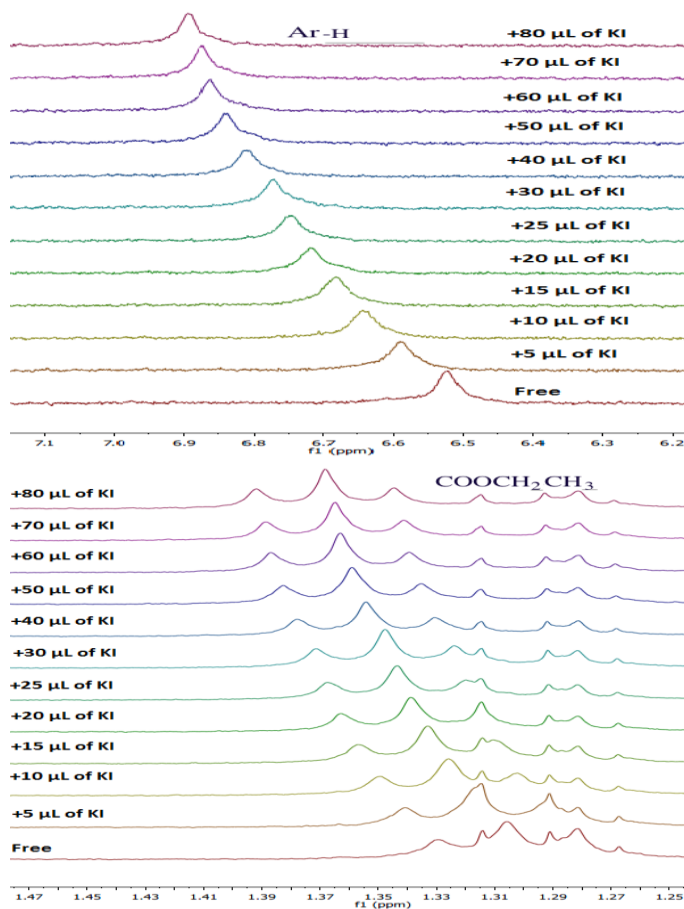


**Figure 2-25.**  $^1\text{H}$  NMR (300 MHz) titration spectra for Ar-H (*Top*) and  $-\text{COOCH}_2\text{CH}_3$  (*Bottom*) of **6** with KI.

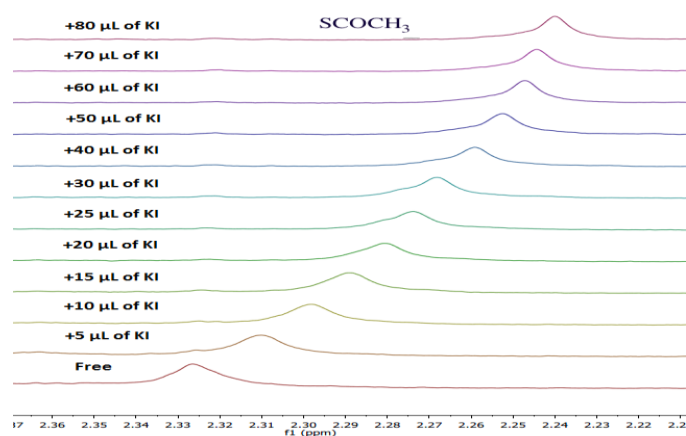


**Figure 2-26.**  $^1\text{H}$  NMR (300 MHz) titration spectra for  $\text{SCOCH}_3$  of **6** with KI.

**Table 2-11.**  $^1\text{H}$  NMR (300 MHz) titration chemical shift data for Ar-H,  $\text{COOCH}_2\text{CH}_3$ , and  $\text{SCOCH}_3$  of **6** ( $1.50 \times 10^{-3}$  M) with KI.

[KI]	G/H	Ar-H $\delta$ (ppm)	$\Delta\delta$ (Hz)	$-\text{COOCH}_2\text{CH}_3$ $\delta$ (ppm)	$\Delta\delta$ (Hz)	$-\text{SCOCH}_3$ $\delta$ (ppm)	$\Delta\delta$ (Hz)
		<b>6.522</b>		<b>1.306</b>		<b>2.327</b>	
3.10E-03	1.86	6.590	20.4	1.316	3.0	2.310	5.1
6.15E-03	3.71	6.642	36.0	1.326	6.0	2.298	8.7
9.15E-03	5.57	6.683	48.3	1.333	8.1	2.289	11.4
1.21E-02	7.43	6.718	58.8	1.339	9.9	2.281	13.8
1.50E-02	9.28	6.742	66.0	1.343	11.1	2.274	15.9
1.79E-02	11.14	6.771	74.7	1.348	12.6	2.268	17.7
2.34E-02	14.86	6.809	86.1	1.354	14.4	2.259	20.4
2.88E-02	18.57	6.838	94.8	1.359	15.9	2.253	22.2
3.41E-02	22.28	6.863	102.3	1.363	17.1	2.247	24.0
3.92E-02	26.00	6.873	105.3	1.365	17.7	2.244	24.9
4.41E-02	29.71	6.893	111.3	1.368	18.6	2.240	26.1

The association constants, as before, were determined using the non-linear 1:1 binding isotherm for the (Ar-H),  $-\text{COOCH}_2\text{CH}_3$  and  $\text{SCOCH}_3$  proton chemical shift changes (Table 2-11). Using the Origin program the concentrations of the guest ([KI]) were plotted against the observed chemical shift changes ( $\Delta\delta$ ) in Hz. The  $K_{\text{assoc}}$  values

were determined to be  $44 \pm 0.5$ ,  $44 \pm 4$  and  $46 \pm 3 \text{ M}^{-1}$  respectively, based on the Ar-H,  $\text{SCOCH}_3$ , and  $\text{COOCH}_2\text{CH}_3$  proton chemical shift changes (Figure 2-27).

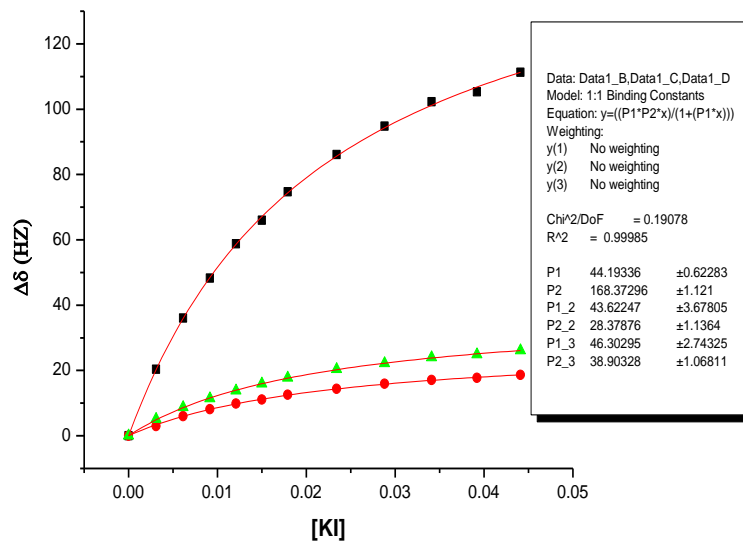


**Figure 2-27.**  $^1\text{H}$  NMR (300 MHz) titration curves for Ar-H,  $-\text{SCOCH}_3$ , and  $\text{COOCH}_2\text{CH}_3$  respectively of **6** ( $1.50 \times 10^{-3} \text{ M}$ ) with KI.

### 2.3.2.4 Methyl ester **5** with KI

Figure 2-28 shows the  $^1\text{H-NMR}$  titration spectra of **5** with successive additions of aliquots of a KI solution. It can be seen that by increasing the amounts of KI to the solution of **5**, downfield chemical shift changes for Ar-H and  $-\text{OCH}_2\text{COOCH}_3$  proton singlet signals from  $\delta$  6.546 to 6.770 ppm and  $\delta$  3.781 to 3.848 ppm, respectively. Whereas figure 2-29 the upfield change in chemical shift occurs for  $-\text{OCH}_2\text{COOCH}_3$  and  $-\text{SCOCH}_3$  proton from 4.733 ppm to 4.657 ppm and 2.232 to 2.272 ppm respectively. Table 2-12, indicating that complexation occurred between **5** and KI.

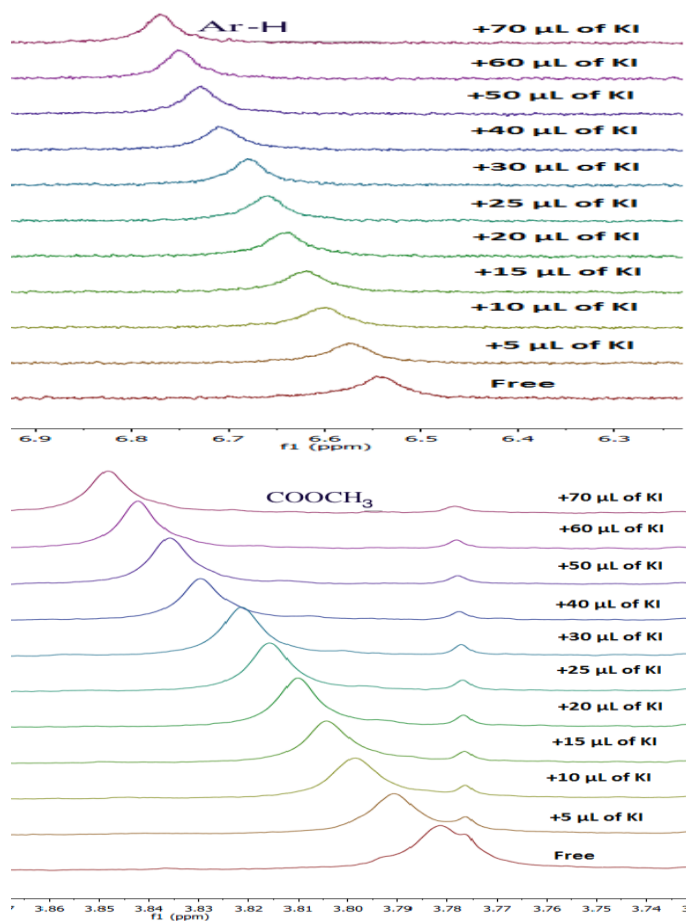


**Figure 2-28.**  $^1\text{H}$  NMR (300 MHz) titration spectra for Ar-H (Top) and  $-\text{COOCH}_3$  (Bottom) of **5** with KI.

**Table 2-12.**  $^1\text{H}$  NMR (300 MHz) titration chemical shift data for Ar-H, and  $\text{COOCH}_3$  of **5** ( $1.50 \times 10^{-3}$  M) with KI.

[KI]	G/H	Ar-H $\delta$ (ppm)	$\Delta\delta$ (Hz)	$\text{COOCH}_3$ $\delta$ (ppm)	$\Delta\delta$ (Hz)
		<b>6.546</b>		<b>3.781</b>	
3.10E-03	1.86	6.575	8.7	3.791	3.0
6.15E-03	3.71	6.602	16.8	3.799	5.4
9.15E-03	5.57	6.621	22.5	3.804	6.9
1.21E-02	7.43	6.64	28.5	3.810	8.7
1.50E-02	9.28	6.66	34.2	3.816	10.5
1.79E-02	11.14	6.68	40.2	3.821	12.0
2.34E-02	14.86	6.71	48.3	3.829	14.4
2.88E-02	18.57	6.73	54.9	3.836	16.5
3.41E-02	22.28	6.75	61.2	3.842	18.3
3.92E-02	26.00	6.77	67.2	3.848	20.1

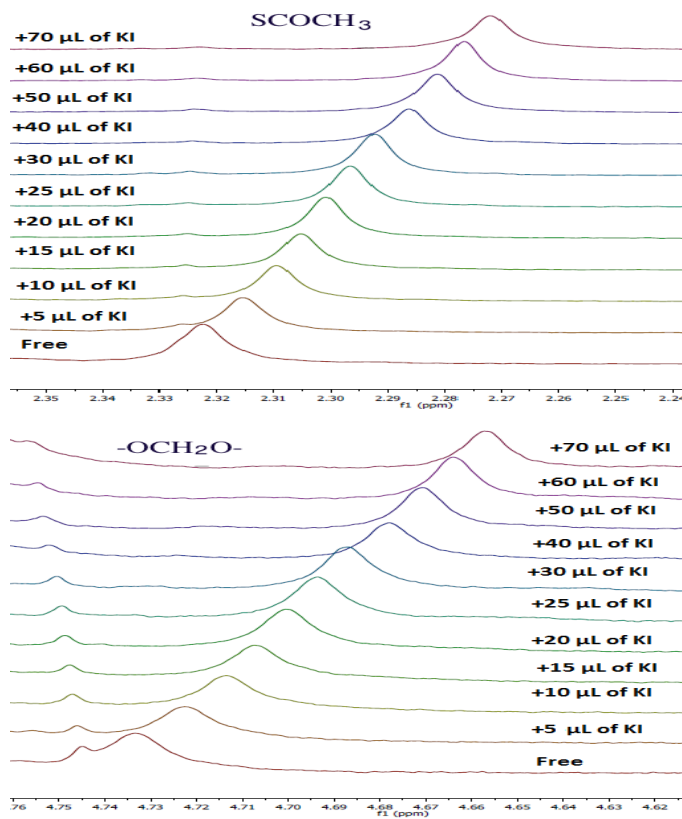


**Figure 2-29.**  $^1\text{H}$  NMR (300 MHz) titration spectra for  $-\text{SCOCH}_3$  (Top) and  $\text{OCH}_2\text{COOCH}_3$  (Bottom) of **5** with KI.

The extent of this complexation was determined by measuring the binding, or association constant ( $K_{assoc}$ ), using the non-linear 1:1 binding isotherm for Ar-H, COOCH<sub>3</sub>, -OCH<sub>2</sub>COOCH<sub>3</sub> and -SCOCH<sub>3</sub> chemical shift changes. (Table 2-12 and 2-13).

**Table 2-13.** <sup>1</sup>H NMR (300 MHz) titration chemical shift data for SCOCH<sub>3</sub>, and OCH<sub>2</sub>COOCH<sub>3</sub> of **5** (1.50×10<sup>-3</sup> M) with KI.

[KI]	G/H	SCOCH <sub>3</sub> δ(ppm)	Δδ (Hz)	-OCH <sub>2</sub> COOCH <sub>3</sub> δ(ppm)	Δδ (Hz)
		<b>2.322</b>		<b>4.733</b>	
3.10E-03	1.86	2.315	2.1	4.722	3.3
6.15E-03	3.71	2.309	3.9	4.713	6.0
9.15E-03	5.57	2.305	5.1	4.707	7.8
1.21E-02	7.43	2.301	6.3	4.700	9.9
1.50E-02	9.28	2.297	7.5	4.694	11.7
1.79E-02	11.14	2.292	9.0	4.687	13.8
2.34E-02	14.86	2.286	10.8	4.678	16.5
2.88E-02	18.57	2.281	12.3	4.671	18.6
3.41E-02	22.28	2.277	13.5	4.664	20.7
3.92E-02	26.00	2.272	15.0	4.657	22.8

The association constants, as in all cases previously described, were determined using the non-linear 1:1 binding isotherm for the Ar-H, -OCH<sub>2</sub>COOCH<sub>3</sub>, -COOCH<sub>3</sub> and -SCOCH<sub>3</sub> proton singlet chemical shift changes. The  $K_{assoc}$  values were determined to be 18±0.5, 21±2, 19±2, and 20±1 M<sup>-1</sup> respectively based on the above order. (Figure 2-30).

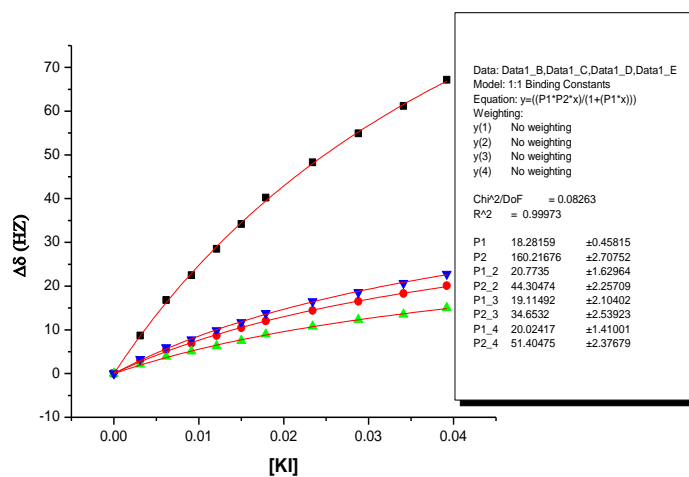


**Figure 2-30.**  $^1\text{H}$  NMR (300 MHz) titration curves for Ar-*H*,  $-\text{OCH}_2\text{COOCH}_3$ ,  $-\text{COOCH}_3$ , and  $-\text{SCOCH}_3$ , respectively of **5** ( $1.50 \times 10^{-3}$  M) with KI.

### 2.3.3 Complexation of Methyl ester calixarene **5** and its corresponding ethyl ester **6** with AgTFA

#### 2.3.3.1 Ethyl ester **6** with AgTFA

Figure 2-31 shows the  $^1\text{H}$ -NMR titration spectra of **6** with successive additions of aliquots of a AgTFA solution. It can be seen that by increasing the amounts of AgTFA to the solution of **6**, downfield chemical shift changes for Ar-*H* and  $-\text{OCH}_2\text{COOCH}_2\text{CH}_3$  proton singlet signals from  $\delta$  6.522 to 6.060 ppm and  $\delta$  1.322 to 1.414 ppm, respectively. Whereas the figure 2-31 (bottom) the upfield change in chemical shift occurs for  $\text{SCOCH}_3$  proton from 2.327 to 2.174 ppm respectively. Table 2-14, indicating that complexation occurred between **6** and AgTFA.

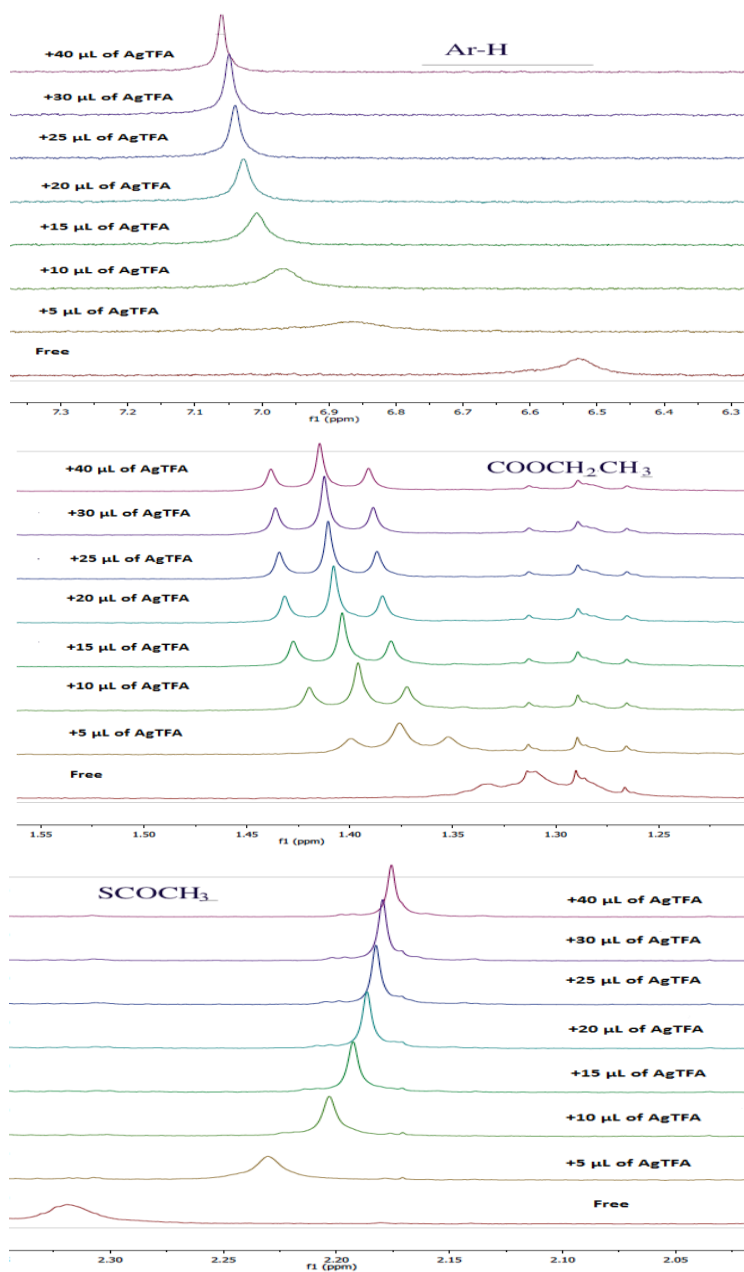


**Figure 2-31.** <sup>1</sup>H NMR (300 MHz) titration spectra for Ar-H (Top), -COOCH<sub>2</sub>CH<sub>3</sub> (Middle) and SCOCH<sub>3</sub> (Bottom) of **6** with AgTFA.

**Table 2-14.**  $^1\text{H}$  NMR (300 MHz) titration chemical shift data for Ar-*H*,  $\text{COOCH}_2\text{CH}_3$ , and  $\text{SCOCH}_3$  of **6** ( $1.50 \times 10^{-3}$  M) with AgTFA.

[AgTFA]	G/H	Ar- <i>H</i> $\delta$ (ppm)	$\Delta\delta$ (Hz)	$\text{COOCH}_2\text{CH}_3$ $\delta$ (ppm)	$\Delta\delta$ (Hz)	- $\text{SCOCH}_3$ $\delta$ (ppm)	$\Delta\delta$ (Hz)
		<b>6.522</b>		<b>1.322</b>		<b>2.327</b>	
2.81E-03	1.67	6.936	112.2	1.388	19.8	2.211	26.4
5.58E-03	3.31	7.001	131.7	1.402	24.0	2.192	32.1
8.29E-03	4.93	7.013	135.3	1.404	24.6	2.189	33.0
1.10E-02	6.68	7.04	142.5	1.409	26.1	2.181	35.4
1.36E-02	8.35	7.045	144.9	1.411	26.7	2.179	36.0
1.62E-02	10.02	7.055	147.9	1.413	27.3	2.175	37.2
2.13E-02	13.63	7.060	149.4	1.414	27.6	2.174	37.5

Using the Origin program the concentration of the guest [AgTFA] was plotted against the chemical shift changes ( $\Delta\delta$ ) in Hz. The  $K_{\text{assoc}}$  values were determined to be  $883 \pm 30$ ,  $740 \pm 128$  and  $682 \pm 84$   $\text{M}^{-1}$  respectively, based on the Ar-*H*, - $\text{SCOCH}_3$ , and  $\text{COOCH}_2\text{CH}_3$  proton chemical shift changes (Figure 2-32).

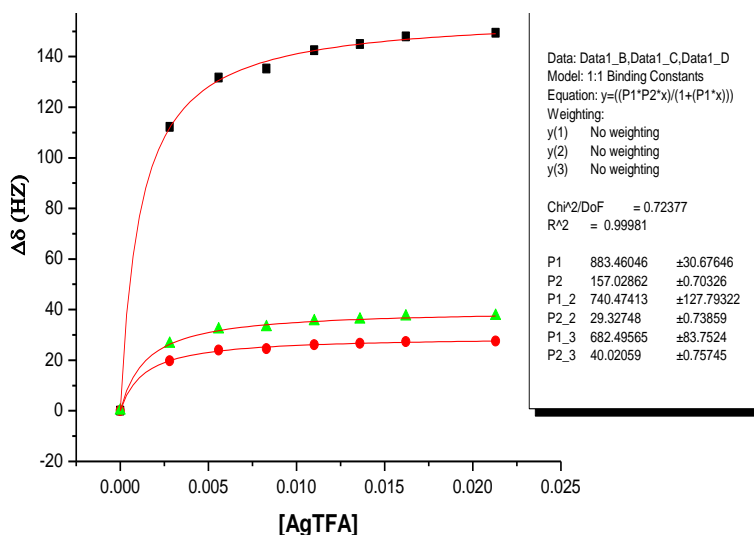


**Figure 2-32.**  $^1\text{H}$  NMR (300 MHz) titration curves for Ar-*H*,  $\text{SCOCH}_3$ , and  $\text{COOCH}_2\text{CH}_3$  respectively of **6** ( $1.50 \times 10^{-3}$  M) with AgTFA.

### 2.3.3.2 Methyl ester 5 with AgTFA

**Figure 2-33** shows the  $^1\text{H-NMR}$  titration spectra of 5 with successive additions of aliquots of a AgTFA solution. It can be seen that by increasing the amounts of AgTFA to the solution of 5, downfield chemical shift changes for Ar-*H* and  $-\text{OCH}_2\text{COOCH}_3$  proton singlet signals from  $\delta$  6.542 to 7.042 ppm and  $\delta$  3.770 to 3.925 ppm, respectively. Table 2-15, indicating that complexation occurred between 5 and AgTFA.

**Table 2-15.**  $^1\text{H NMR}$  (300 MHz) titration chemical shift data for Ar-*H*, and  $\text{COOCH}_3$  of 5 ( $1.5 \times 10^{-3}$  M) with AgTFA.

[AgTFA]	G/H	Ar- <i>H</i> $\delta$ (ppm)	$\Delta\delta$ (Hz)	$\text{COOCH}_3$ $\delta$ (ppm)	$\Delta\delta$ (Hz)
		<b>6.546</b>		<b>3.774</b>	
2.81E-03	1.79	6.768	70.8	3.853	23.7
5.58E-03	3.58	6.857	97.5	3.883	32.7
8.29E-03	5.37	6.906	112.2	3.899	37.5
1.10E-02	7.15	6.93	120.6	3.909	40.5
1.36E-02	8.94	6.956	127.2	3.916	42.6
1.62E-02	10.73	6.971	131.7	3.921	44.1
1.87E-02	12.52	6.984	135.6	3.925	45.3
2.13E-02	14.31	6.994	138.6	3.928	46.2
2.62E-02	17.89	7.009	143.1	3.933	47.7
3.55E-02	25.04	7.029	149.1	3.939	49.5

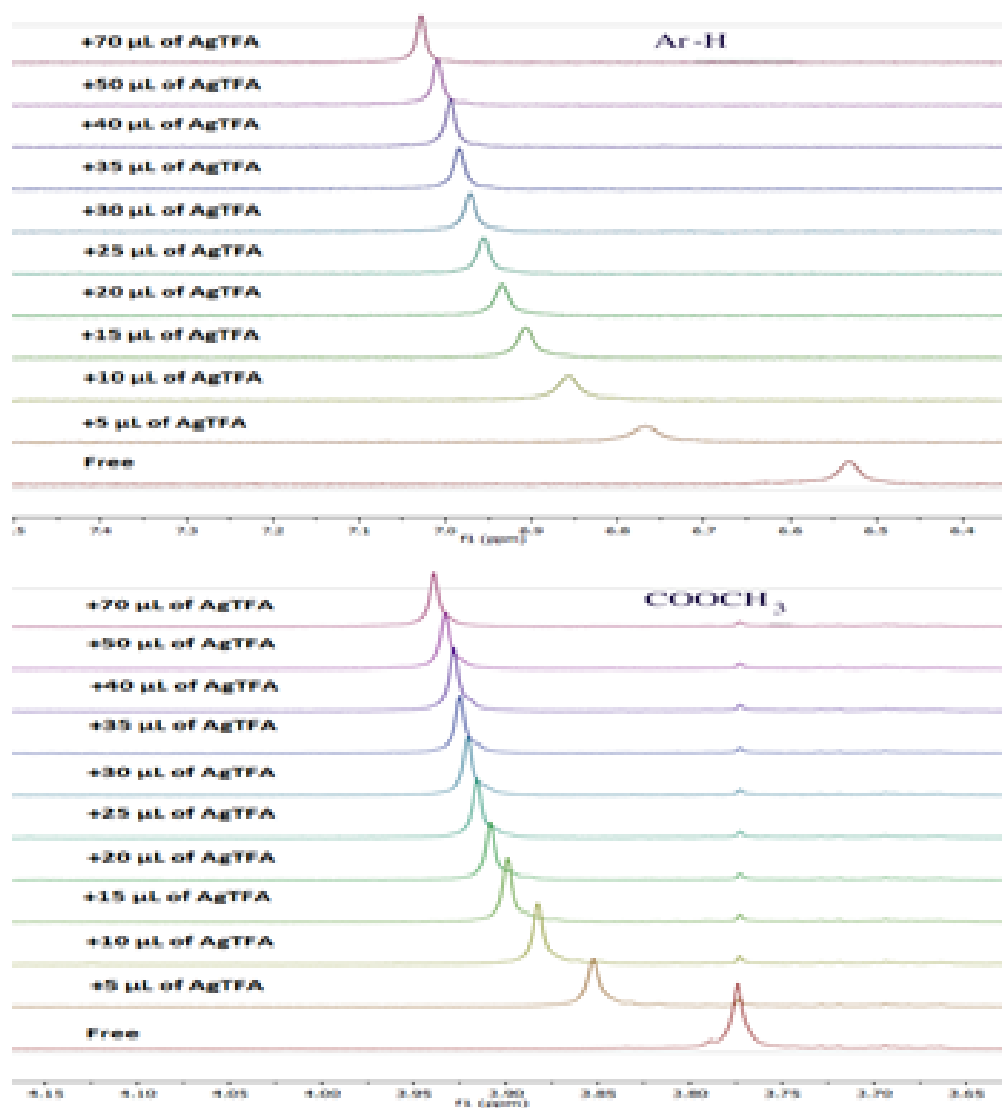


**Figure 2-33.**  $^1\text{H}$  NMR (300 MHz) titration spectra for Ar-H (Top),  $\text{COOCH}_3$  (Bottom) of **5** with AgTFA.

Figure 2-34 shows the  $^1\text{H}$ -NMR titration spectra of **5** with successive additions of aliquots of a AgTFA solution. It can be seen that by increasing the amounts of AgTFA to the solution of **5**, upfield chemical shift changes for  $-\text{OCH}_2\text{COOCH}_3$  and  $-\text{SCOCH}_3$  proton singlet signals from  $\delta$  4.732 to 4.593 ppm and  $\delta$  2.315 to 2.163 ppm, respectively. Table 2-16, indicating that complexation occurred between **5** and AgTFA.

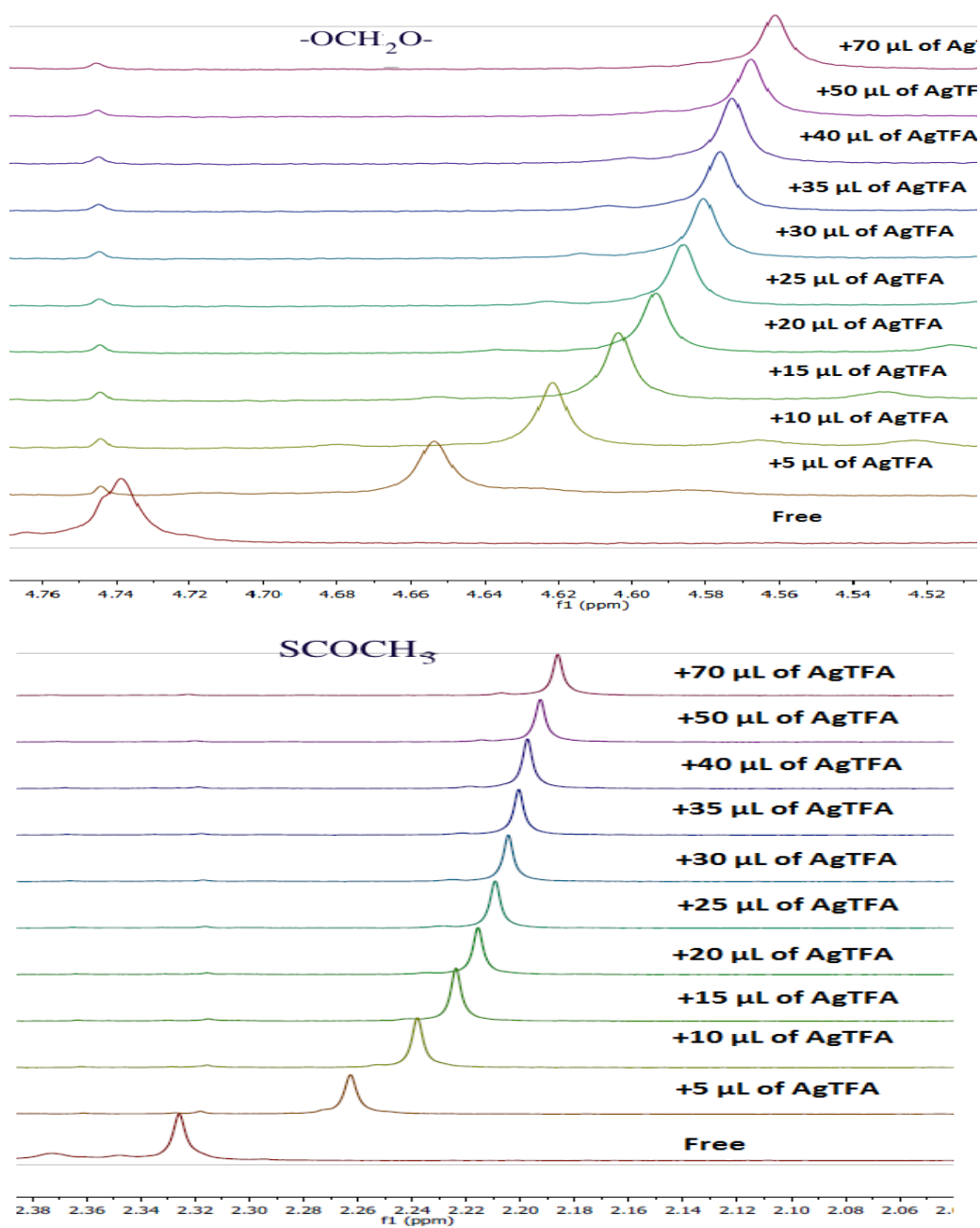


**Figure 2-34.** <sup>1</sup>H NMR (300 MHz) titration spectra for  $-OCH_2COOCH_3$  (Top) and  $SCOCH_3$  (Bottom) of **5** with AgTFA.

**Table 2-16.**  $^1\text{H}$  NMR (300 MHz) titration chemical shift data for  $\text{SCOCH}_3$ , and  $\text{OCH}_2\text{COOCH}_3$  of **5** ( $1.50 \times 10^{-3}$  M) with AgTFA.

[AgTFA]	G/H	$-\text{SCOCH}_3$ $\delta(\text{ppm})$	$\Delta\delta$ (Hz)	$-\text{OCH}_2\text{COOCH}_3$ $\delta(\text{ppm})$	$\Delta\delta$ (Hz)
		2.329		4.742	
2.81E-03	1.79	2.263	18.9	4.606	25.5
5.58E-03	3.58	2.238	26.4	4.654	35.1
8.29E-03	5.37	2.224	30.6	4.622	40.5
1.10E-02	7.15	2.216	33.0	4.604	43.5
1.36E-02	8.94	2.209	35.1	4.594	45.9
1.62E-02	10.73	2.204	36.6	4.586	47.4
1.87E-02	12.52	2.201	37.5	4.581	48.9
2.13E-02	14.31	2.197	38.7	4.576	49.8
2.62E-02	17.89	2.193	39.9	4.573	51.3
3.55E-02	25.04	2.186	42.0	4.568	53.1

Table 2-17 shows the extent of this complexation that was determined by measuring the binding, or association constant ( $K_{assoc}$ ), using the non-linear 1:1 binding isotherm for  $-\text{OCH}_2\text{COOCH}_3$ , and  $-\text{SCOCH}_3$  chemical shift changes. The  $K_{assoc}$  values were determined to be  $265 \pm 3$ ,  $271 \pm 9$ ,  $236 \pm 9$  and  $271 \pm 8$   $\text{M}^{-1}$  respectively, based on the aromatic singlet signals  $-\text{OCH}_2\text{COOCH}_3$  and  $-\text{SCOCH}_3$  proton chemical shift changes (Figure 2-35).

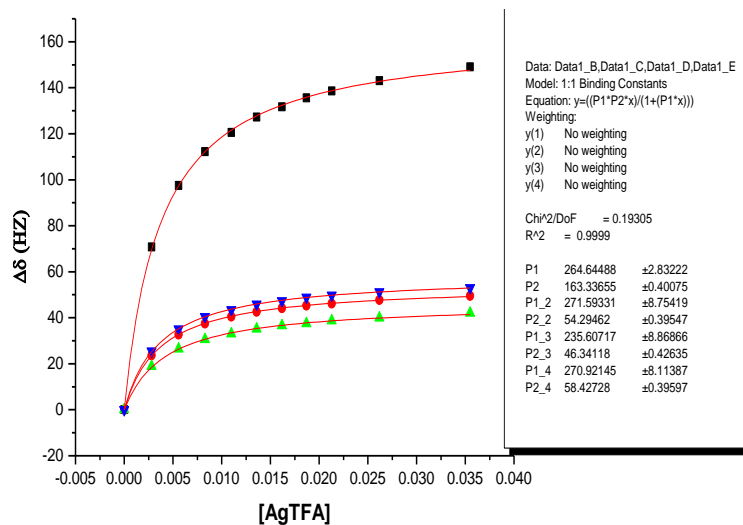


**Figure 2-35.**  $^1\text{H}$  NMR (300 MHz) titration curves for Ar- $H$ ,  $-\text{OCH}_2\text{COOCH}_3$ ,  $-\text{COOCH}_3$ , and  $-\text{SCOCH}_3$  respectively of **5** ( $1.50 \times 10^{-3}$  M) with AgTFA.

### 2.3.4 Comparison between the $K_{\text{assoc}}$ values of methyl ester calix **5** and ethyl ester calix **6**

With the calcium salts examined, no discernable chemical shift changes could be seen, with the exception of  $\text{CaCl}_2$ ,  $\text{CaBr}_2$  and  $\text{CaI}_2$  although only very small chemical shift changes were observed with  $\text{CaBr}_2$ . It should be noted that  $\text{CaBr}_2$  had only very limited solubility in the solvent system used for the NMR titrations. Calix **5** and **6** showed different  $K_{\text{assoc}}$  values for  $\text{CaCl}_2$ ,  $\text{CaBr}_2$  and  $\text{CaI}_2$ . Ethyl ester calix **6** showing the higher association value with AgTFA. The  $K_{\text{assoc}}$  values were determined based upon the chemical shift changes for the proton signals which showed the greatest changes. Table 2-17 lists the average  $K_{\text{assoc}}$  values.

For the calcium salts whose  $K_{\text{assoc}}$  values could be determined,  $\text{CaCl}_2$  had higher values than  $\text{CaI}_2$  for both calixarenes **5** and **6**. This suggests that the mode of

complexation could involve the salt binding to the host calixarenes in the solvent system used, as tight contact linear ion triplets, in which case, the larger iodide ions would not be as easily accommodated as with the corresponding chloride ions. NaI as a linear contact ion pair showed the strongest binding and this was higher than that seen for KI which has the larger cation.

**Table 2-17.**  $K_{assoc}$  values for **5** and **6** with representative salts.

Salt	$K_{assoc}$ of <b>5</b>	$K_{assoc}$ of <b>6</b>
CaCl <sub>2</sub>	78	179
CaBr <sub>2</sub>	1	1
CaI <sub>2</sub>	18	34
NaI	294	611
KI	18	44
AgTFA	254	682

NaCl, KCl, KBr and KNO<sub>3</sub> which were considered for comparison purposes were not sufficiently soluble in the solvent mixture used in the titration experiments. In order to determine where the site of binding actually occurs in these calixarenes, AgTFA containing the soft-metal ion Ag<sup>+</sup> was used as a probe. As can be seen in Table 2-16, AgTFA showed the highest binding constant with calix **6** than **5**.

With Ca(TFA)<sub>2</sub> in the same solvent system however, by way of contrast, no chemical shift changes could be observed. This suggests that the primary site for the Ag<sup>+</sup> complexation could be the upper-rim thioacetate S atoms and that due to the large TFA counterions (including Br<sup>-</sup>, I<sup>-</sup>, ClO<sub>4</sub><sup>-</sup>, NO<sub>3</sub><sup>-</sup>) Ca<sup>2+</sup> cannot be easily accommodated within the narrow rims of the host calixarenes.

## 2.4. References

1. For leading references see (a) Calixarenes: An Introduction, ed. Gutsche, C. D., Royal Society of Chemistry, Cambridge, UK, 2nd edn, 2008; (b) Calixarenes 2001 Asfari, ed. Z.; Böhmer, V.; Harrowfield, J.; and Vicens, J. Kluwer Academic Publishers, Dordrecht, The Netherlands, 2001; (c) Calixarenes in the Nanoworld, ed. J. Vicens and J. Harrowfield, Springer, Dordrecht, Holland, 2007.
2. For a recent review of multifunctionalization of calixarenes see Sliwa, W.; Deska, M. *ARKIVOC* **2011**, 496–551.
3. Mokhtari, B.; Pourabdollah, K.; Dalali, N. *J. Coord. Chem.* **2011**, *64*, 743–794.
4. Kim, H. J.; Lee, M. H.; Mutihac, L.; Vicens, J.; Kim, J. S. *Chem. Soc. Rev.*, **2012**, *41*, 1173–1190.
5. For a recent example of a potassium ion sensor involving surface plasmon resonance (SPR) a calix[4]crown SAM on a gold surface see Chen, H; Gal, Y.-S; Kim, S.-H.; Choi, H.-J.; Oh, M. C.; Lee, J.; Koh, K. *Sens. Actuators B.* **2008**, *113*, 577–581.
6. (a) Daniel, M. C.; Astruc, D. *Chem. Rev.*, **2004**, *104*, 293–346; (b) Templeton, A. C.; Wuelfing M. P.; Murray, R. W. *Acc. Chem. Res.*, **2000**, *33*, 27–36.
7. Vericat, C.; Vela, M. E.; Benitez, G.; Carro, P.; Salvarezza, R. C. *Chem. Soc. Rev.*, **2010**, *39*, 1805–1834.
8. Link, S.; El-Sayed, M. A. *Int. Rev. Phys. Chem.*, **2000**, *19*, 409–453.
9. Kamat, P. V. *J. Phys. Chem. B.* **2002**, *106*, 7729–7744.

10. Kneipp, K.; Kneipp, H.; Itzkan, I.; Dasari, R. R.; Feld, M. S. *Chem. Rev.*, **1999**, *99*, 2957–2975.
11. Chen, H.; Gal, Y.-S.; Kim, S.-H.; Choi, H.-J.; Oh, M.-C.; Lee, J.; Koh, K. *Sens. Actuators, B*, **2008**, *133*, 577–581.
12. Ji, H. F.; Finot, E.; Dabestani, R.; Thundat, T.; Brown, G. M.; Britt, P. F. *Chem. Commun.*, **2000**, 457–458.
13. Zhang, S.; Palkar, A.; Echegoyen, L. *Langmuir*, **2006**, *22*, 10732–10738.
14. Georghiou, P. E.; Rahman, S.; Valluru, G.; Dawe, L. N.; Rahman, S. M. S.; Alodhayb, A. N.; Beaulieu, L. Y. *New J. Chem.* **2013**, *37*, 1298–1301.
15. Calixarene **5** can be formally named as 5,11,17,23-tetrakis-(3-propylthioacetate)-25,26,27,28-tetrakis-[(methoxycarbonyl)methoxy]calix[4]arene.
16. Chawla, H. M.; Santra, A. *Synth. Commun.*, **2001**, *31*, 2605–2611.
17. Gutsche, C. D.; Levine, J. A.; Sujeeth, P. K. *J. Org. Chem.*, **1985**, *50*, 5802–5806.
18. Kimura, M.; Yokokawa, M.; Sato, S.; Fukawa, T.; Mihara, T. *Chem. Lett.*, **2011**, 1402–1404.
19. Buskas, T.; Soderberg, E.; Konradsson, P.; Fraser-Reid, B. J. *J. Org. Chem.*, **2000**, *65*, 958–963.
20. (a) Connors, K.A. *Binding Constants*, Wiley, New York, 1987. (b) Association constants were calculated using a non-linear curve fitting using the program ORIGIN Pro 6 from Origin Lab Corporation.

## Chapter 3

### **<sup>1</sup>H-NMR Spectroscopic Studies of Tetrabutylammonium Halides with Different Solvents**

#### **3.1 Introduction**

In this Chapter, a continuing study of the supramolecular complexation behaviour of tetra-*n*-butylammonium halides (TBAX: X = Cl<sup>-</sup>, Br<sup>-</sup>) in different solvents i.e. CD<sub>3</sub>OD, (CD<sub>3</sub>)<sub>2</sub>CO, CD<sub>2</sub>Cl<sub>2</sub>, CD<sub>3</sub>CN and (CD<sub>3</sub>)<sub>2</sub>SO, using <sup>1</sup>H-NMR spectroscopy is described. A previous study by Sleem et al.<sup>1</sup> had shown that the reference residual proton signal (i.e. from CHCl<sub>3</sub>) in the CDCl<sub>3</sub> solvent in <sup>1</sup>H-NMR titration experiments was shifted downfield after successive amounts of TBAX salts were added to the solutions of host macrocyclic amides. As a result of Sleem's work, it was concluded that a study to quantify the extent of the chemical shift changes of the residual protons of other commonly-employed NMR solvents was also necessary. The experiments described in this present Chapter show that linear concentration-chemical shift relationships for the residual protons in each of the solvents tested (CD<sub>3</sub>OD, (CD<sub>3</sub>)<sub>2</sub>CO, CD<sub>2</sub>Cl<sub>2</sub>, CD<sub>3</sub>CN and (CD<sub>3</sub>)<sub>2</sub>SO) could be obtained from the resulting titration plots obtained from the addition of the TBAX salts to these commonly-employed NMR solvents.

#### **3.1.1 NMR studies of the complexation of tetrabutylammonium halides (TBAX)**

Numerous research groups have used spectroscopic methods including <sup>1</sup>H-NMR spectroscopy<sup>2</sup> to investigate the complexation of various host or receptor molecules such as, for example, calixarene derivatives with tetra-*n*-butylammonium salts (TBAX: where X = Cl<sup>-</sup>, Br<sup>-</sup> or I<sup>-</sup>) and with other organic ammonium salts.<sup>3,4</sup> For instance, Nam et al.<sup>5</sup>

demonstrated the synthesis of two new calix[4]arene-based anion receptors, and examined their binding studies with TBAX salts ( $X = \text{Cl}^-$ ,  $\text{Br}^-$  or  $\text{F}^-$ ) by employing  $^1\text{H}$ -NMR titrations in  $\text{CDCl}_3$ . The titration spectra presented in the study by Nam et al., when examined by Sleem et al., revealed that there was an occurrence of down-field chemical shift changes for the residual proton signal of the  $\text{CDCl}_3$  solvent. However, Nam et al. failed to rationalize this phenomenon.

As described further by Sleem in his thesis,<sup>6</sup> Green and Martin<sup>7</sup> conducted an extensive and insightful study in 1986, which reported the interactions between tetra-*n*-butylammonium chloride, bromide and iodide with various trihalomethanes, including chloroform. The study was conducted in two different solvents, acetonitrile and tetrachloromethane, using both  $^1\text{H}$ -NMR and IR spectroscopy. They found also that there were changes in the  $^1\text{H}$ -NMR chemical shifts of the trihalomethane protons upon the addition of the TBA halides to those solvents. Figure 3.1, adapted from Green and Martin's paper, demonstrates a typical titration curve for the complex formation of  $\text{CHCl}_3$  with  $\text{TBABr}$  in  $\text{CH}_3\text{CN}$  solution. The authors determined the  $K$  value using a modified Benesi-Hildebrand plot and found it to be  $0.73 \pm 0.09 \text{ M}^{-1}$ . Taking their data as presented in Figure 3-1 and using the non-linear 1:1 binding isotherm employed in all of the binding studies reported in the earlier Chapters of this thesis, a comparable value of  $0.94 \times 0.04 \text{ M}^{-1}$  was determined by Sleem et al.<sup>6</sup>

Green and Martin further reported a study of an IR spectroscopic titration of  $\text{CD}_3\text{Cl}$  with  $\text{TBACl}$  and  $\text{TBABr}$  in  $\text{CCl}_4$  solvent where the characteristic "C–D H-bonded stretch band"<sup>8,9</sup> in the  $2170\text{--}2200 \text{ cm}^{-1}$  range was observed for each of the complexes in

$\text{CDCl}_3\text{:TBACl}$  and  $\text{CDCl}_3\text{:TBABr}$ . The band's intensity was found to be proportional to the respective complexes' concentrations as measured using the equilibrium constant that the authors obtained from the  $^1\text{H}$  NMR measurements.

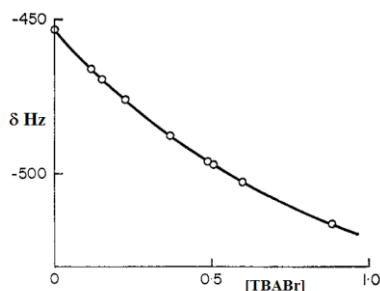


**Figure 3-1.** Proton shielding of 0.1 M  $\text{CHCl}_3$  in  $\text{CH}_3\text{CN}$  as a function of TBABr concentration. [Adapted with permission from Reference 6]

It was also possible to see clearly the linear relationships between the concentration of the complex, and the intensity of the H-bond band. It was therefore concluded that the observed association (or binding constants), which increased with the decrease in the ionic radius of the anion (i.e.  $\text{Cl}^- > \text{Br}^- > \text{I}^-$ ) could be attributed to relatively strongly-bound 1:1 complexes that were formed between the anions and the chloroform in the dilute solutions of the weakly-interacting solvent. The authors further concluded that the complexes' association energies were dominated by the carbon-halogen polarization structure of the molecules instead of the C—H fragment electrophilicity. Moreover, it was concluded that the observed data could be accounted for by a simple monopole-dipole electrostatic model. The evidence suggested that, for chloroform, the interaction was between that halide ion and the hydrogen of the chloroform, whereas for tribromo- and

triiodomethane, the interactions were between the halide ion and the halogens of the  $\text{CHBr}_3$  and  $\text{CHI}_3$ .<sup>10</sup>

In their 2012 paper, Sleem et al.<sup>1</sup> reported the synthesis of a new tetraamido macrocyclic compound which is related to a macrocyclic compound which Lüning and coworkers' had reported in an earlier study. The complexation behaviour with various TBAX salts ( $\text{X} = \text{Cl}^-$ ,  $\text{Br}^-$ ,  $\text{I}^-$ ,  $\text{BF}_4^-$  and  $\text{PF}_6^-$ ) using  $^1\text{H-NMR}$  titration experiments in  $\text{CDCl}_3$  solutions were investigated in this study. Sleem et al. found that gradual addition of TBABr to the solution of the tetraamido macrocyclic compound resulted in significant shifts for the residual  $^1\text{H}$  signal of the solvent. The authors made similar observations during the titration experiments in  $\text{CDCl}_3$  using TBAX salts with several other chromotropic acid-based macrocyclic sulphonamides and these findings were also reported recently.<sup>11</sup> An X-ray structure<sup>12</sup> shown in Figure 3.2, lent further support for the hypothesis that interactions between the halides and the protons of the solvent are responsible for the chemical shift changes seen in the  $^1\text{H}$  NMR titration experiments, since as can be seen in Figure 3-2 the closest contacts are between  $\text{Br}^-$  ions and the H atoms of the  $\text{CHCl}_3$ .

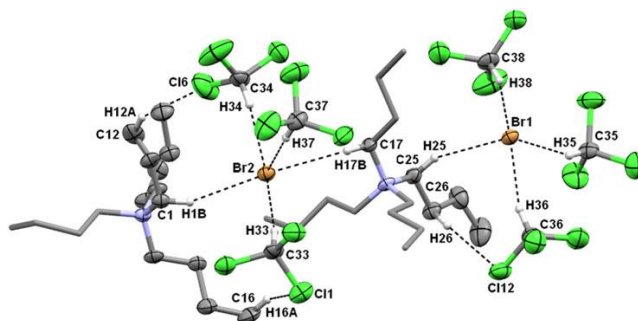


**Figure 3-2.** Asymmetric unit of  $\text{TBABr}:\text{CHCl}_3$ . [Adapted with permission from Reference 11]

Figure 3-3 shows the straight-line relationships between the observed chemical shifts for the  $\text{CDCl}_3$  solvent's residual proton signal and the molar concentrations of the respective TBAX salts. The least-squares linear regression method was used in obtaining the slopes of the chloride, bromide, iodide and tetrafluoroborate salts, which were found to be 0.58, 0.54, 0.45 and 0.16 ppm  $\text{M}^{-1}$ , respectively.

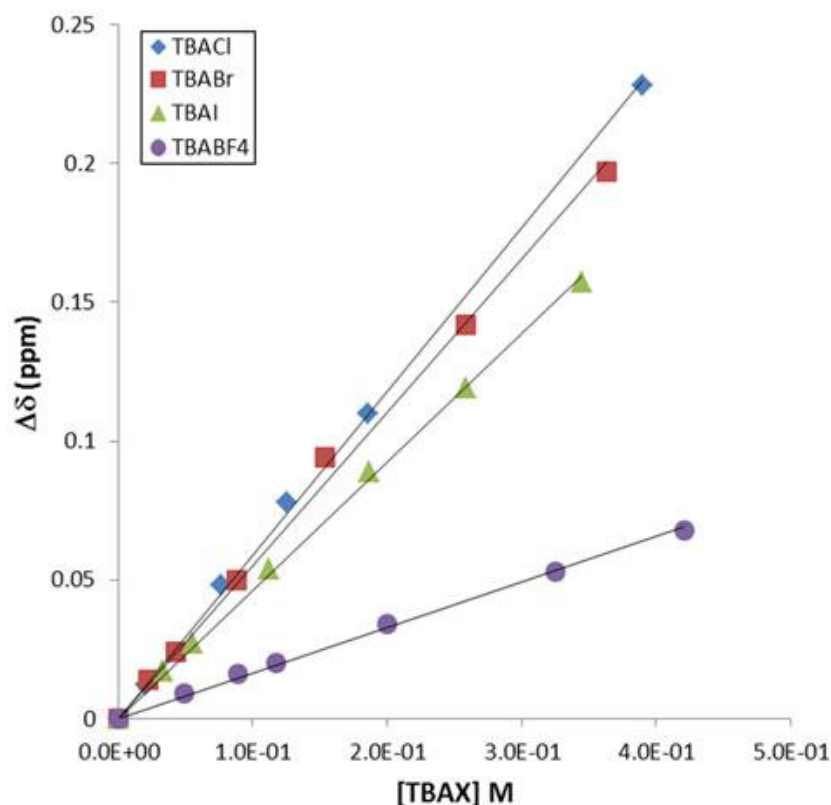


**Figure 3-3.** Least-squares linear plots of the  $\text{CDCl}_3$ :TBAX titrations. [Adapted with permission from Reference 11]

Referees to the *Supramolecular Chemistry* paper recommended extending the study to the other most-commonly used solvents in NMR-based supramolecular complexation studies. The work described in this Chapter therefore had these objectives.

### 3.2 Experimental section

The anhydrous TBAX salts were used as supplied by Sigma-Aldrich or Alfa-Aesar without any further purification. Acetone- $d_6$  [(CD<sub>3</sub>)<sub>2</sub>CO; 99.9% D], methanol- $d_4$  (CD<sub>3</sub>OD; 99.9% D), acetonitrile- $d_3$  (CD<sub>3</sub>CN; 99.9% D), and DMSO- $d_6$  [(CD<sub>3</sub>)<sub>2</sub>SO; 99.9% D] all containing 0.05% v/v tetramethylsilane (TMS) were used as supplied by Cambridge Isotope Labs. Dichloromethane- $d_2$  (CD<sub>2</sub>Cl<sub>2</sub>; 99.9% D) as supplied, contained no TMS, therefore CD<sub>2</sub>Cl<sub>2</sub> containing 0.05% v/v TMS were prepared by adding 50  $\mu$ L amounts of TMS to 1.0 mL volumes of the as-supplied DCM- $d_2$ . For the titration studies, varying mg aliquots of each of the TBAX salts were added to the 0.6 mL volumes of the respective solvents in the NMR sample tubes. After each addition, the mixtures were shaken for 5 min and the resulting <sup>1</sup>H-NMR spectra at 500 MHz after each addition were recorded at 24 $\pm$ 1°C. For all of these solutions, the <sup>1</sup>H-NMR spectra were referenced to the ‘external’ TMS (i.e. the 0.05% v/v TMS in each of the deuterated solvents which were used) placed in a coaxial insert tube’s capillary portion. This precluded any contact between the TBAX and the TMS. Plots of the observed chemical shift changes ( $\Delta\delta$  in ppm) for the residual proton signals of the solvents against the molar concentrations of the TBAX salts in the solutions were produced.

### 3.3 Complexation studies of different TBAX halides with different solutions

In preliminary <sup>1</sup>H-NMR experiments conducted for this study, the maximum proton chemical shift changes were first determined using saturated solutions of the TBA halides in each of the different solvents. The titration studies were conducted by addition of varying amounts of each of the TBAX salts into each of the NMR tubes. The resulting

$^1\text{H}$ -NMR spectra obtained after shaking the sample for 5 minutes upon each addition were recorded at  $24\pm 1^\circ\text{C}$ . Figures 3-4, 3-6, 3-8, 3-10 and 3-12 show the chemical shift changes for the signals of the residual protons of the respective solvents. The observed chemical shifts changes ( $\Delta\delta$  Hz) were plotted against the molar concentrations of the TBAX salts in the solution. Slopes of 677, 617, 540, 251 and 203  $\text{Hz}\cdot\text{M}^{-1}$  were obtained from the least-squares linear regression plots of  $(\text{CD}_3)_2\text{CO}$ ,  $\text{CD}_3\text{OD}$ ,  $\text{CD}_2\text{Cl}_2$ ,  $\text{CD}_3\text{CN}$ , and  $\text{DMSO}-d_6$  solvents respectively, and are shown in each of the respective Figures presented below.

### 3.3.1 Titration of TBACl in acetone- $d_6$ ( $(\text{CD}_3)_2\text{CO}$ )

Figure 3.4 shows the titration spectra for TBACl in acetone- $d_6$  ( $(\text{CD}_3)_2\text{CO}$ ) in which the upfield chemical shift changes from 2.059 ppm to 1.883 ppm can be seen for the residual proton signal of  $\text{C}_3\text{D}_6\text{O}$ . Table 3-1 summarizes the data which were plotted in Figure 3-5.

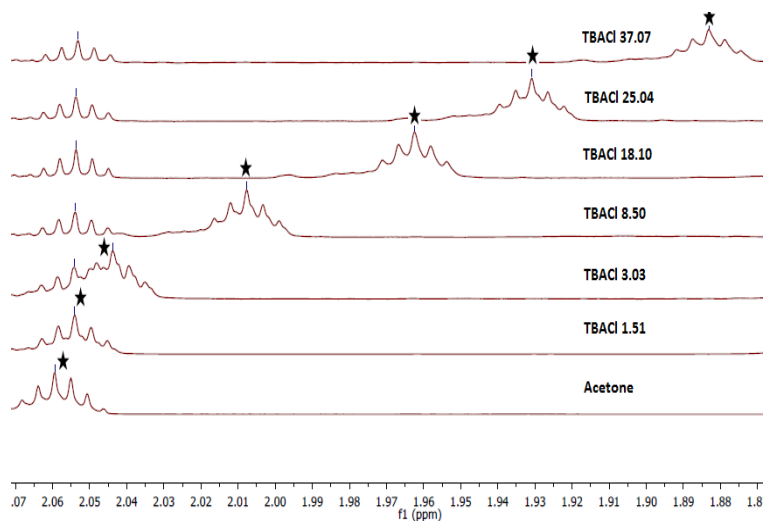


**Figure 3-4.**  $^1\text{H}$  NMR (500 MHz) expanded titration spectra for the residual proton signal of the  $(\text{CD}_3)_2\text{CO}$  solvent with increasing amounts of TBACl.

**Table 3-1.**  $^1\text{H-NMR}$  (500 MHz) titration data in  $(\text{CD}_3)_2\text{CO}$ .

Sample	TBACl (g)	Moles of TBACl	[TBACl]	$(\text{CD}_3)_2\text{CO}$ $\delta(\text{ppm})$	$\Delta\delta(\text{Hz})$
		0	0	2.059	0
1	1.50E-03	5.40E-06	5.40E-03	2.055	2
2	3.00E-03	1.08E-05	1.08E-02	2.044	7.5
3	8.50E-03	3.06E-05	3.06E-02	2.009	25
4	1.81E-02	6.51E-05	6.51E-02	1.963	48
5	2.50E-02	9.00E-05	9.00E-02	1.931	64
6	3.70E-02	1.33E-04	1.33E-01	1.883	88

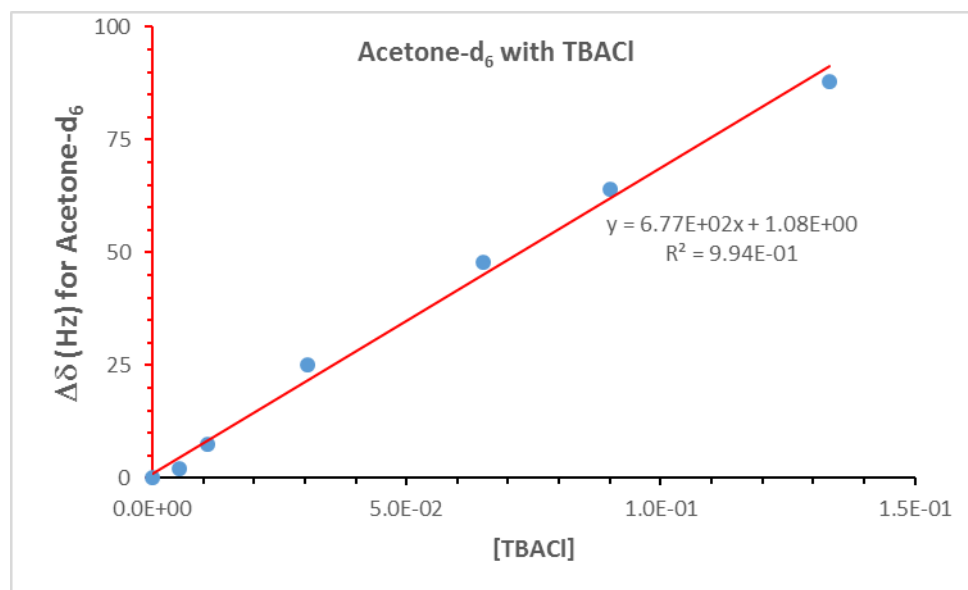


**Figure 3-5.** Least-squares linear regression plot for the  $(\text{CD}_3)_2\text{CO}$ : TBACl data.

### 3.3.2 Titration of TBACl in acetonitrile- $d_3$ ( $CD_3CN$ )

The titration spectra for TBACl in  $CD_3CN$  are shown in Figure 3-6. It can be seen that increasing the amounts of TBACl added to the  $CD_3CN$  causes downfield changes in the chemical shifts for the residual proton signal of  $CD_3CN$ , from 1.933 ppm to 2.107 ppm. Table 3-2 summarizes the data which were plotted in Figure 3-7.

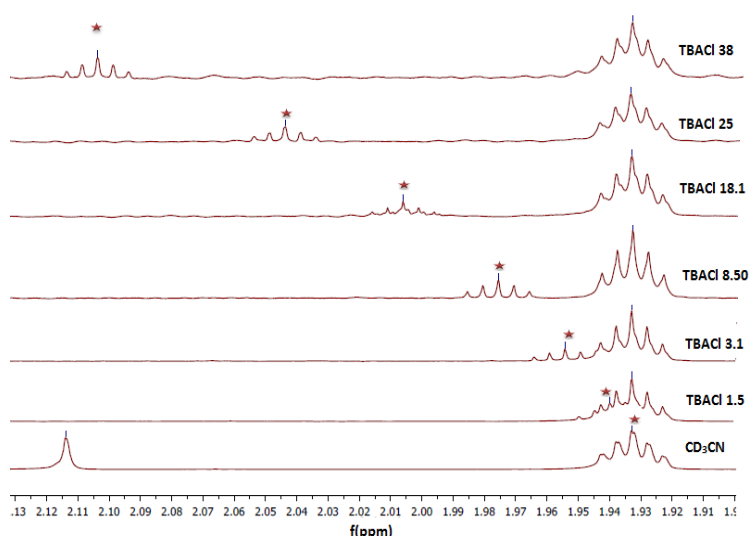


**Figure 3-6.**  $^1H$  NMR (500 MHz) expanded titration spectra for the residual proton signal of the  $CD_3CN$  solvent with increasing amounts of TBACl.

**Table 3-2.**  $^1\text{H}$  NMR (500 MHz) titration data in  $\text{CD}_3\text{CN}$ .

Moles of TBACl	[TBACl]	$\text{CD}_3\text{CN}$ $\delta(\text{ppm})$	$\Delta\delta(\text{Hz})$
0	0	1.933	0
5.40E-06	5.40E-03	1.940	3.5
1.08E-05	1.08E-02	1.954	10.5
3.06E-05	3.06E-02	1.976	21.5
6.51E-05	6.51E-02	2.007	37
9.00E-05	9.00E-02	2.045	56
1.37E-04	1.37E-01	2.107	87

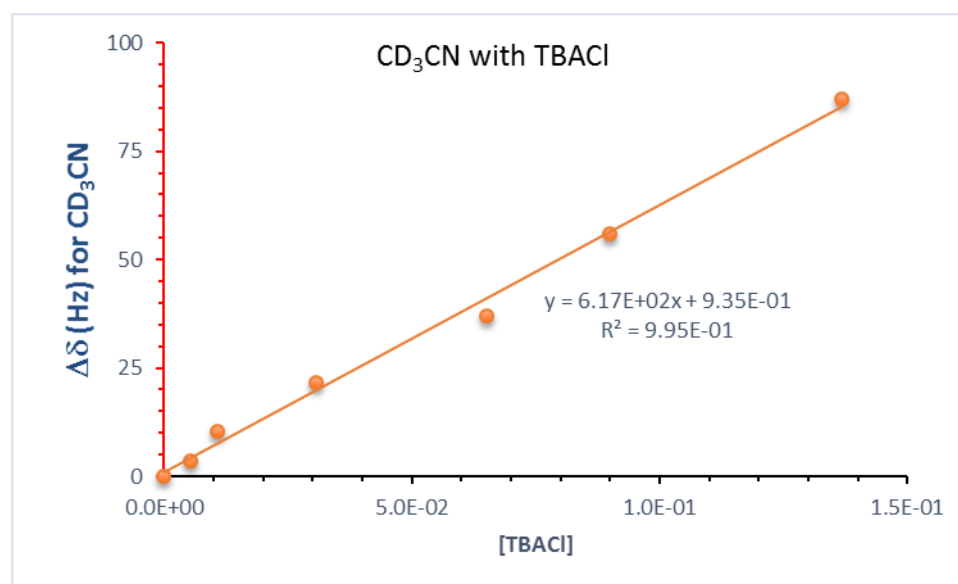


**Figure 3-7.** Least-squares linear regression plot for the  $\text{CD}_3\text{CN}$ : TBACl data.

### 3.3.3 Titration of TBACl in $\text{DMSO}-d_6$

Figure 3-8 shows the titration spectra for TBACl in  $\text{DMSO}-d_6$ . Increasing the added amounts of TBACl to the  $\text{DMSO}-d_6$  results in upfield chemical shift changes for

the residual proton signal of DMSO- $d_6$  from 2.50 ppm to 2.40 ppm. Table 3-3 summarizes the data which were plotted in Figure 3-9.

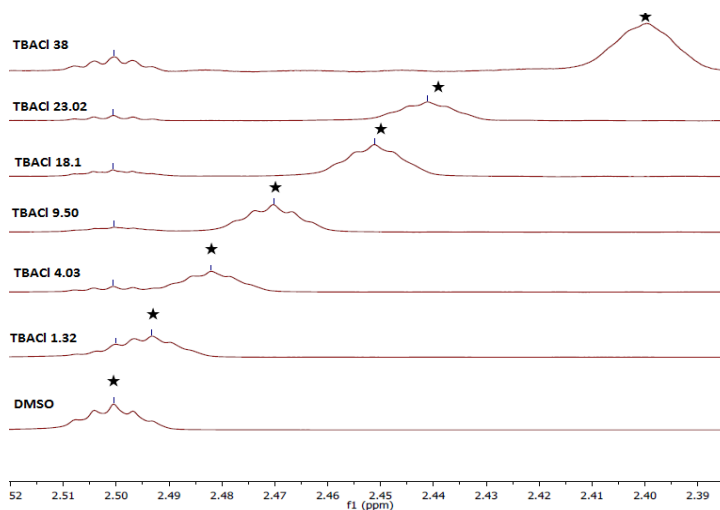


**Figure 3-8.**  $^1\text{H}$  NMR (500 MHz) expanded titration spectra for the residual proton signal of the DMSO- $d_6$  solvent with increasing amounts of TBACl.

**Table 3-3.**  $^1\text{H}$  NMR (300 MHz) titration data in DMSO- $d_6$ .

Sample	TBACl (g)	Moles of TBACl	[TBACl]	DMSO- $d_6$ $\delta$ (ppm)	$\Delta\delta$ (Hz)
		0	0	2.50	0.0
1	1.30E-03	4.68E-06	4.68E-03	2.493	0.6
2	4.00E-03	1.44E-05	1.44E-02	2.482	3.9
3	9.50E-03	3.42E-05	3.42E-02	2.47	7.5
4	1.81E-02	6.51E-05	6.51E-02	2.452	12.9
5	2.30E-02	8.28E-05	8.28E-02	2.441	16.2
6	3.80E-02	1.37E-04	1.37E-01	2.4	28.5

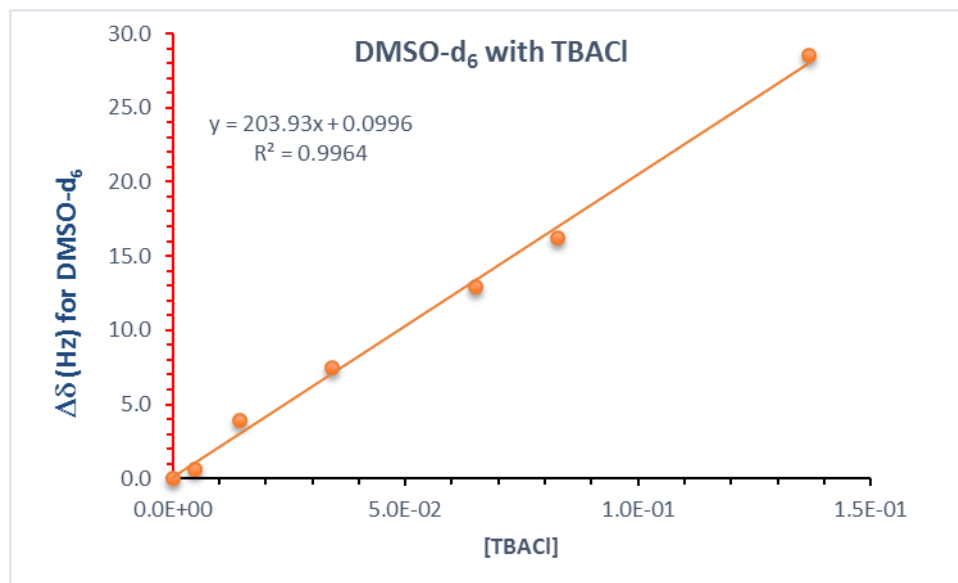


**Figure 3-9.** Least-squares linear regression plot for the DMSO: TBACl data.

### 3.2.4 Titration of TBACl in Methanol- $d_4$ ( $CD_3OD$ )

As previously noted, Figure 3-10 shows that increasing the added amount of TBACl to the  $CD_3OD$  results in up-field chemical shift changes, as can be seen, for the residual proton signal of  $CD_3OD$  from 4.833 ppm to 4.690 ppm. The complexation that occurred between TBACl and  $CD_3OD$  is indicated in the Table 3-4. The least-squares linear regression plot for the  $CD_3OD$ : TBACl data is shown in Figure 3-11.

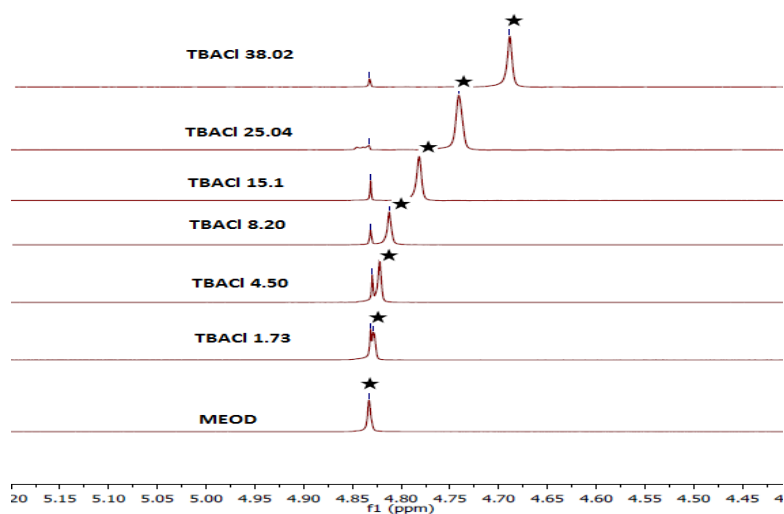


**Figure 3-10.**  $^1\text{H}$  NMR (500 MHz) expanded titration spectra for the residual proton signal of the  $\text{CD}_3\text{OD}$  solvent with increasing amounts of TBACl.

**Table 3-4.**  $^1\text{H}$  NMR (500 MHz) titration data in  $\text{CD}_3\text{OD}$ .

Sample	TBACl (g)	Moles of TBACl	[TBACl]	$\text{CD}_3\text{OD}$ $\delta$ (ppm)	$\Delta\delta$ (Hz)
		0	0	4.833	0
1	1.73E-03	6.22E-06	6.22E-03	4.829	2
2	4.50E-03	1.62E-05	1.62E-02	4.825	4
3	8.20E-03	2.95E-05	2.95E-02	4.814	9.5
4	1.51E-02	5.43E-05	5.43E-02	4.784	24.5
5	2.50E-02	9.00E-05	9.00E-02	4.739	47
6	3.80E-02	1.37E-04	1.37E-01	4.69	71.5

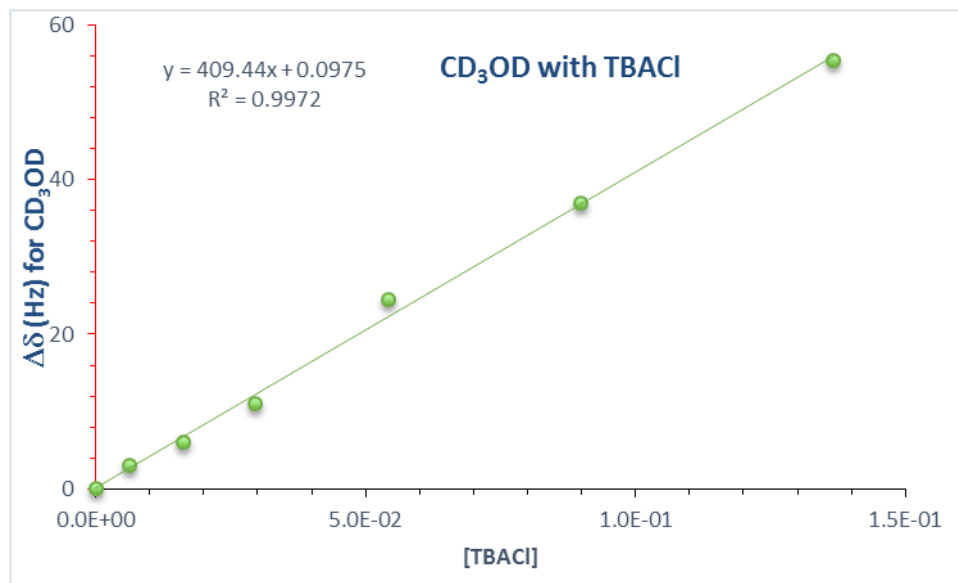


**Figure 3-11.** Least-squares linear regression plot for the CD<sub>3</sub>OD: TBACl data.

### 3.3.5 Titration of TBACl in DCM-*d*<sub>2</sub>

Figure 3-12 shows the titration spectra for TBACl in dichloromethane (DCM-*d*<sub>2</sub>) in which the down-field chemical shift changes from 5.316 ppm to 5.397 ppm can be seen for the residual proton signal of CD<sub>2</sub>Cl<sub>2</sub>. Table 3-5 summarizes the data which were plotted in Figure 3-13.

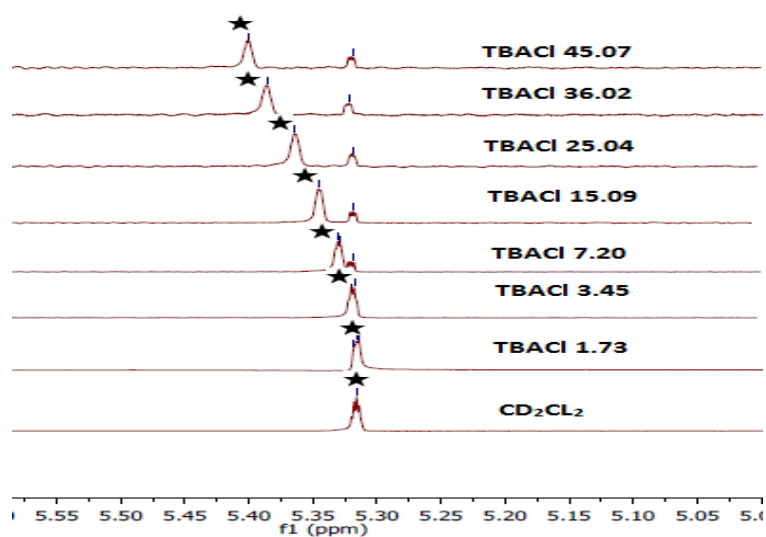


**Figure 3-12.**  $^1\text{H}$  NMR (500 MHz) expanded titration spectra for the residual proton signal of the  $\text{DCM-}d_2$  solvent with increasing amounts of TBACl.

**Table 3-5.**  $^1\text{H}$  NMR (500 MHz) titration data in  $\text{DCM-}d_2$ .

Sample	TBACl (g)	Moles of TBACl	[TBACl]	$\text{DCM-}d_2$ $\delta(\text{ppm})$	$\Delta\delta(\text{Hz})$
	0	0	0	5.316	0
<b>1</b>	1.73E-03	6.22E-06	6.22E-03	5.319	1.5
<b>2</b>	3.45E-03	1.24E-05	1.24E-02	5.321	2.5
<b>3</b>	7.20E-03	2.59E-05	2.59E-02	5.329	6.5
<b>4</b>	1.51E-02	5.43E-05	5.43E-02	5.345	14.5
<b>5</b>	2.50E-02	9.00E-05	9.00E-02	5.362	23
<b>6</b>	3.60E-02	1.30E-04	1.30E-01	5.381	32.5
<b>7</b>	4.51E-02	1.62E-04	1.62E-01	5.397	40.5

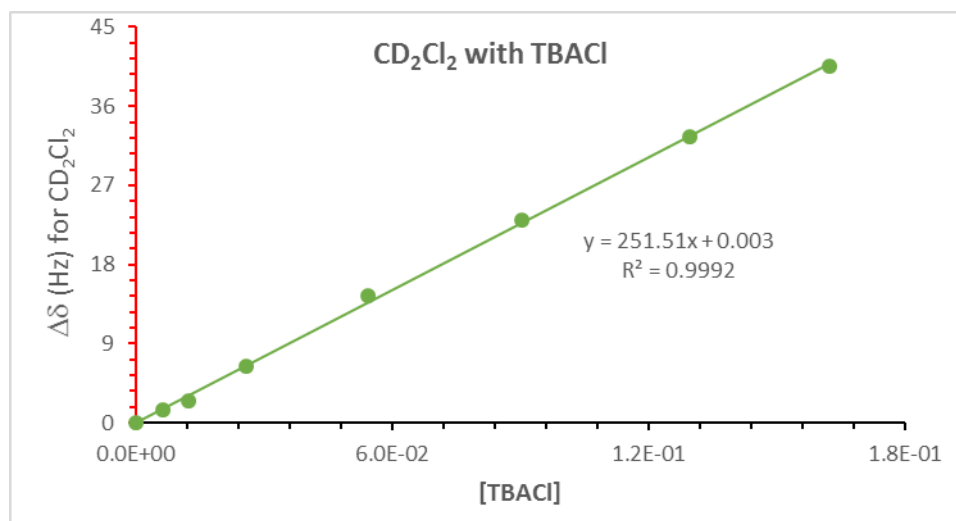


**Figure 3-13.** Least-squares linear regression plot for the DCM-*d*<sub>2</sub>: TBACl data.

### 3.3.6 Titration of TBABr in acetone-*d*<sub>6</sub>

A complexation study between TBABr and acetone-*d*<sub>6</sub> was conducted to test whether TBABr behaved in a manner similar to that seen in the Sleem et al. study. The value of the slope measured for TBABr in the CDCl<sub>3</sub> solutions was smaller than that seen for the TBACl in their study. The result obtained in the present study, albeit with acetone-*d*<sub>6</sub>, was found to be basically similar to Sleem's observations. The observed chemical shifts ( $\Delta\delta$  Hz) for the residual proton signal of the (CD<sub>3</sub>)<sub>2</sub>CO solvent were plotted against the molar concentrations of the TBABr in the (CD<sub>3</sub>)<sub>2</sub>CO solutions. Figure 3-14 shows the slope of 492 obtained from the least-squares linear regression plots for the TBABr in (CD<sub>3</sub>)<sub>2</sub>CO, compared with that from the TBACl study which was 677.

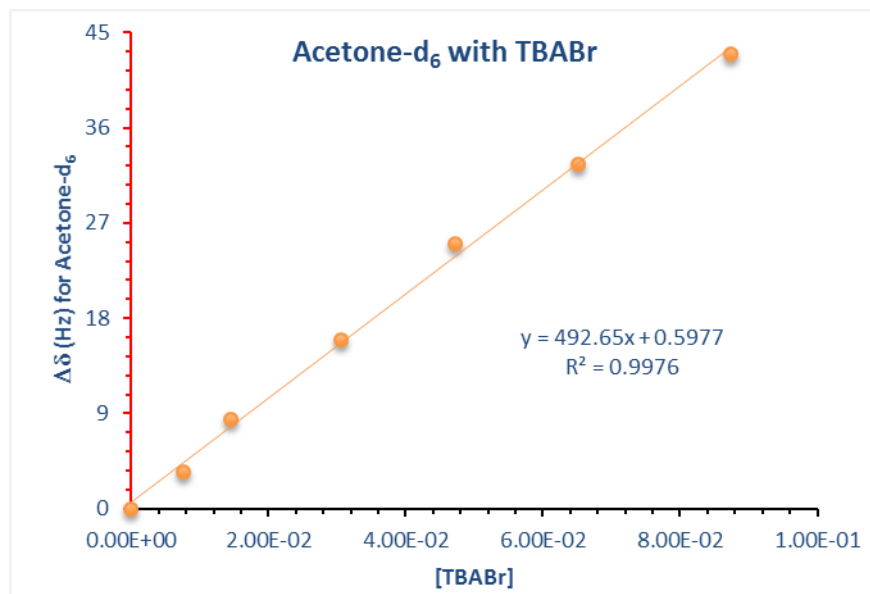


**Figure 3-14.** Least-squares linear regression plot for the  $(\text{CD}_3)_2\text{CO}:\text{TBABr}$  data.

Figure 3-15 shows the titration spectra for TBABr with  $(\text{CD}_3)_2\text{CO}$ . Increasing the amount of TBABr added to the solvent results in up-field chemical shift changes for the residual proton signal of the deuterioacetone from 2.059 ppm to 1.973 ppm. Table 3-6 summarizes the data which were plotted in Figure 3-14.

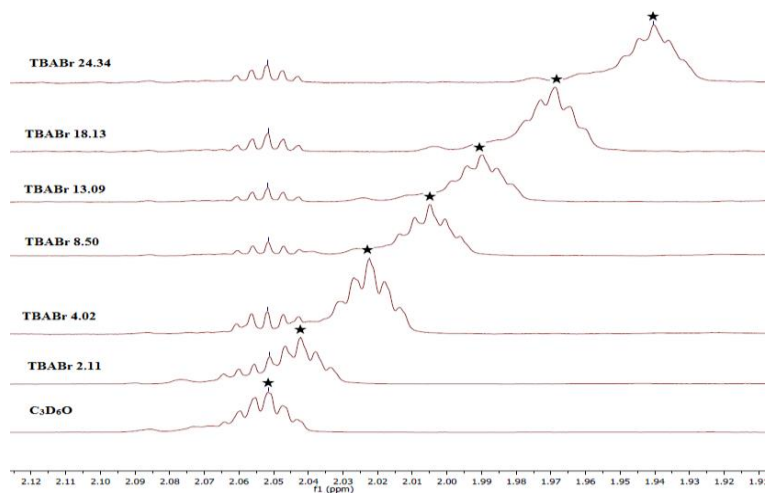


**Figure 3-15.**  $^1\text{H}$  NMR (500 MHz) expanded titration spectra for the residual proton signal of the  $(\text{CD}_3)_2\text{CO}$  solvent with increasing amounts of TBABr.

**Table 3-6.**  $^1\text{H}$  NMR (500 MHz) titration data for  $(\text{CD}_3)_2\text{CO}$ .

Sample	TBABr (g)	Moles of TBABr	[TBABr]	$(\text{CD}_3)_2\text{CO}$ (ppm)	$\Delta\delta(\text{Hz})$
	0	0	0	2.059	0
1	2.11E-03	7.59E-06	7.59E-03	2.052	3.5
2	4.02E-03	1.44E-05	1.44E-02	2.042	8.5
3	8.50E-03	3.06E-05	3.06E-02	2.027	16
4	1.31E-02	4.68E-05	4.68E-02	2.009	25
5	1.81E-02	6.48E-05	6.48E-02	1.994	32.5
6	2.43E-02	8.64E-05	8.64E-02	1.973	43

### 3.4. Conclusion and Summary

The values of the slopes measured for the five different solutions with TBACl salts are summarized in Figure 3-16. The differences between the values could be attributed to several factors. First, there are the obvious differences in the dielectric constants of the solvents, though these were not determined. Secondly, the addition of

halide to the fixed amount of the solvent results in an increased complexation. This is because the mode of complexation is presumed to be *via* hydrogen-bonding between the halide ions and the residual protons in the solvents. However, a “binding constant” could not be determined since a true saturation between the “guest” (i.e. the TBAX salt) and the solvent could not be reached.

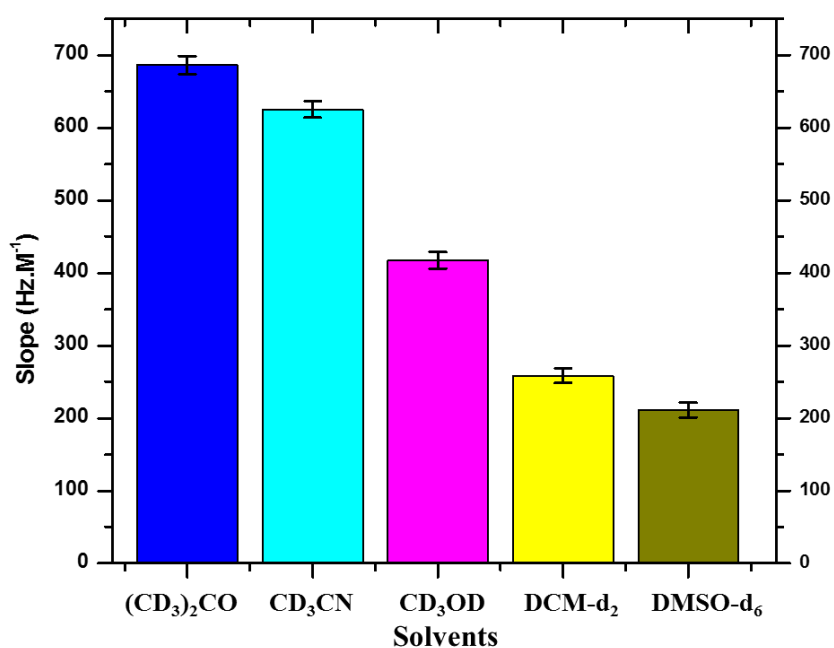


**Figure 3-16.** Histogram showing the slope values (absolute values) obtained from the addition of TBACl to the different deuterated solvents determined by <sup>1</sup>H NMR titration experiments. Each column represents the average slope obtained from duplicate experiments, with the corresponding standard deviation shown by error bars.

### 3.5 References

1. Sleem, H. F.; Dawe, L. N.; Georghiou, P. E. *New J. Chem.* **2012**, *36*, 2451–2455.
2. Späth, A.; König, B. *Beilstein J. Org. Chem.* **2010**, *6* No. 32, 1-111.
3. Asfari, Z.; Böhmer, V.; Harrowfield, J.; Vicens, J. *Calixarenes 2001*; Kluwer Academic Press: Dordrecht, 2001.
4. Fielding, L. *Tetrahedron* **2000**, *56*, 6151–6170.
5. Nam, K. C.; Kang, S. O.; Ko, S. W. *Bull. Korean Chem. Soc.* **1999**, *20*, 953–956.
6. Green, R. D.; Martin, J. S. *J. Am. Chem. Soc.* **1968**, *90*, 3659–3668.
7. Sleem, H. F. *Synthesis of New Macrocyclic Polyamids and Polysulfonamids and a Study of their Complexation behavior using H-NMR and Mass Spectroscopy*. Ph.D. Dissertation, Memorial University, 2013.
8. Pimentel, G. C.; McClellan, A. L. *The Hydrogen Bond* W. H. Freeman, San Francisco, California, 1960.
9. Allerhand, A.; Schleyer, P. v. R. *J. Am. Chem. Soc.* **1963**, *85*, 1715–1725.
10. Buckingham, A. D. *Can. J. Chem.* **1960**, *38*, 430–439.
11. Sleem, H. F.; Dawe, L. N.; Georghiou, P. E. *Tetrahedron Lett.* **2013**, *54*, 3444–3448.
12. Sleem, H. F.; Dawe, L. N.; Rahman, S.; Georghiou, P. E. *Supramol. Chem.* **2014**, *26*, 579–582.

## Chapter 4

### Naphthalene-Appended Triazole-Based Calix[4]arene Cavities

#### as Fluorescent Chemosensors for Fe<sup>3+</sup>

#### 4.1 Introduction

There have been extensive studies conducted on the use of calixarene-based devices as highly selective and sensitive chemosensors. Calixarenes offer several advantages over other molecular systems. These advantages include relatively easy functionalization at their lower and upper rims, the presence of a hydrophobic cavity, and the existence of a flexible core/scaffold that can be modified for targeted substrate binding.<sup>1</sup> The functionalization of calixarenes with azide-bearing triazole groups has recently been achieved through the “click” or copper-assisted azide cycloaddition (CuAAC) reaction of alkynyl calixarenes with azide-bearing fluorophores.<sup>2-5</sup> The nitrogen atoms of the triazole groups form a binding pocket with the calixarene oxygen atoms thus making such triazole-calixarenes effective cation receptor molecules. The synthesis and design of triazole-bridged calix[4]arenes receptors for metal ions is therefore of significant interest in supramolecular chemistry. This is due to the diverse roles that metal ions play in chemical processes, in biology, and in the environment.<sup>6,7</sup> Iron plays an essential role where, as a transition metal, it has the important function of carrying oxygen in heme molecules and also as a cofactor in enzymatic reactions of the mitochondrial respiratory chain.<sup>7</sup>

#### 4.1.1 The copper(I)-catalyzed alkyne-azide cycloaddition (CuAAC)

A powerful synthetic tool for the construction of macrocyclic molecules, which has emerged recently, is the CuAAC or “click” reaction. Some of the reasons for the increased popularity of this reaction include its high efficiency, mild reaction conditions, and tolerance for sensitive functional groups. 1,2,3-Triazoles, which are products of the CuAAC reaction, are a group of heterocycles that have interesting properties such as good aromatic character, large dipole moments (5D),<sup>8</sup> the ability to engage in  $\pi$ -stacking interactions,<sup>9</sup> and have excellent neutral C-H hydrogen-bonding capability. In addition, the triazoles have high chemical stability since they are inert to acidic and basic conditions as well as to oxidative and reductive conditions. These properties allow triazoles to be suitable for applications in different fields of supramolecular chemistry including protein chemistry, carbohydrate chemistry and as synthetic receptors and molecular machines. In addition, triazole-based compounds are used in medicinal chemistry as antiasthmatic,<sup>10</sup> antiviral, antibacterial,<sup>11</sup> and antiallergic drugs.<sup>12</sup>

In their 2005 study, Ryu and Zhao<sup>13</sup> became among the first to use the CuAAC synthetic method in a calixarene moiety to produce the 1,2,3-triazole based calix[4]arenes **1a-c** shown in Figure 4-1. In this study, the lower-rim terminal alkyne-bearing calix[4]arene was used as a scaffold upon which the 1,2,3-triazole functional group was generated. The generated functional group was then capable of binding to different metal cations *via* non-covalent interactions.

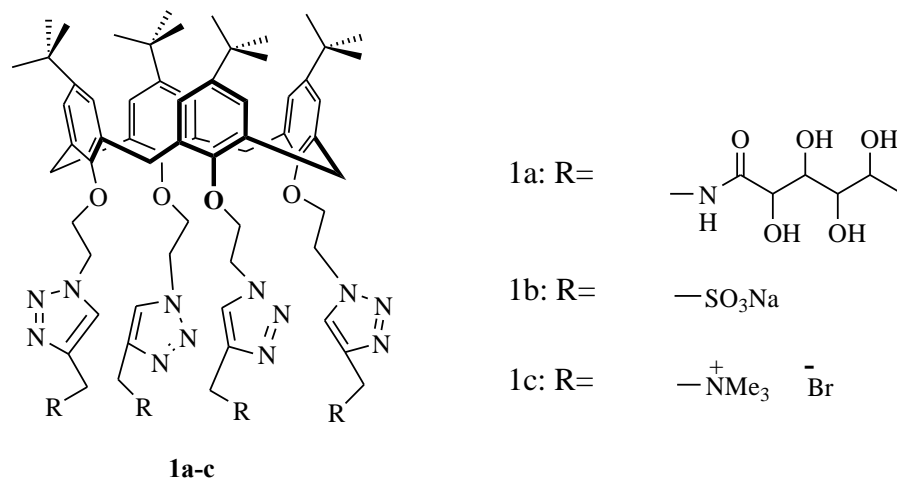


**Figure 4-1.** Triazole-bridge based calix[4]arenes **1a-c**.

## 4.1.2 Triazole-bridge based calixarene chemosensors

### 4.1.2.1 Metal ions receptor

Chung and colleagues conducted a study utilizing click chemistry on calixarene frameworks for constructing metal ion sensors.<sup>14</sup> Figure 4-2 shows the structure of the bimodal compound **2** which they obtained through the coupling of the anthracene units onto a *1,3-alternate* calix[4]crown-5 scaffold thus creating two possible metal binding sites: (1) between the triazole units and the calixarene phenolic group; and (2) within the crown ether moiety on the opposite face. There was limited selectivity for  $\text{Pb}^{2+}$  observed in  $\text{MeCN}/\text{CHCl}_3$  in the study. The fluorescence of the anthracene groups was quenched by  $\text{Hg}^{2+}$ ,  $\text{Cu}^{2+}$ ,  $\text{Cr}^{3+}$  and  $\text{Pb}^{2+}$  while  $\text{K}^+$ ,  $\text{Ba}^{2+}$  and  $\text{Zn}^{2+}$  enhanced it. An interesting observation in the study was that  $\text{K}^+$  addition to the  $\text{Pb}^{2+}$  complex resulted in almost the complete revival of the fluorescence emission while the addition of  $\text{Pb}^{2+}$  to the  $\text{K}^+$  complex resulted in quenching. Compound **2** therefore is an example of a metal-ion switchable chemosensor, and that the  $\text{K}^+$  and  $\text{Pb}^{2+}$  are the "on" and "off" switches

respectively.  $^1\text{H}$  NMR studies have shown that  $\text{K}^+$  binds to the crown ether while  $\text{Pb}^{2+}$  binds to the triazole binding pocket, with the metal exchange being caused by electrostatic repulsion as well as any allosteric effects.

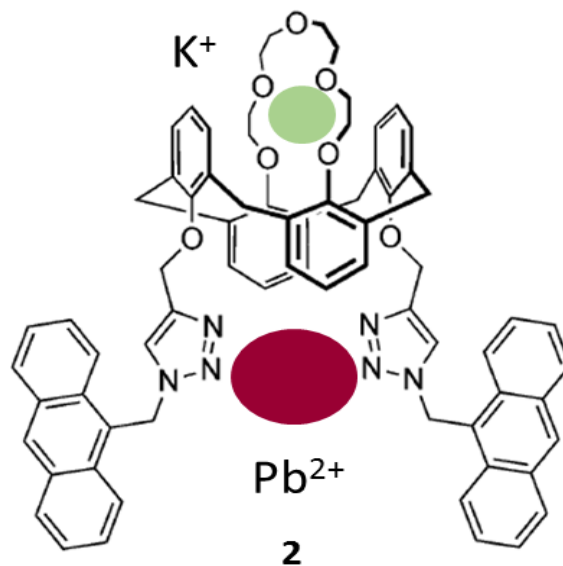


**Figure 4-2.** Triazole-modified calix[4]crown as a novel fluorescent on-off switchable chemosensor.

Figure 4-3 shows the structure of **3**, a triazole-modified calix[4]arene which is another example of a metal ion receptor which has two potential binding sites. In this case, they situated on the same lower rim substituent groups of the calix[4]arene which is in a *cone* conformer. The first binding site is a bis-triazole binding pocket while the second site consists of two Schiff base groups that also contain hydroxymethyl groups.<sup>15</sup> Compound **3** was shown to be an extremely sensitive sensor for  $\text{Zn}^{2+}$  and was selective for  $\text{Zn}^{2+}$  over a range of divalent metal ions, including  $\text{Cd}^{2+}$ , as well as responding with a 65-fold increase in fluorescence in MeOH and slightly less in aqueous organic solutions. Although compound **3** has two potential binding sites, an analysis using a Job plot

showed that there was 1:1 stoichiometry, with the  $^1\text{H}$  NMR studies showing that  $\text{Zn}^{2+}$  binds only at the Schiff base site. Moreover, an analogue without the hydroxyl and imino groups showed no absorbance or fluorescence changes when  $\text{Zn}^{2+}$  was added. This observation confirmed that, perhaps surprisingly, the triazoles play only an exclusively structural role in this sensor.

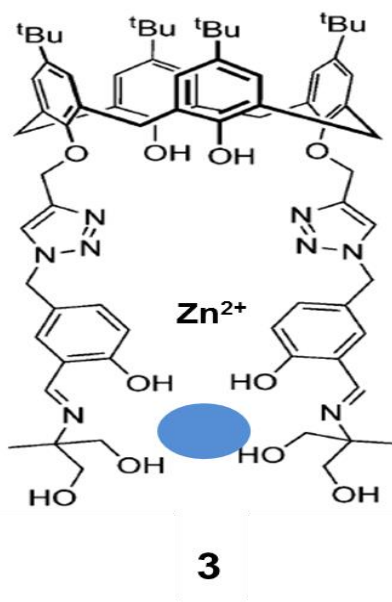


**Figure 4-3.** Salicylaldehyde appended triazole-linked calix[4]arene.

#### 4.1.2.2 Anion receptors

Various donors of hydrogen bonds such as ammonium groups,<sup>16</sup> ureas,<sup>17</sup> amides,<sup>18</sup> guanidiniums,<sup>19</sup> and polypyrroles<sup>20</sup> have been used to recognize anions based upon the N-H groups. The CuAAC click reaction offers an effective tool for synthesizing receptors that incorporate C-H hydrogen-bond donors in the form of the triazole group.<sup>21,22</sup>

For example, Flood et al. used CuAAC reactions to synthesize the aryl-triazole shown in Figure 4-4. In this receptor, the backbone is pre-organized by intramolecular

hydrogen bonds formed between the two *meta*-amide groups on the central aromatic ring and the triazole N atoms. This receptor showed high binding constants in the range of  $10^5$  -  $10^3$  with tetra-*n*-butylammonium halides in the order:  $\text{Cl}^- > \text{Br}^- > \text{I}^-$ .<sup>23</sup>

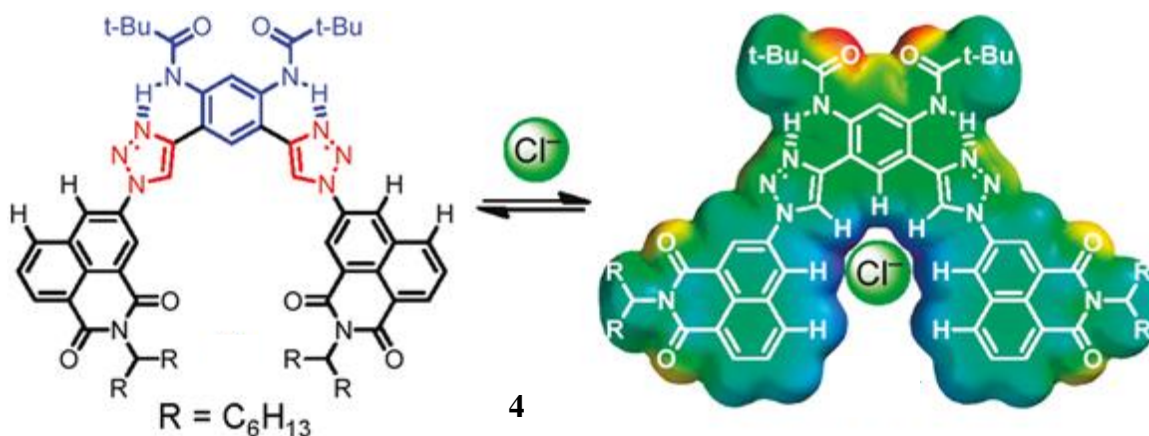
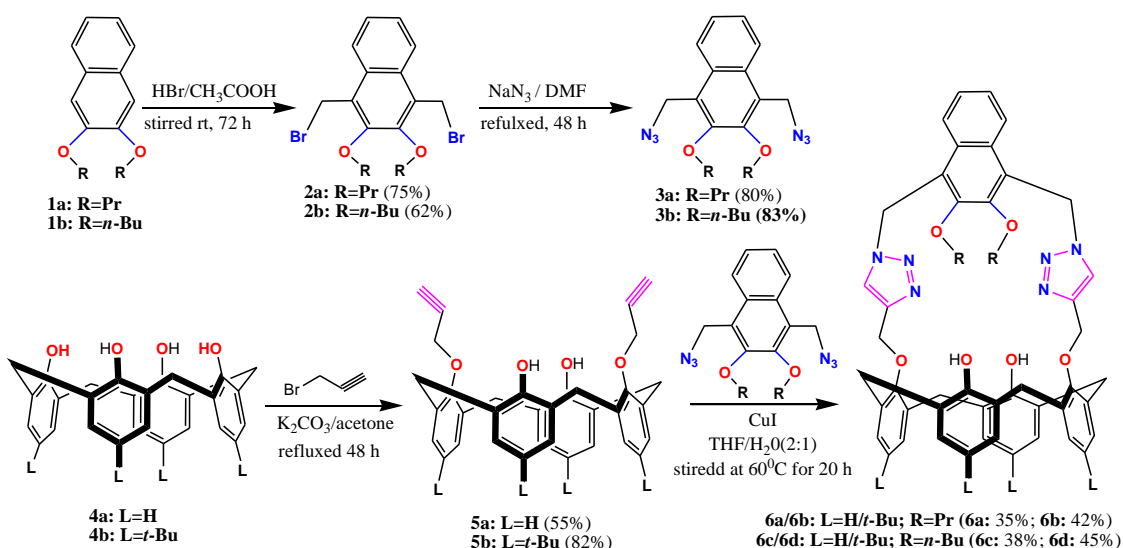


**Figure 4-4.** An aryl-triazole receptor capable of strong chloride binding. [Adapted with permission from Reference 23]

## 4.2 Objectives of the work reported in this Chapter

Using the click or CuAAC methodology with 1,3-bis-alkyne-calix[4]arenes **5a** and **5b**, receptors **6a-6d** were synthesized by coupling with the corresponding 1,4-bis-naphthyl-azide derivatives (Scheme 1). The starting materials, de-*tert*-butylcalix[4]arene **8a**,<sup>24a</sup> *p-tert*-butylcalix[4]arene **8b**,<sup>24b</sup> *p-tert*-butyl-25,27-bis(propargyl)-calix[4]arene **9b**<sup>25</sup> and 25,27-dihydroxy-1,3-bis(*O*-propargyl)calix[4]arene **9a**<sup>24c</sup> were synthesized by modified literature procedures. 1,4-bis-naphthyl-azide derivatives **7a/7b** were synthesized from **10a/b** via **11a/b** according to the literature procedure.<sup>26</sup> The syntheses of all of the calixarenes employed in the study reported herein were conducted by Dr. Shofiur Rahman in the Georghiou labs. The metal ion receptor properties of **6a-6d** were carried

out both by fluorescence emission and  $^1\text{H}$  NMR spectroscopy, To better understand the binding properties of receptors **6a** and **6c** with  $\text{Fe}^{3+}$ ,  $\text{Hg}^{2+}$  and  $\text{Cu}^{2+}$  ions a computation study was carried out. The individual structures for all studies in the gas-phase were fully geometry-optimized using Gaussian 09<sup>27</sup> with the B3LYP level of DFT and the lan12dz basis set.



**Scheme 4.1.** Synthesis of triazolyl-bridged naphthylcalix[4]arenes **6a-6d**.

## 4.3 Complexation studies

### 4.3.1 Experimental section

UV-Visible spectra were recorded on an Agilent 8543 Diode Array Spectrophotometer interfaced to an HP computer. Data manipulations were conducted using software supplied by the manufacturer. Spectroscopic experiments were conducted

using 1 cm sealed quartz fluorescence cuvettes. Emission spectra were measured on a Photon Technology International (PTI) Quanta master 6000 spectrofluorometer equipped with a continuous xenon arc lamp as the excitation source. The emitting light was collected at 90° to the excitation beam and detected by a Hamamatsu R-928 photomultiplier tube (PMT) in photon counting mode. All emission spectra were corrected for instrumental light loss using correction factors supplied by PTI. All the metal ion salts were received from Alfa Aesar in >99 % purity and were used as supplied. High-purity spectral grade CHCl<sub>3</sub> and CH<sub>3</sub>CN were purchased from Cambridge Isotope Laboratories. In a typical experiment, solutions of **6a-6d** in CHCl<sub>3</sub>:CH<sub>3</sub>CN (1:9) were prepared by gravimetric methods for each individual experiment. The concentrations of **6a-6d** were  $\sim 1.64 \times 10^{-5}$  M for the titrations experiments. Stock solutions of individual metal salts were also prepared by gravimetric methods, in CHCl<sub>3</sub>:CH<sub>3</sub>CN (1:9). Compounds **6a-6d** were dissolved first in CH<sub>3</sub>Cl and then diluted with CH<sub>3</sub>CN to achieve efficient solubilization. The concentration of each stock solution was different and was set according to its response towards the sensor observed in the preliminary experiments. Metal salts were dissolved first in CH<sub>3</sub>CN and then diluted in CHCl<sub>3</sub> to achieve efficient solubilization. After acquiring the absorption and emission spectra of **6a-6d**, solutions of the respective metal salts were added using a micro-syringe (Hamilton). Addition of aliquots of metal salts in CHCl<sub>3</sub>:CH<sub>3</sub>CN (1:9) resulted in spectral changes in the emission spectra which were assigned to sequential binding reactions of **6a-6d** with the metal ions.

### 4.3.2 Complexation studies using fluorescence spectroscopy

#### 4.3.2.1 Calculation of association constants:

The association constants ( $K$ ) determined for the complexation between hosts **6a-d** and the metal ions examined were based on the fluorescence data and were calculated employing a modified Bensi-Hildebrand<sup>28</sup> method using equations 1:

$$\frac{1}{(F_o - F)} = \frac{1}{(F_o - F_{fc})} + \frac{1}{K(F_o - F_{fc})[M]} \quad (1)$$

In these equations,  $K$  is the association constant,  $F_o$  is the fluorescence intensity of the free host,  $F$  is the observed fluorescence intensity of the host-guest complex, and  $F_{fc}$  is the fluorescence intensity upon saturation.  $[M]$  is the concentration of the guest ion in molL<sup>-1</sup>. According to these equations, a plot of  $1/(F_o - F)$  vs  $1/[M]$  giving a straight line indicates 1:1 stoichiometry between the host and metal ions. In the titrations conducted during the present study, all of the plots showed clear linear relationships using equation (1), with correlation coefficients  $> 0.993$ . The 1:1 binding constants were obtained from equation (2):

$$K = (\text{y-intercept}) / (\text{slope}) \quad (2)$$

Note:  $[M]$  have in the B-H approach assumes that it is  $[M] + [M]_{\text{complex}}$ .

#### 4.3.2.2 Fluorescence complexation studies for 6a-6d with metal ions

Dilute stock solutions of **6a-6d** ( $1.50 \times 10^{-5}$  M) were prepared in a 9:1 CH<sub>3</sub>CN:CHCl<sub>3</sub> mixed solvent and these receptors displayed monomer emissions at 352 nm at 291 nm excitation wavelength. The fluorescence emissions were quenched upon

adding the metal ions as a result of complexation occurring between each of the host receptor molecules and the metal ion guest. The cationic guests that were investigated were:  $\text{Na}^+$ ,  $\text{K}^+$ ,  $\text{Ca}^{2+}$ ,  $\text{Ba}^{2+}$ ,  $\text{Mg}^{2+}$ ,  $\text{Sr}^{2+}$ ,  $\text{Ag}^+$ ,  $\text{Co}^{2+}$ ,  $\text{Cd}^{2+}$ ,  $\text{Fe}^{2+}$ ,  $\text{Fe}^{3+}$ ,  $\text{Cu}^{2+}$ ,  $\text{Hg}^{2+}$ ,  $\text{Pd}^{2+}$ ,  $\text{Zn}^{2+}$ ,  $\text{Ni}^{2+}$  and  $\text{Mn}^{2+}$  ions, all of which were used as their respective perchlorate salts in aqueous solution. The fluorescence spectroscopy (FS) studies showed that **6a-6d** selectively recognized  $\text{Fe}^{3+}$  ions. Association constants were calculated using the Benesi-Hildebrand equations for these cationic guests and gave the highest values namely,  $1.96 \times 10^5 \text{ M}^{-1}$  for the **6a**: $\text{Fe}^{3+}$ ,  $1.38 \times 10^5 \text{ M}^{-1}$  for the **6b**: $\text{Fe}^{3+}$ ,  $1.22 \times 10^5 \text{ M}^{-1}$  for the **6c**: $\text{Fe}^{3+}$  and  $1.02 \times 10^5 \text{ M}^{-1}$  for the **6d**: $\text{Fe}^{3+}$  complexes. Figures 4-5 to 4-8 show the FS titration experiments conducted for the receptors **6a-6d** with  $\text{Fe}^{3+}$  ions. The highest association constant values with the macrocycles were obtained with  $\text{Fe}^{3+}$ ,  $\text{Cu}^{2+}$  and  $\text{Hg}^{2+}$ .

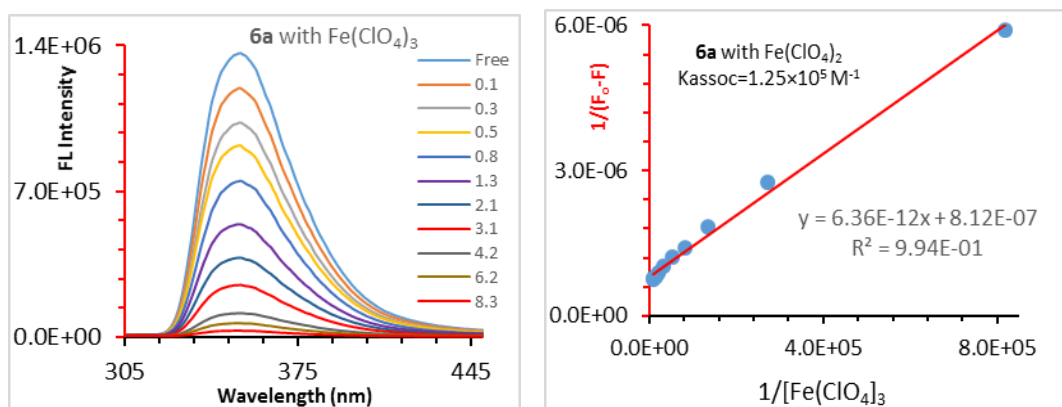


**Figure 4-5.** Left: Fluorescence spectra of **6a** (1.50  $\mu\text{M}$ ) upon addition of  $\text{Fe}^{3+}$  in acetonitrile/chloroform (v/v= 9:1) solutions.  $\lambda_{\text{ex}} = 291 \text{ nm}$ . Right: Benesi-Hildebrand plots of  $1/(F_0 - F)$  versus  $1/[\text{Fe}(\text{ClO}_4)_3]$  for **6a** upon titration with  $\text{Fe}^{3+}$  (0-8.3 equivalents). The association constants were calculated for the changes at the 352 nm wavelengths.

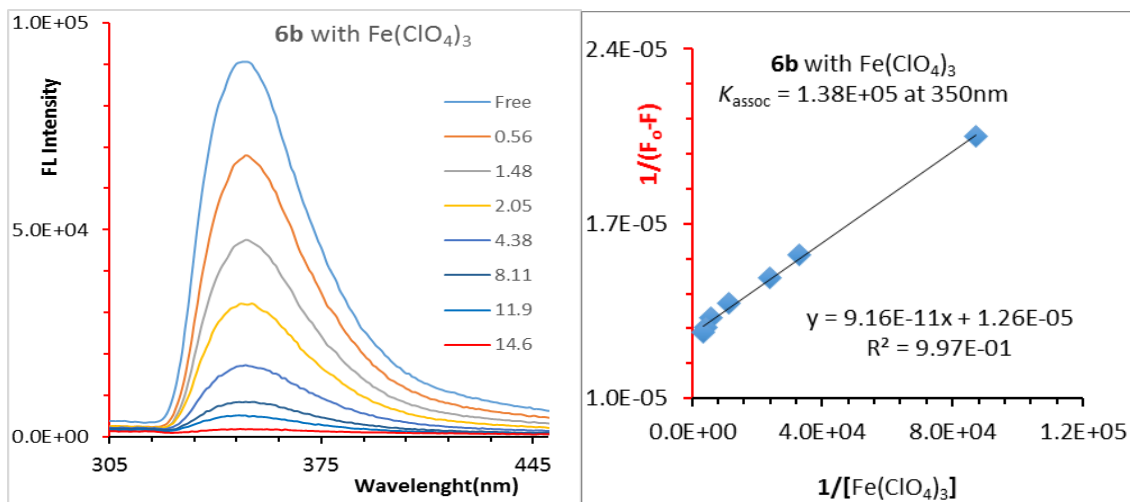


**Figure 4-6.** *Left:* Fluorescence spectra of **6b** (1.50  $\mu\text{M}$ ) upon addition of Fe<sup>3+</sup> in acetonitrile/chloroform (v/v= 9:1) solutions.  $\lambda_{\text{ex}} = 291$  nm. *Right:* Benesi-Hildebrand plots of  $1/(F_0-F)$  versus  $1/[\text{Fe}(\text{ClO}_4)_3]$  for **6b** upon titration with Fe<sup>3+</sup> (0-14.6 equivalents). The association constants were calculated for the changes at the 352 nm wavelengths.

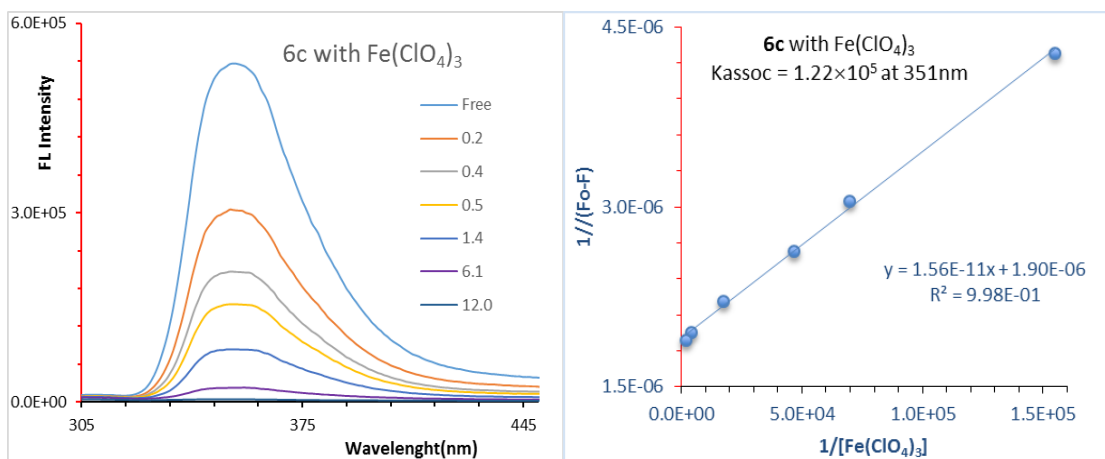


**Figure 4-7.** *Left:* Fluorescence spectra of **6c** (1.50  $\mu\text{M}$ ) upon addition of Fe<sup>3+</sup> in acetonitrile/chloroform (v/v= 9:1) solutions.  $\lambda_{\text{ex}} = 291$  nm. *Right:* Benesi-Hildebrand plots of  $1/(F_0-F)$  versus  $1/[\text{Fe}(\text{ClO}_4)_3]$  for **6c** upon titration with Fe<sup>3+</sup> (0-12 equivalents). The association constants were calculated for the changes at the 352 nm wavelengths.

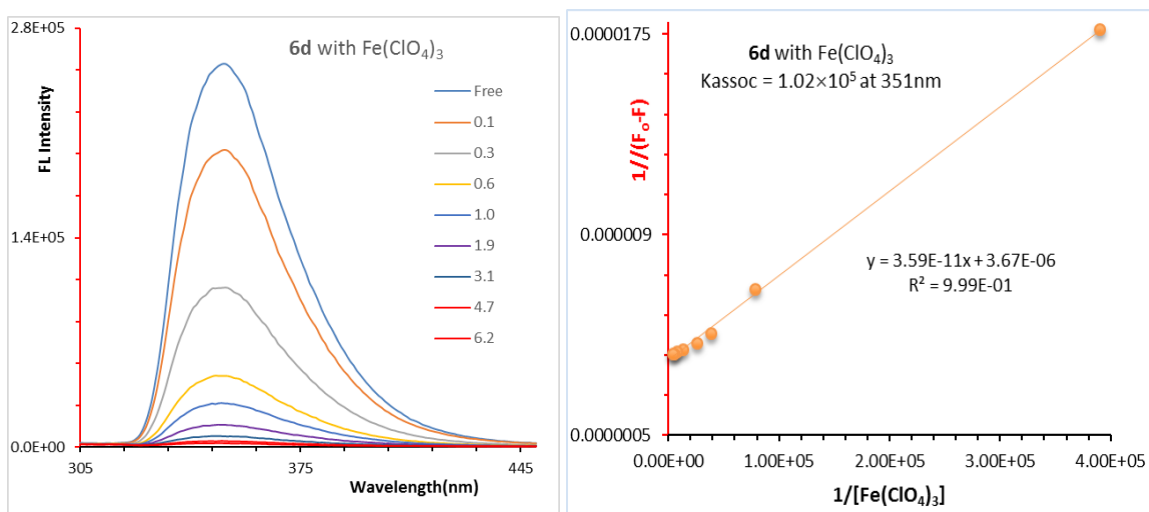


**Figure 4-8.** Left: Fluorescence spectra of **6d** (1.50  $\mu\text{M}$ ) upon addition of  $\text{Fe}^{3+}$  in acetonitrile/chloroform ( $v/v=9:1$ ) solutions.  $\lambda_{\text{ex}}=291$  nm. Right: Benesi-Hildebrand plots of  $1/(F_0-F)$  versus  $1/[\text{Fe}(\text{ClO}_4)_3]$  for **6d** upon titration with  $\text{Fe}^{3+}$  (0-6.2 equivalents). The association constants were calculated for the changes at the 352 nm wavelengths.

#### 4.3.2.3 Job plot analysis for **6a** and **6c** with $\text{Fe}^{3+}$

The titration data showed that 1:1 host-guest complexes were confirmed by Job plot analysis for **6a** and **6c** with  $\text{Fe}^{3+}$  and shown in Figure 4-9.

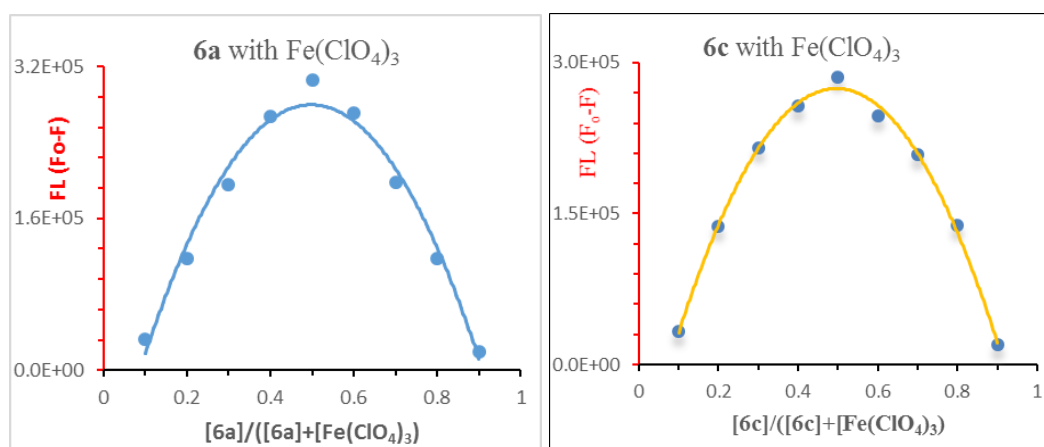


**Figure 4-9.** Job plot curves showing 1:1 complexation for **6a** and **6c** with  $\text{Fe}(\text{ClO}_4)_3$ .

#### 4.3.2.4 Fluorescence quenching of receptors 6a-6d with different metal ions

A comparison of the fluorescence quenching observed when each of the receptors **6a-6d** were titrated with the 17 different metal ions tested are shown in Figures 4-10 and 4-11. As can be seen in these figures, the greatest degree of quenching is found with  $\text{Fe}^{3+}$ ,  $\text{Hg}^{2+}$  and  $\text{Cu}^{2+}$ .

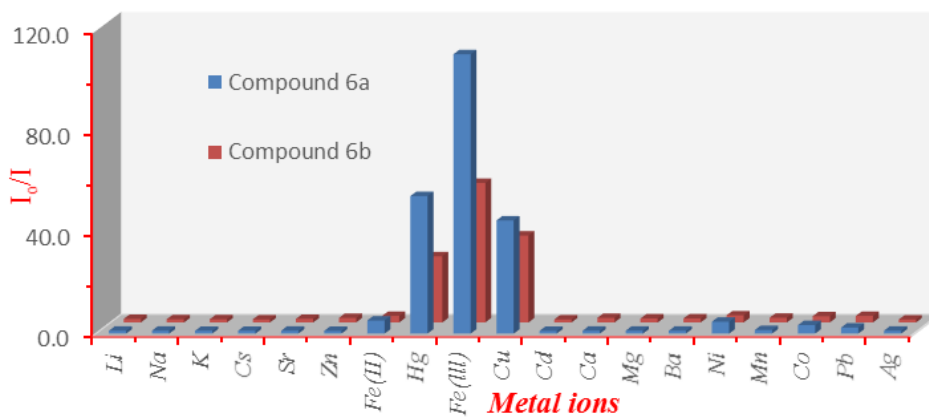


**Figure 4-5.** Histogram showing the fluorescence quenching of receptors **6a** (blue) and **6b** (red) with different metal ions.

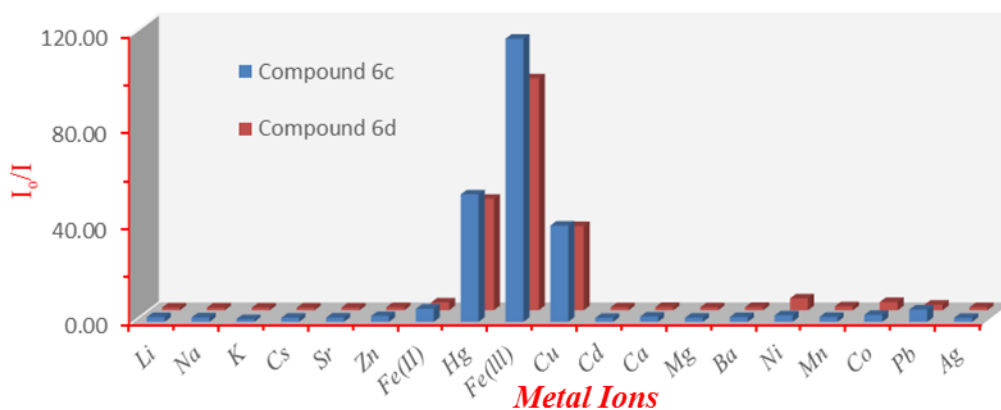


**Figure 4-11.** Histogram showing the fluorescence quenching of receptors **6c** (blue) and **6d** (red) with different metal ions.

#### 4.3.2.5 Comparison of the association constants of receptors 6a-6d with metal ions

Figures 4-12 and, 4-13 show the association constants determined for all of the complexes and it is clearly evident that the complexation of **6a**, **6b**, **6c** and **6d** with  $\text{Fe}^{3+}$  ions shows the largest  $K$  value of  $\sim 1.96 \times 10^5$ ,  $1.38 \times 10^5$ ,  $1.22 \times 10^5$  and  $1.02 \times 10^5 \text{ M}^{-1}$  based upon the changes in fluorescence intensity for receptors **6a-d** respectively.

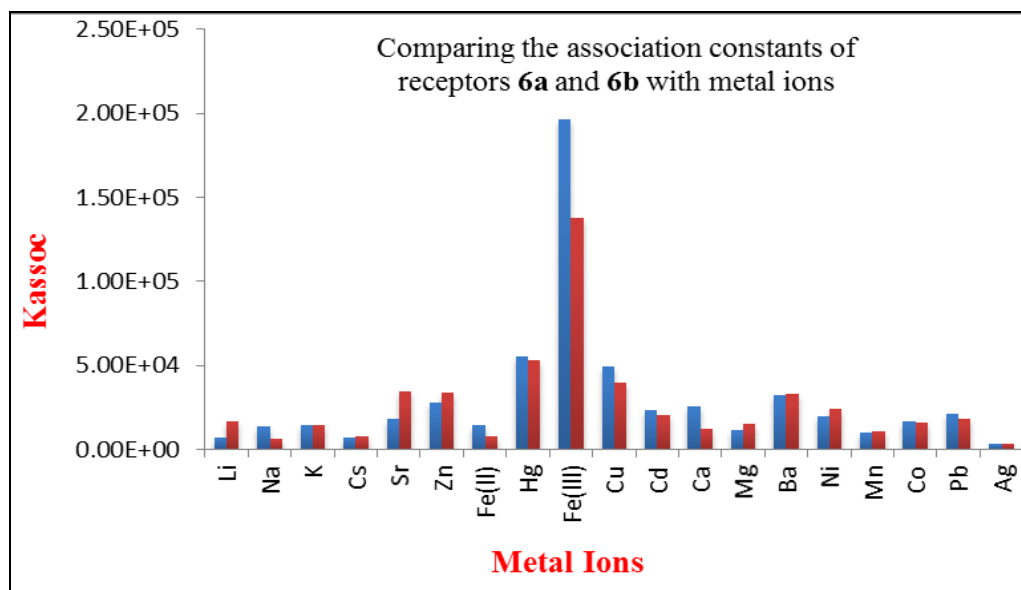


**Figure 4-12.** Histogram showing the association constants ( $K_{\text{assoc}}$ ) values determined for receptors **6a** (red) and **6b** (blue) with different metal ions.

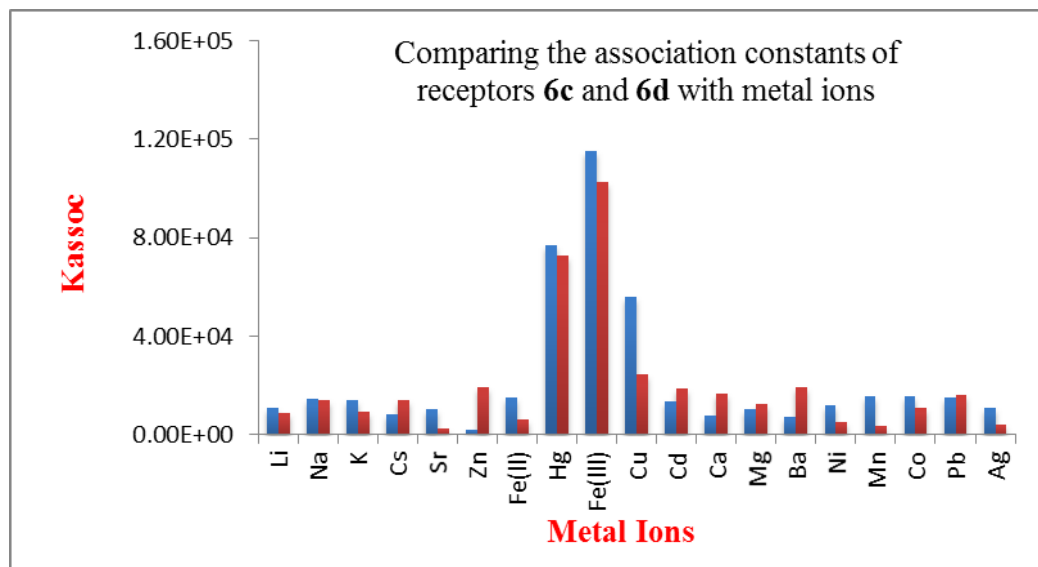


**Figure 4-13.** Histogram showing the association constants ( $K_{assoc}$ ) values determined for receptors **6c** (red) and **6d** (blue) with different metal ions.

### 4.3.3 $^1\text{H-NMR}$ complexation studies

$^1\text{H-NMR}$  spectroscopy was chosen as the other technique for the complexation study since it is better suited for determining the binding sites of the host molecules in the complexes. Stock solutions of the host molecules **6** ( $1.98 \times 10^{-2}$  M) were prepared in a  $\text{CD}_2\text{Cl}_2:\text{CD}_3\text{CN}$  (3:1, v/v) solvent mixture previously found to be suitable for the complexes.

#### 4.3.3.1 Complexation of receptor **6c** with $\text{Fe}^{3+}$

In order to further support the complex formation between *de-tBu* calix-triazole (**6c**) with metal cation ( $\text{Fe}^{3+}$ ),  $^1\text{H NMR}$  titration experiments were carried out. During the titration, the concentration of **6c** was kept constant and the added  $[\text{Fe}^{3+}]$  mole ratio was varied up to 2.0 equivalents. Addition of  $\text{Fe}^{3+}$  into the solution of **6c** in  $\text{CD}_2\text{Cl}_2:\text{CD}_3\text{CN}$

(3:1, v/v), the proton signals of the host *de-tBu* calix-triazole (**6c**) corresponding to the lower rim, viz. triazole-H( $\Delta$ )( $+\Delta\delta=0.13$  ppm), calix-OH( $\blacklozenge$ ) ( $+\Delta\delta=0.36$  ppm), and the bridged triazole-CH<sub>2</sub>( $*$ )( $+\Delta\delta=0.24$ ppm), protons were all found to shift downfield considerably, owing to binding of the Fe<sup>3+</sup> as shown in Figure 4-14.

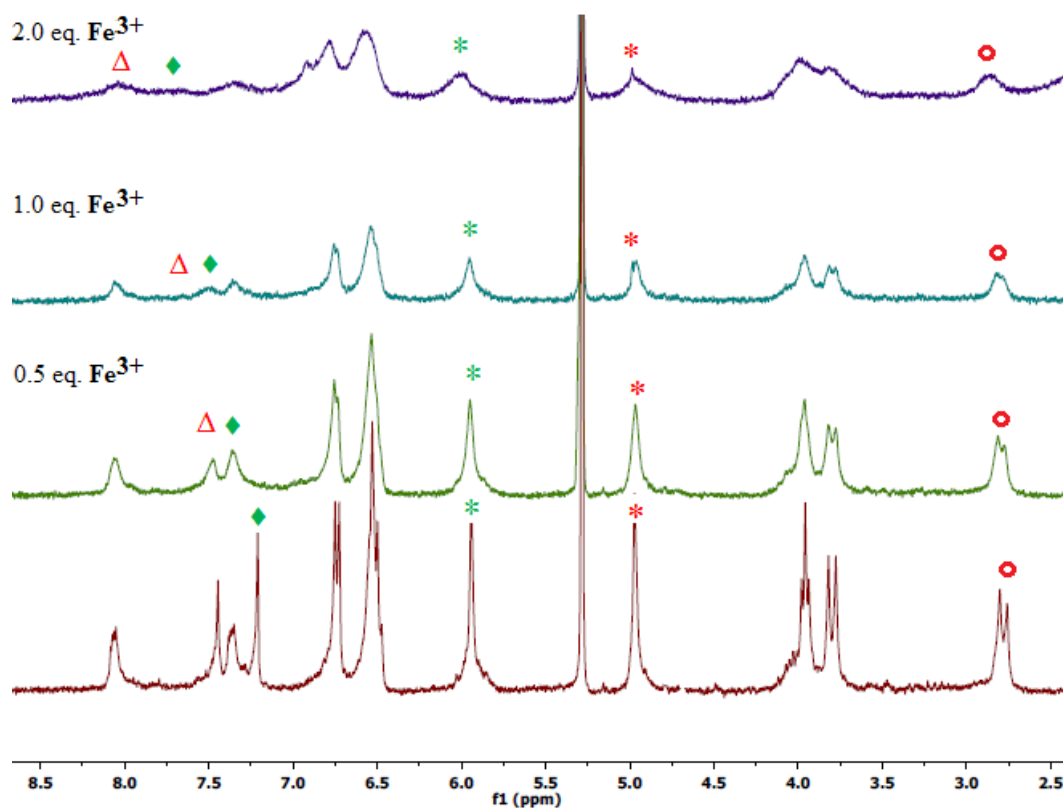


**Figure 4-14.** Partial <sup>1</sup>H NMR (300 MHz) spectra of **6c** ( $1.98 \times 10^{-2}$  M) upon addition of Fe(ClO<sub>4</sub>)<sub>3</sub> (0-2.0 equivalents) in a CD<sub>2</sub>Cl<sub>2</sub>:CD<sub>3</sub>CN (3:1, v/v) at 298K;  $\Delta$ ,  $\blacklozenge$ ,  $*$ ,  $*$ , and  $\circ$  denoted the denoted the triazole-H, calix-OH and triazole-CH<sub>2</sub>-naphthyl, calix-OCH<sub>2</sub>-triazole and calix-CH<sub>2</sub>-bridge protons.

#### 4.3.4 Computational studies

##### 4.3.4.1 General description for the computational study

To better understand the binding properties of receptors **6a** and **6c** with  $\text{Fe}^{3+}$ ,  $\text{Hg}^{2+}$  and  $\text{Cu}^{2+}$  ions a computation study was carried out. The individual structures for all studies in the gas-phase were fully geometry-optimized using Gaussian 09<sup>27,29</sup> with the B3LYP level of DFT and the lanl2dz basis set. The calculated complexation energies ( $\Delta E$  kJ/mole) for receptors **6a** and **6c** with  $\text{Fe}^{3+}$ ,  $\text{Hg}^{2+}$  and  $\text{Cu}^{2+}$  ions complexes are shown in Table 4-1. Significant distance changes were observed two triazole moieties for receptors **6a** and **6c** with metal metal ions complexes are shown Figure 4-15 to 4-20). The distance changes are summarized in Table 4-2 and Table 4-3.

##### 4.3.4.2 Calculated binding energies

The DFT B3LYP/lanl2dz basis set-calculated binding energies ( $\Delta E$ ) of the metal cations complexes of the receptors **6a(L)** and **6c(L)** formed between the metal cation( $\text{M}^{n+}$ ) and the free receptors **6a** and **6c** in the gas phase at 298 K are based on the equation (1), and the results are summarized in in Table 4.-1.

For this system, the binding energy  $\Delta E$  can be express as follows:

$$\Delta E = (L:M^{n+}_{\text{ions}})_{\text{complex}} - E(L_{\text{free}}) - E(M^{n+}_{\text{ions}}) \dots \dots \dots (1)$$

Where **L**=**6a** or **6c**, and  $\text{M}^{n+}$ = metal ions.

**Table 4-1.** Calculated binding energies (KJ/mole) for the receptors **6a** and **6c** with Fe<sup>3+</sup>, Hg<sup>2+</sup> and Cu<sup>2+</sup> cations.

Host	Binding energies for receptors <b>6a</b> and <b>6c</b> with metal ions		
	Fe <sup>3+</sup>	Cu <sup>2+</sup>	Hg <sup>2+</sup>
<b>6a</b>	-3623.80	-1784.89	-1345.41
<b>6c</b>	-3623.30	-1763.73	-1344.61

**Table 4-2.** The calculated distance for selected parameters for the Backbones of the receptor **6a** and complex with metal cations (M<sup>n+</sup>= Fe<sup>3+</sup>, Hg<sup>2+</sup> and Cu<sup>2+</sup>) optimized at B3LYP/ lan12dz Level (Distance in Å).

Parameter	<b>6a</b> Distance (Å)	<b>6a:Fe<sup>3+</sup></b> Distance (Å)	<b>6a:Hg<sup>2+</sup></b> Distance (Å)	<b>6a:Cu<sup>2+</sup></b> Distance (Å)
N <sub>5</sub> -N <sub>16</sub>	7.481	3.024	3.577	2.990
N <sub>6</sub> -N <sub>17</sub>	7.715	3.517	3.712	3.370
N <sub>6</sub> -O <sub>46</sub>	5.754	3.410	3.818	3.012
N <sub>6</sub> -O <sub>64</sub>	5.915	3.901	4.200	3.628
N <sub>17</sub> -O <sub>46</sub>	5.632	4.244	4.476	3.012
N <sub>17</sub> -O <sub>64</sub>	4.231	2.898	3.307	3.628
H <sub>77</sub> -H <sub>115</sub>	6.692	8.548	9.326	8.713
M <sup>n+</sup> -N <sub>6</sub>	5.205	2.149	2.314	2.014
M <sup>n+</sup> - N <sub>17</sub>	5.207	2.272	2.381	1.988
M <sup>n+</sup> - O <sub>46</sub>	9.21	2.104	2.372	2.016
M <sup>n+</sup> O <sub>64</sub>	5.579	2.126	2.413	2.411

**Table 4-3.** The calculated distance for selected parameters for the Backbones of the receptor **6c** and complex with metal cations (M= Fe<sup>3+</sup>, Hg<sup>2+</sup> and Cu<sup>2+</sup>) optimized at B3LYP/ lanl2dz Level (Distance in Å).

Parameter	<b>6c</b> Distance (Å)	<b>6c:Fe<sup>3+</sup></b> Distance (Å)	<b>6c:Hg<sup>2+</sup></b> Distance (Å)	<b>6c:Cu<sup>2+</sup></b> Distance (Å)
N <sub>5</sub> -N <sub>16</sub>	7.465	3.355	3.694	4.721
N <sub>6</sub> -N <sub>17</sub>	7.702	3.035	3.587	3.946
N <sub>6</sub> -O <sub>46</sub>	5.763	2.962	3.234	2.579
N <sub>6</sub> -O <sub>64</sub>	5.909	4.060	4.33	5.000
N <sub>17</sub> -O <sub>46</sub>	5.620	3.986	4.338	3.711
N <sub>17</sub> -O <sub>64</sub>	4.239	3.521	3.929	3.372
H <sub>77</sub> -H <sub>121</sub>	6.707	8.742	9.370	7.443
M <sup>n+</sup> -N <sub>6</sub>	-	2.201	2.340	3.136
M <sup>n+</sup> -N <sub>17</sub>	-	2.176	2.347	2.029
M <sup>n+</sup> -O <sub>46</sub>	-	2.162	2.437	1.947
M <sup>n+</sup> -O <sub>64</sub>	-	2.088	2.351	2.122

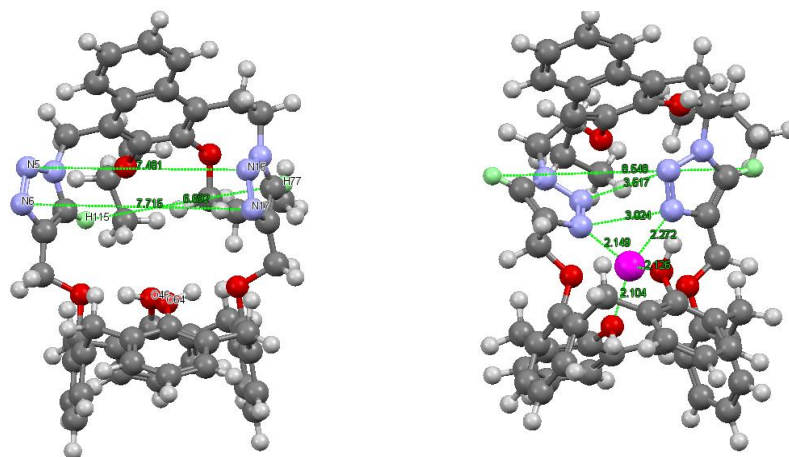


**Figure 4-15.** Geometry-optimized (ball-and-stick) structures of: *Left: 6a* and *Right: 6a*⊃Fe<sup>3+</sup> complex. Colour code: Fe<sup>3+</sup> = magenta, triazole nitrogen = blue, triazole hydrogen = light green and oxygen atom = red. Hydrogen atoms have been omitted for clarity.

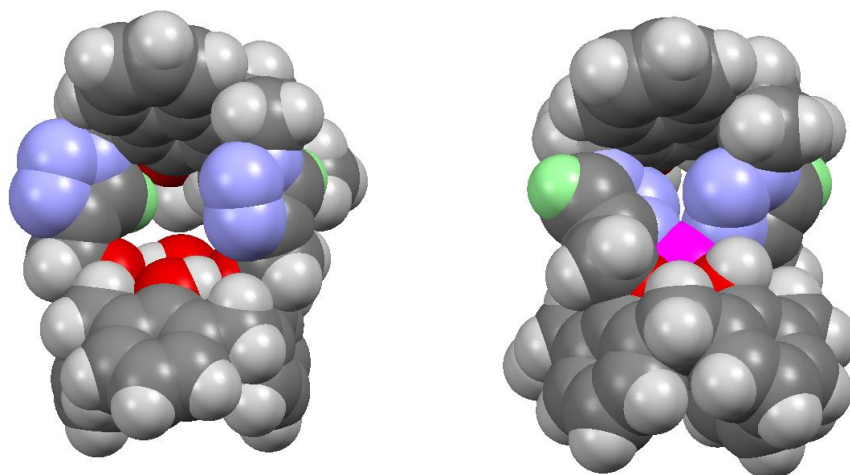


**Figure 4-16.** Geometry-optimized (space fill) structures of: *Left: 6a* and *Right: 6a*⊃ $\text{Fe}^{3+}$  complex. Colour code:  $\text{Fe}^{3+}$  = magenta, triazole nitrogen = blue, triazole hydrogen = light green and oxygen atom = red. Hydrogen atoms have been omitted for clarity.

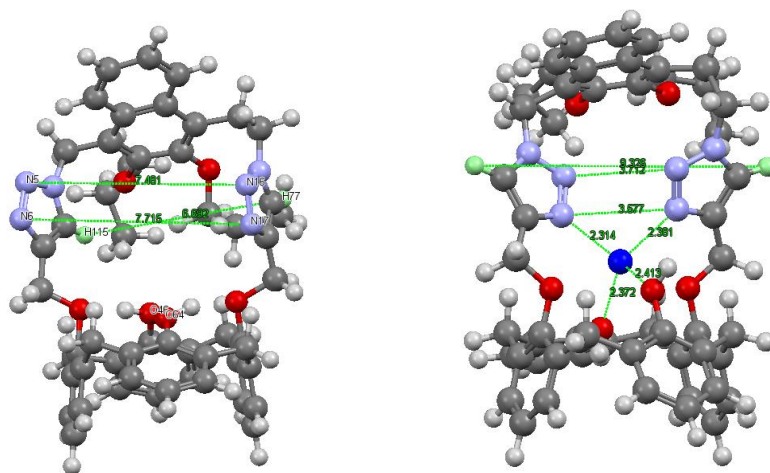


**Figure 4-17.** Geometry-optimized (ball-and-stick) structures of: *Left: 6a* and *Right: 6a*⊃ $\text{Hg}^{2+}$  complex. Colour code:  $\text{Hg}^{2+}$  = deep blue, triazole nitrogen = blue, triazole hydrogen = light green and oxygen atom = red. Hydrogen atoms have been omitted for clarity.

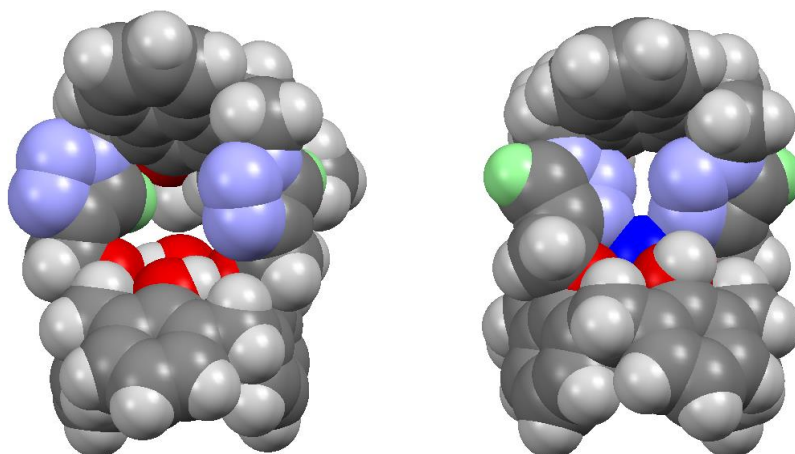


**Figure 4-18.** Geometry-optimized (space fill) structures of: *Left: 6a* and *Right: 6a⊃Hg<sup>2+</sup>* complex. Colour code: Hg<sup>2+</sup> = deep blue, triazole nitrogen = blue, triazole hydrogen = light green and oxygen atom = red. Hydrogen atoms have been omitted for clarity.

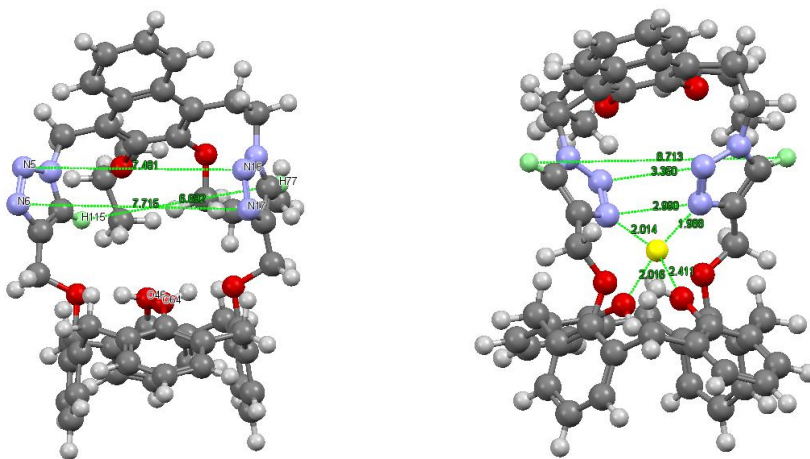


**Figure 4-19.** Geometry-optimized (ball-and-stick) structures of: *Left: 6a* and *Right: 6a⊃Cu<sup>2+</sup>* complex. Colour code: Hg<sup>2+</sup> = yellow, triazole nitrogen = blue, triazole hydrogen = light green and oxygen atom = red. Hydrogen atoms have been omitted for clarity.

#### 4.4 Conclusions

The new macrocyclic receptors namely, triazolyl-bridged naphthanene-calix[4]arenes **6a-6d**, were successfully synthesised by Dr. S. Rahman in the Georghiou Laboratory. In the study reported herein, their complexation properties with various metal ions were investigated using both fluorescence and  $^1\text{H-NMR}$  spectroscopy. The fluorescence studies showed that **6a-6d** possess high binding selectivities towards  $\text{Fe}^{3+}$ ,  $\text{Hg}^{2+}$  and  $\text{Cu}^{2+}$  ions as indicated by significant fluorescence quenching in their titration spectra.. The triazole proton signals showed the greatest chemical shift changes during the titration experiments indicating that the triazole units are the binding sites in the supramolecular complexes formed by the metal ions with macrocycles **6a-6d**. On the basis of the computation and  $^1\text{H NMR}$  studies, it can be proposed that the metal cations ( $\text{Fe}^{3+}$ ;  $\text{Hg}^{2+}$  and  $\text{Cu}^{2+}$ ) binds to the lower rim region (calix-OH and triazole region,  $\text{N}_2\text{O}_2$  core).

## 4.5 References

1. a) Gutsche, C. D.; Muthukrishnan, R. *J. Org. Chem.* **1978**, *43*, 4905–4906; b) Dalgarno, S. J.; Thallapally, P. K.; Barbour, L. J.; Atwood, J. L. *Chem. Soc. Rev.* **2007**, *36*, 236–245.
2. Kim, J. S.; Quang, D. T. *Chem. Rev.* **2007**, *107*, 3780–3799.
3. Creaven, B. S.; Donlon, D. F.; McGinley, J. *Coord. Chem. Rev.* **2009**, *253*, 893–962.
4. Lo, P.; Wong, M. *Sensors*, **2008**, *8*, 5313–5335.
5. Valeur, B.; Leray, I. *Inorg. Chim. Acta.* **2007**, *360*, 765–774.
6. Farina, M.; Avila, D. S.; Rocha, J. B.; Aschner, M. *Neurochemistry Intrna.* **2013**, *62*, 575–594.
7. Chio, Y. W.; Park, G. H.; Na, Y. J.; Jo, H. Y.; Lee, S. A.; You, G. R.; Kim, C. *Sensors and Actutors B.* **2014**, *193*, 343–352.
8. Bourne, Y.; Kolb, H. C.; Radic', Z.; Sharpless, K. B.; Taylor, P.; Marchot, P.; *Proc. Natl. Acad. Sci.* **2004**, *101*, 1449–1454.
9. Tornøe, C. W.; Sanderson, S. J.; Mottram, J. C.; Coombs, G. H.; Meldal, M. *J. Comb. Chem.* **2004**, *6*, 312–324.
10. Naito, Y.; Akahoshi, F.; Takeda, S.; Okada, T.; Kajii, M.; Nishimura, H.; Sugiura, M.; Fukaya, C.; Kagitani, Y. *J. Med. Chem.* **1996**, *39*, 3019–3029.
11. Genin, M. J.; Allwine, D. A.; Anderson, D. J.; Barbachyn, M. R.; Emmert, D. E.; Garmon, S. A.; Graber, D. R.; Grega, K. C.; Hester, J. B.; Hutchinson, D. K.; J. Morris, Reischer, R. J.; Ford, C. W.; Zurenko, G. E.; Hamel, J. C.; Schaadt, R. D.; D. Stapert, Yagi, B. H.; *J. Med. Chem.* **2000**, *43*, 953–970.

12. Buckle, D. R.; Rockell, C. J. M.; Smith, H.; Spicer, B. A. *J. Med. Chem.* **1986**, *29*, 2262–2267.
13. Ryu, E.; Zhao, Y. *Org. Lett.* **2005**, *7*, 1305–1307.
14. Chang, K.C.; Su, I. H.; Senthilvelan, A.; Chung, W.S. *Org. Lett.*, **2007**, *9*, 3363–3366.
15. Pathak, R. K.; Ibrahim, S. M.; Rao, C. P. *Tetrahedron Lett.* **2009**, *50*, 2730–2734.
16. Ilioudis, C. A.; Tocher, D. A.; Steed, J. W. *J. Am. Chem. Soc.* **2004**, *126*, 12395–12402.
17. Fan, E.; Van Arman, S. A.; Kincaid, S.; Hamilton, A. D. *J. Am. Chem. Soc.* **1993**, *115*, 369–370.
18. Valiyaveetil, S.; Engbersen, J. F. J.; Verboom, W.; Reinhoudt, D. N. *Angew. Chem.* **1993**, *105*, 942–944; *Angew. Chem. Int. Ed.* **1993**, *32*, 900–901.
19. Best, M. D.; Tobey, S. L.; Anslyn, E. V. *Coord. Chem. Rev.* **2003**, *240*, 3–15.
20. Lee, C. H.; Miyaji, H.; Yoon, D. W.; Sessler, J. L. *Chem. Commun.* **2008**, *10*, 24–34.
21. Beckendorf, S.; Asmus, S. Lichtenfeld, C. M.; Manche, O. G. *Chem. Eur. J.* **2013**, *19*, 1581–1585.
22. Palmer, M. H.; Findlay, R. H.; Gaskell, A. J. *J. Chem. Soc.* **1974**, 420–428.
23. McDonald, K. P.; Ramabhadran, R. O.; Lee, S.; Raghavachari, K.; Flood, A. H. *Org. Lett.* **2011**, *13*, 6260–6263.
24. (a) Gutsche, C. D.; Iqbal, M. *Org. Synth.* **1990**, *68*, 234–242; (b) Gutsche, C. D.; Dhawan, B.; Levine, J. A.; No, K. H.; Bauer, L. *J. Tetrahedron* **1983**, *39*, 409–426, (c) Xu, W.; Vittal, J. J.; Puddephatt, R. J. *Can. J. Chem.* **1996**, *74*, 766–774.

25. Pathak, R. K.; Hinge, V. K.; Mondal, M.; Rao, C. P. *J. Org. Chem.* **2011**, *76*, 10039–10049.
26. Tran, A. H.; Miller, D. O.; Georghiou, P. E. *J. Org. Chem.* **2005**, *70*, 1115–1121.
27. *Gaussian 09, Revision C.01*, Frisch, M. J.; Trucks, G. W.; Schlegel, H. B.; Scuseria, G. E.; Robb, M. A.; Cheeseman, J. R.; Scalmani, G.; Barone, V.; Mennucci, B.; Petersson, G. A.; Nakatsuji, H.; Caricato, M.; Li, X.; Hratchian, H. P.; Izmaylov, A. F.; Bloino, J.; Zheng, G.; Sonnenberg, J. L.; Hada, M.; Ehara, M.; Toyota, K.; Fukuda, R.; Hasegawa, J.; Ishida, M.; Nakajima, T.; Honda, Y.; Kitao, O.; Nakai, H.; Vreven, T.; Montgomery, Jr. J. A.; Peralta, J. E.; Ogliaro, F.; Bearpark, M.; Heyd, J. J.; Brothers, E.; Kudin, K. N.; Staroverov, V. N.; Keith, T.; Kobayashi, R.; Normand, J.; Raghavachari, K.; Rendell, A.; Burant, J. C.; Iyengar, S. S.; Tomasi, J.; Cossi, M.; Rega, N.; Millam, J. M.; Klene, M.; Knox, J. E.; Cross, J. B.; Bakken, V.; Adamo, C.; Jaramillo, J.; Gomperts, R.; Stratmann, R. E.; Yazyev, O.; Austin, A. J.; Cammi, R.; Pomelli, C.; Ochterski, J. W.; Martin, R. L.; Morokuma, K.; Zakrzewski, V. G.; Voth, G. A.; Salvador, P.; Dannenberg, J. J.; Dapprich, S.; Daniels, A. D.; Farkas, O.; Foresman, J. B.; Ortiz, J. V.; Cioslowski, J.; Fox, D. J. *Gaussian, Inc., Wallingford CT, 2010.*
28. Benesi, H. A.; Hildebrand, J. H. *J. Am. Chem. Soc.* **1949**, *71*, 2703–2707.
29. Computational studies were conducted by Dr. Shofiur Rahman and Professor Paris Georghiou. Dr. Grigory Shamov of WetGrid/Compute Canada is thanked for technical assistance.

## Appendix

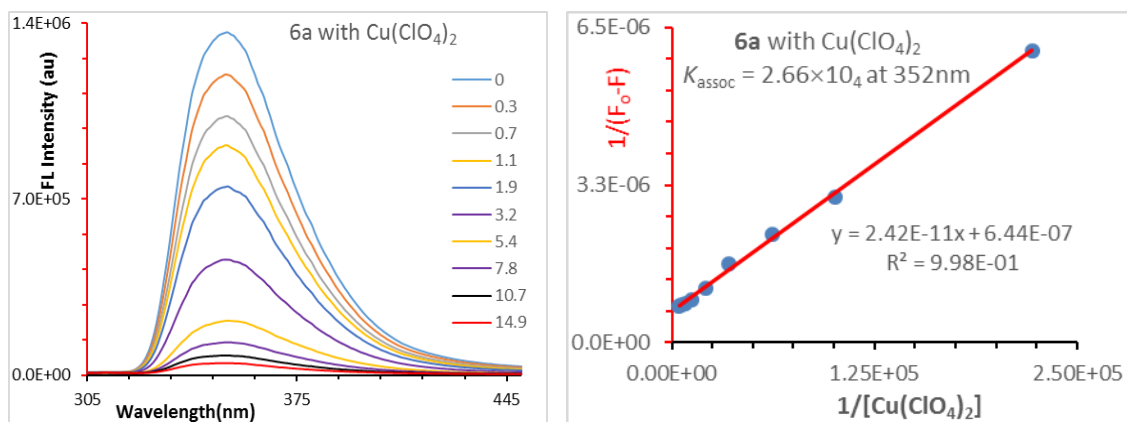


**Figure 4-20.** *Left:* Fluorescence spectra of **6a** (1.50  $\mu\text{M}$ ) upon addition of  $\text{Cu}^{2+}$  in acetonitrile/ chloroform (v/v = 9:1) solutions.  $\lambda_{\text{ex}} = 284$  nm. *Right:* Benesi-Hildebrand plot of  $1/(F_0 - F)$  versus  $1/[\text{Cu}(\text{ClO}_4)_2]$  for **6a** upon titration with  $\text{Cu}(\text{ClO}_4)_2$  (0-15 equivalents). The linear fit showed a 1:1 complexation between **6a** and  $\text{Cu}^{2+}$  ions. The association constant was calculated at 352 nm wavelength.

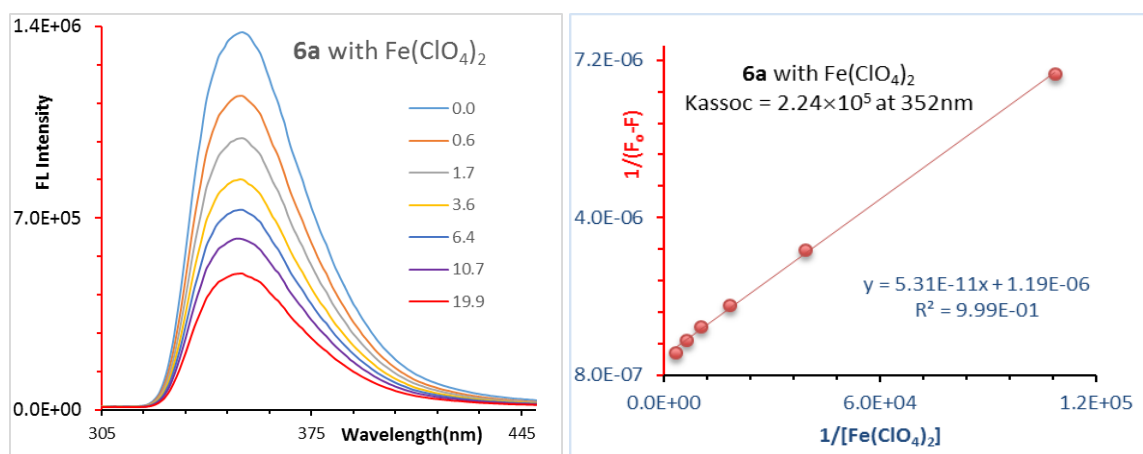


**Figure 4-21.** *Left:* Fluorescence spectra of **6a** (1.50  $\mu\text{M}$ ) upon addition of  $\text{Fe}^{2+}$  in acetonitrile/ chloroform (v/v = 9:1) solutions.  $\lambda_{\text{ex}} = 284$  nm. *Right:* Benesi-Hildebrand plot of  $1/(F_0 - F)$  versus  $1/[\text{Fe}(\text{ClO}_4)_2]$  for **6a** upon titration with  $\text{Fe}(\text{ClO}_4)_2$  (0-20 equivalents). The linear fit showed a 1:1 complexation between **6a** and  $\text{Fe}^{2+}$  ions. The association constant was calculated at 352 nm wavelength.

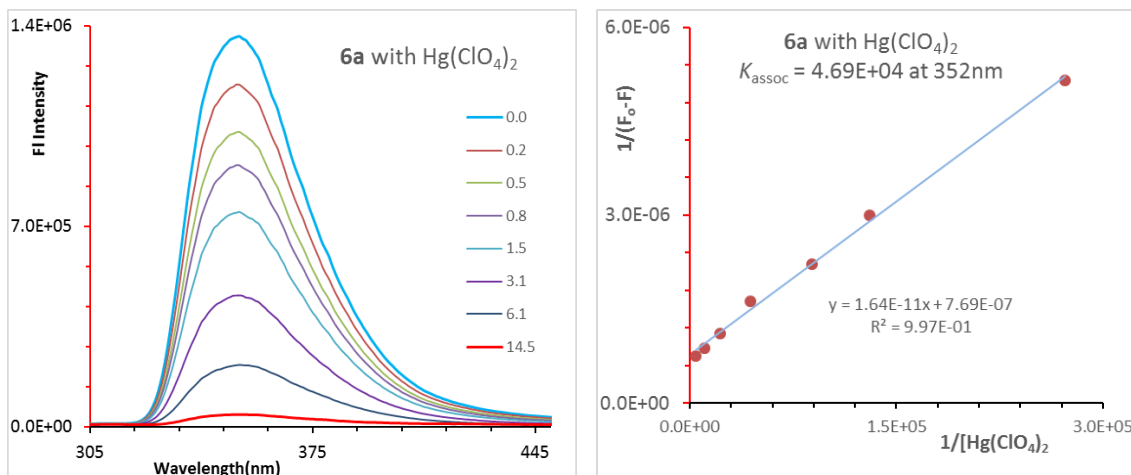


**Figure 4-22.** *Left:* Fluorescence spectra of **6a** (1.50  $\mu\text{M}$ ) upon addition of  $\text{Hg}^{2+}$  in acetonitrile/ chloroform (v/v= 9:1) solutions.  $\lambda_{\text{ex}} = 284 \text{ nm}$ . *Right:* Benesi-Hildebrand plot of  $1/(F_0-F)$  versus  $1/[\text{Hg}(\text{ClO}_4)_2]$  for **6a** upon titration with  $\text{Hg}(\text{ClO}_4)_2$  (0-14.5 equivalents). The linear fit showed a 1:1 complexation between **6a** and  $\text{Hg}^{2+}$  ions. The association constant was calculated at 352 nm wavelength.

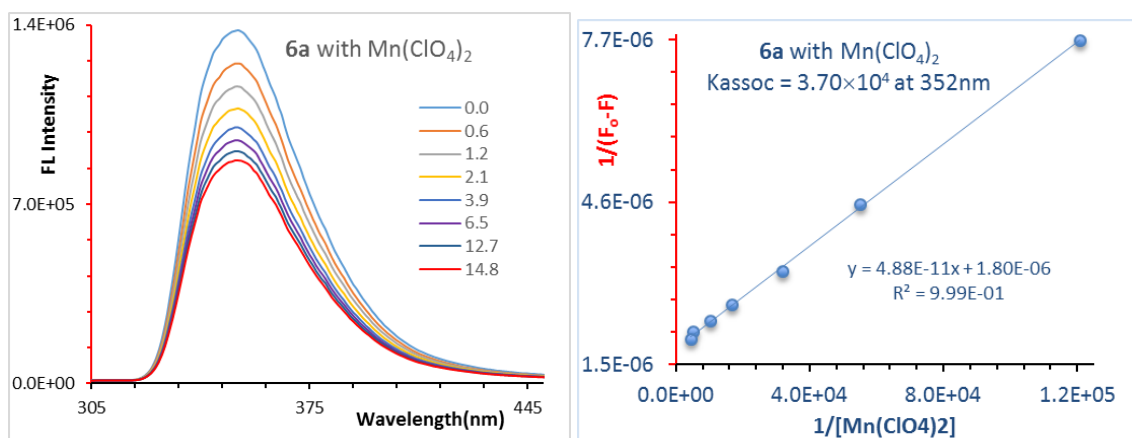


**Figure 4-23.** *Left:* Fluorescence spectra of **6a** (1.50  $\mu\text{M}$ ) upon addition of  $\text{Mn}^{2+}$  in acetonitrile/ chloroform (v/v= 9:1) solutions.  $\lambda_{\text{ex}} = 284 \text{ nm}$ . *Right:* Benesi-Hildebrand plot of  $1/(F_0-F)$  versus  $1/[\text{Mn}(\text{ClO}_4)_2]$  for **6a** upon titration with  $\text{Mn}(\text{ClO}_4)_2$  (0-14.8 equivalents). The linear fit showed a 1:1 complexation between **6a** and  $\text{Mn}^{2+}$  ions. The association constant was calculated at 352 nm wavelength.

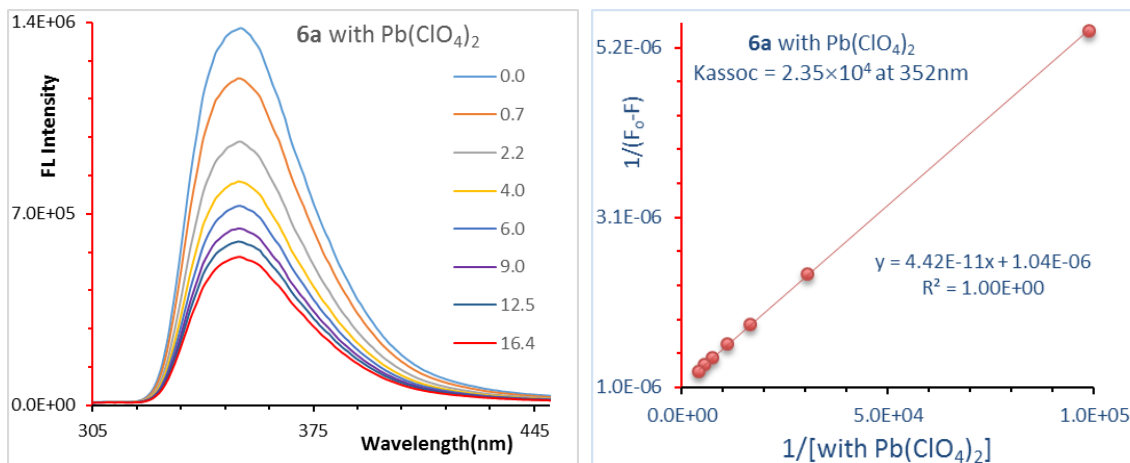


**Figure 4-24.** *Left:* Fluorescence spectra of **6a** (1.50  $\mu\text{M}$ ) upon addition of  $\text{Pb}^{2+}$  in acetonitrile/ chloroform ( $v/v= 9:1$ ) solutions.  $\lambda_{\text{ex}} = 284 \text{ nm}$ . *Right:* Benesi-Hildebrand plot of  $1/(F_0-F)$  versus  $1/[\text{Pb}(\text{ClO}_4)_2]$  for **6a** upon titration with  $\text{Pb}(\text{ClO}_4)_2$  (0-16.4 equivalents). The linear fit showed a 1:1 complexation between **6a** and  $\text{Pb}^{2+}$  ions. The association constant was calculated at 352 nm wavelength.

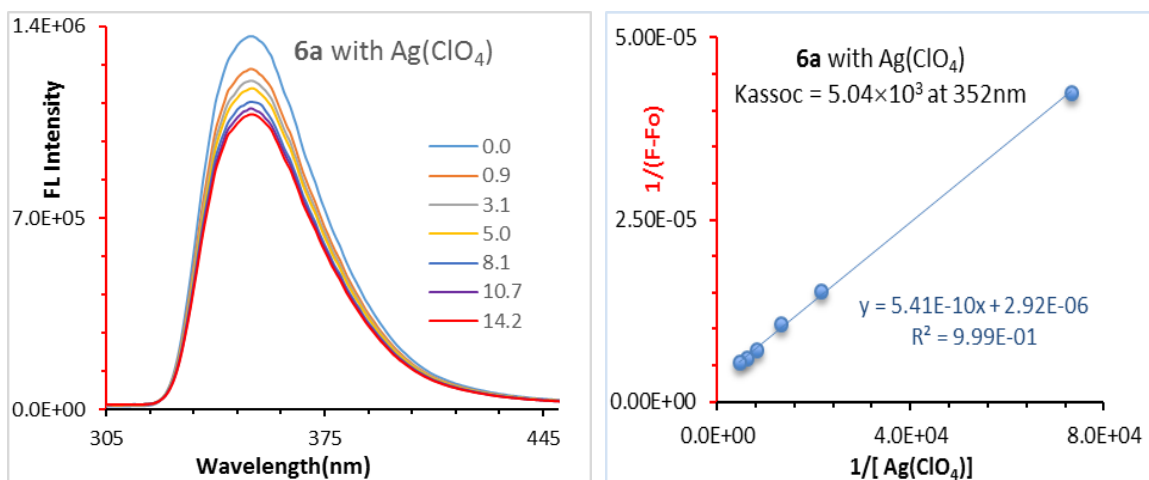


**Figure 4-25.** *Left:* Fluorescence spectra of **6a** (1.50  $\mu\text{M}$ ) upon addition of  $\text{Ag}^+$  in acetonitrile/ chloroform ( $v/v= 9:1$ ) solutions.  $\lambda_{\text{ex}} = 284 \text{ nm}$ . *Right:* Benesi-Hildebrand plot of  $1/(F_0-F)$  versus  $1/[\text{AgClO}_4]$  for **6a** upon titration with  $\text{Ag}(\text{ClO}_4)$  (0-14.2 equivalents). The linear fit showed a 1:1 complexation between **6a** and  $\text{Ag}^+$  ions. The association constant was calculated at 352 nm wavelength.

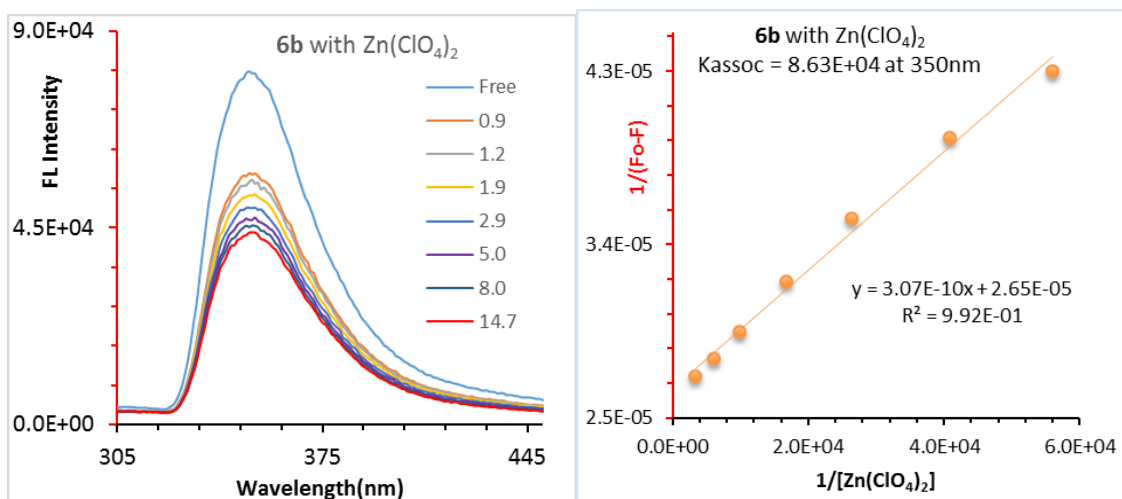


**Figure 4-26.** *Left:* Fluorescence response of chemosensor **6b** (1.50 μM) to various equivalents of Zn(ClO<sub>4</sub>)<sub>2</sub> in acetonitrile/chloroform (v/v= 9:1) solutions. The excitation wavelength was λ 291 nm. *Right:* Benesi-Hildebrand plot of 1/(F<sub>0</sub>-F) versus 1/[Zn(ClO<sub>4</sub>)<sub>2</sub>] for **6b** upon titration with Zn(ClO<sub>4</sub>)<sub>2</sub> (0-14.7 equivalents). The linear fit showed a 1:1 complexation between **6b** and Zn<sup>2+</sup> ions. The association constant was calculated at 352 nm wavelength.

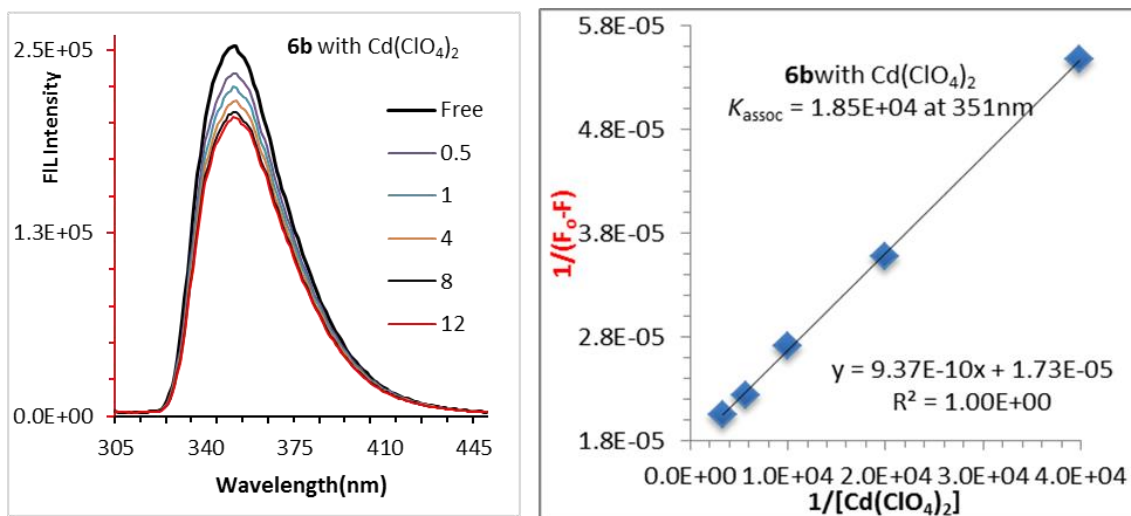


**Figure 4-27.** *Left:* Fluorescence response of chemosensor **6b** (1.50 μM) to various equivalents of Cd(ClO<sub>4</sub>)<sub>2</sub> in acetonitrile/chloroform (v/v= 9:1) solutions. The excitation wavelength was λ 291 nm. *Right:* Benesi-Hildebrand plot of 1/(F<sub>0</sub>-F) versus 1/[Cd(ClO<sub>4</sub>)<sub>2</sub>] for **6b** upon titration with Cd(ClO<sub>4</sub>)<sub>2</sub> (0-12 equivalents). The linear fit showed a 1:1 complexation between **6b** and Cd<sup>2+</sup> ions. The association constant was calculated at 352 nm wavelength.

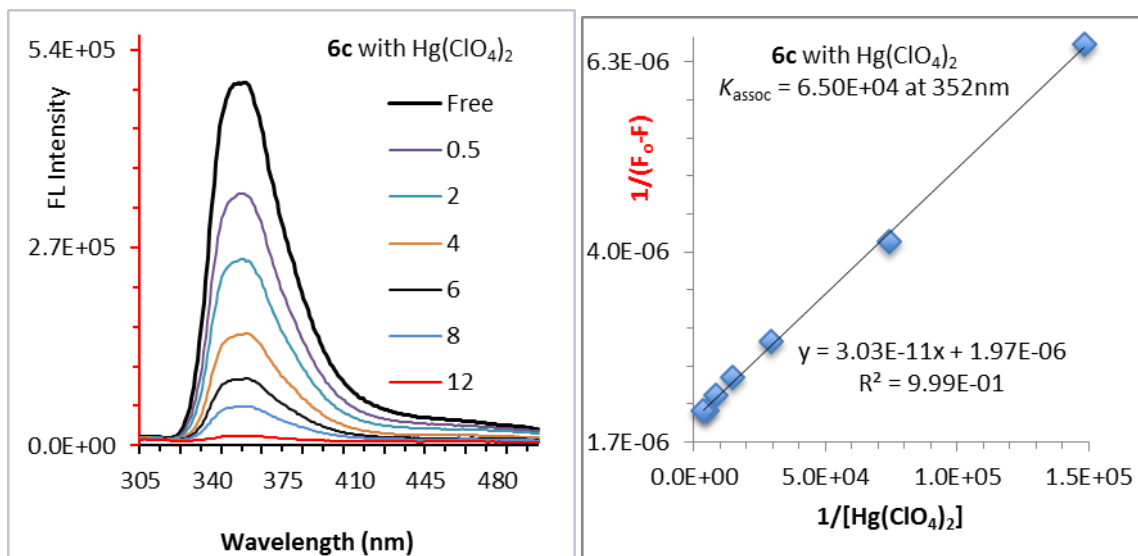


**Figure 4-28.** *Left:* Fluorescence response of chemosensor **6c** (1.50  $\mu\text{M}$ ) to various equivalents of  $\text{Hg}(\text{ClO}_4)_2$  in acetonitrile/chloroform (v/v= 9:1) solutions. The excitation wavelength was  $\lambda$  291 nm. *Right:* Benesi-Hildebrand plot of  $1/(F_0 - F)$  versus  $1/[\text{Hg}(\text{ClO}_4)_2]$  for **6c** upon titration with  $\text{Hg}(\text{ClO}_4)_2$  (0-12 equivalents). The linear fit showed a 1:1 complexation between **6c** and  $\text{Hg}^{2+}$  ions. The association constant was calculated at 352 nm wavelength.

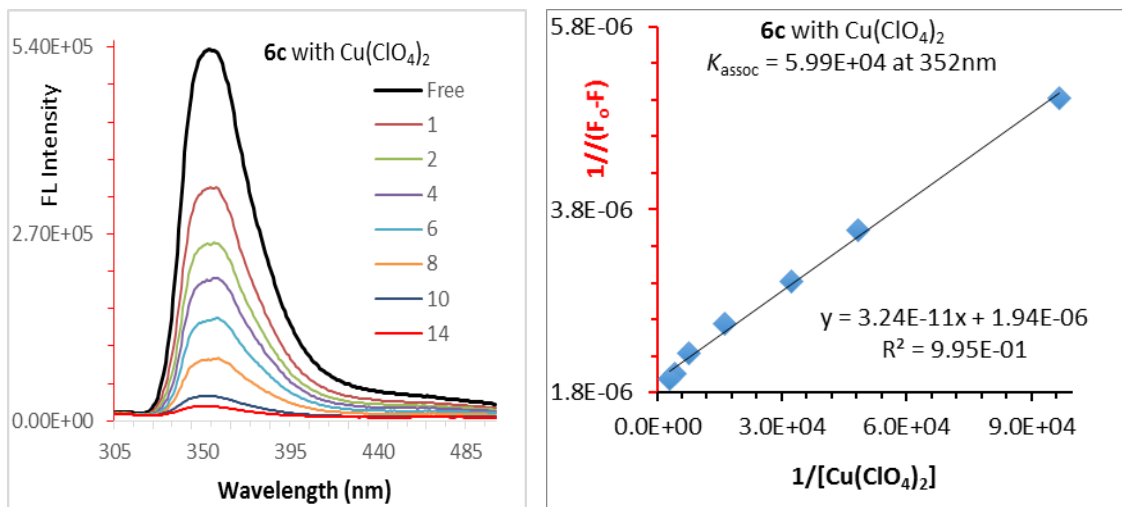


**Figure 4-29.** *Left:* Fluorescence response of chemosensor **6c** (1.50  $\mu\text{M}$ ) to various equivalents of  $\text{Cu}(\text{ClO}_4)_2$  in acetonitrile/chloroform (v/v= 9:1) solutions. The excitation wavelength was  $\lambda$  291 nm. *Right:* Benesi-Hildebrand plot of  $1/(F_0 - F)$  versus  $1/[\text{Cu}(\text{ClO}_4)_2]$  for **6c** upon titration with  $\text{Cu}(\text{ClO}_4)_2$  (0-14 equivalents). The linear fit showed a 1:1 complexation between **6c** and  $\text{Cu}^{2+}$  ions. The association constant was calculated at 352 nm wavelength.

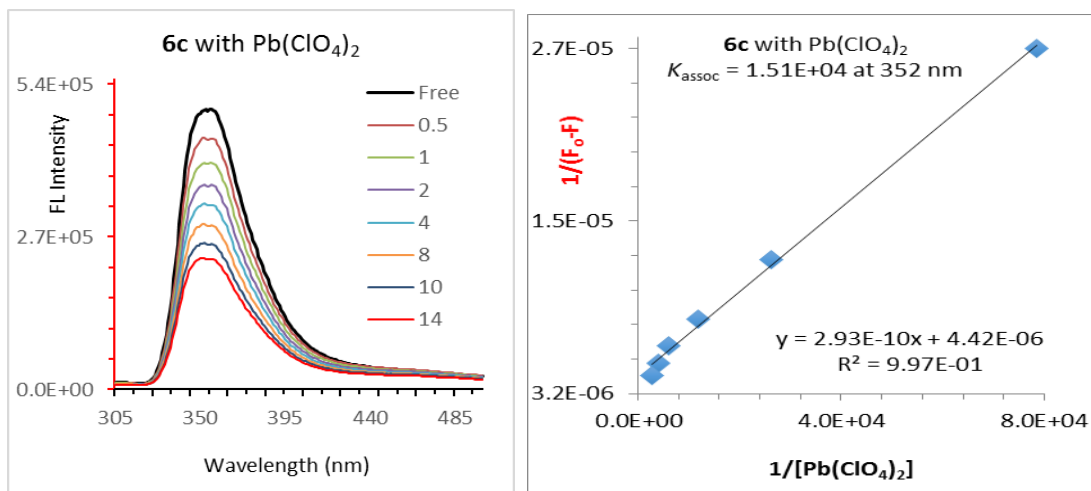


**Figure 4-30.** *Left:* Fluorescence response of chemosensor **6c** (1.50 μM) to various equivalents of Pb(ClO<sub>4</sub>)<sub>2</sub> in acetonitrile/chloroform (v/v= 9:1) solutions. The excitation wavelength was λ 291 nm. *Right:* Benesi-Hildebrand plot of 1/(F<sub>0</sub>-F) versus 1/[Pb(ClO<sub>4</sub>)<sub>2</sub>] for **6c** upon titration with Pb(ClO<sub>4</sub>)<sub>2</sub> (0-14 equivalents). The linear fit showed a 1:1 complexation between **6c** and Pb<sup>2+</sup> ions. The association constant was calculated at 352 nm wavelength.

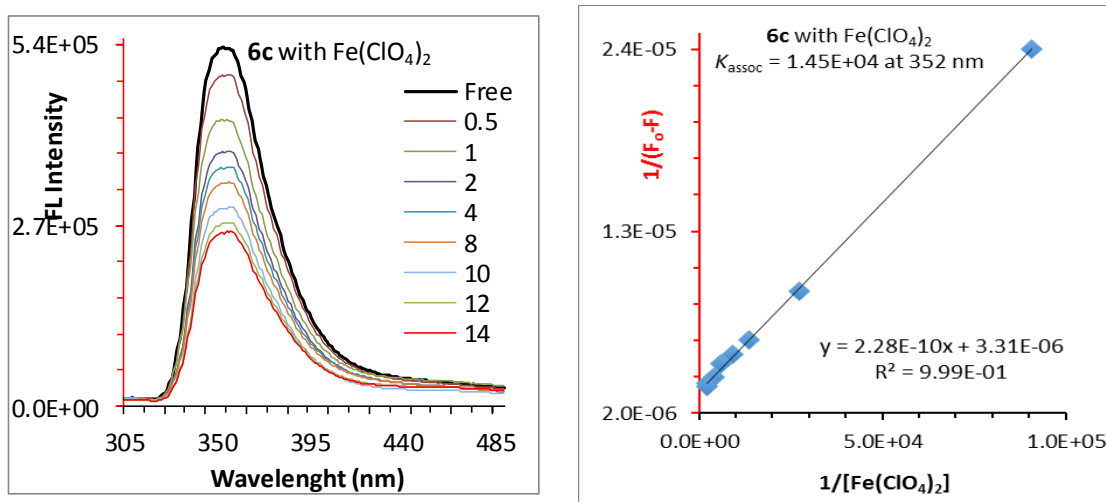


**Figure 4-31.** *Left:* Fluorescence response of chemosensor **6c** (1.50 μM) to various equivalents of Fe(ClO<sub>4</sub>)<sub>2</sub> in acetonitrile/chloroform (v/v= 9:1) solutions. The excitation wavelength was λ 291 nm. *Right:* Benesi-Hildebrand plot of 1/(F<sub>0</sub>-F) versus 1/[Fe(ClO<sub>4</sub>)<sub>2</sub>] for **6c** upon titration with Fe(ClO<sub>4</sub>)<sub>2</sub> (0-14 equivalents). The linear fit showed a 1:1 complexation between **6c** and Fe<sup>2+</sup> ions. The association constant was calculated at 352 nm wavelength.

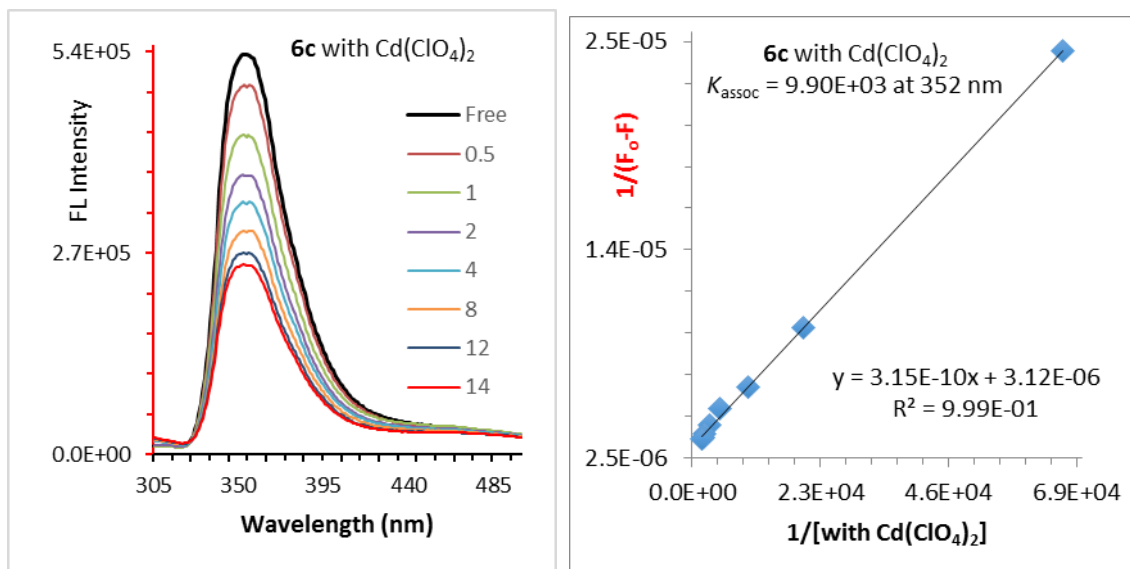


**Figure 4-32.** *Left:* Fluorescence response of chemosensor **6c** (1.50  $\mu\text{M}$ ) to various equivalents of  $\text{Cd}(\text{ClO}_4)_2$  in acetonitrile/chloroform (v/v= 9:1) solutions. The excitation wavelength was  $\lambda$  291 nm. *Right:* Benesi-Hildebrand plot of  $1/(F_0-F)$  versus  $1/[\text{Cd}(\text{ClO}_4)_2]$  for **6c** upon titration with  $\text{Cd}(\text{ClO}_4)_2$  (0-14 equivalents). The linear fit showed a 1:1 complexation between **6c** and  $\text{Cd}^{2+}$  ions. The association constant was calculated at 352 nm wavelength.

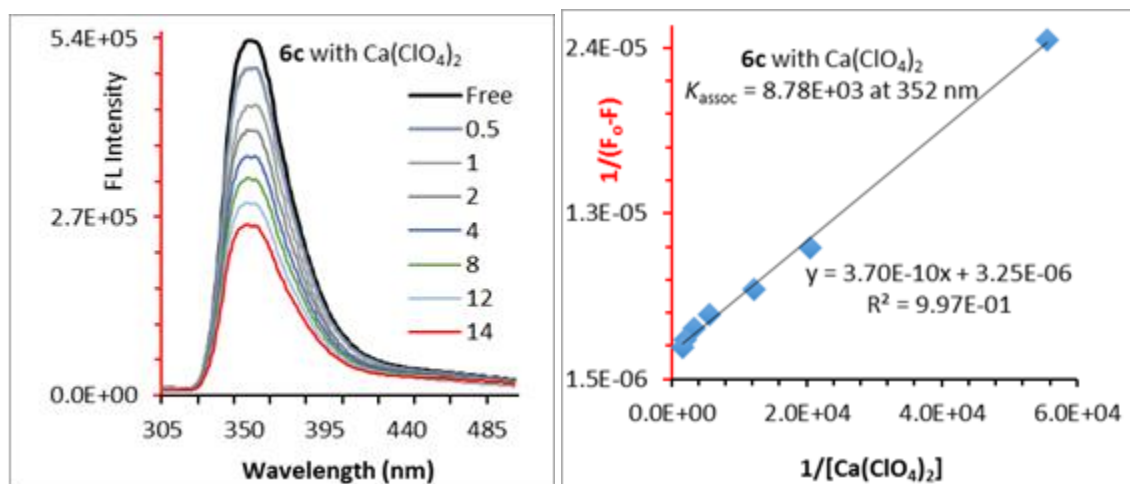


**Figure 4-33.** *Left:* Fluorescence response of chemosensor **6c** (1.50  $\mu\text{M}$ ) to various equivalents of  $\text{Ca}(\text{ClO}_4)_2$  in acetonitrile/chloroform (v/v= 9:1) solutions. The excitation wavelength was  $\lambda$  291 nm. *Right:* Benesi-Hildebrand plot of  $1/(F_0-F)$  versus  $1/[\text{Ca}(\text{ClO}_4)_2]$  for **6c** upon titration with  $\text{Ca}(\text{ClO}_4)_2$  (0-14 equivalents). The linear fit showed a 1:1 complexation between **6c** and  $\text{Ca}^{2+}$  ions. The association constant was calculated at 352 nm wavelength.

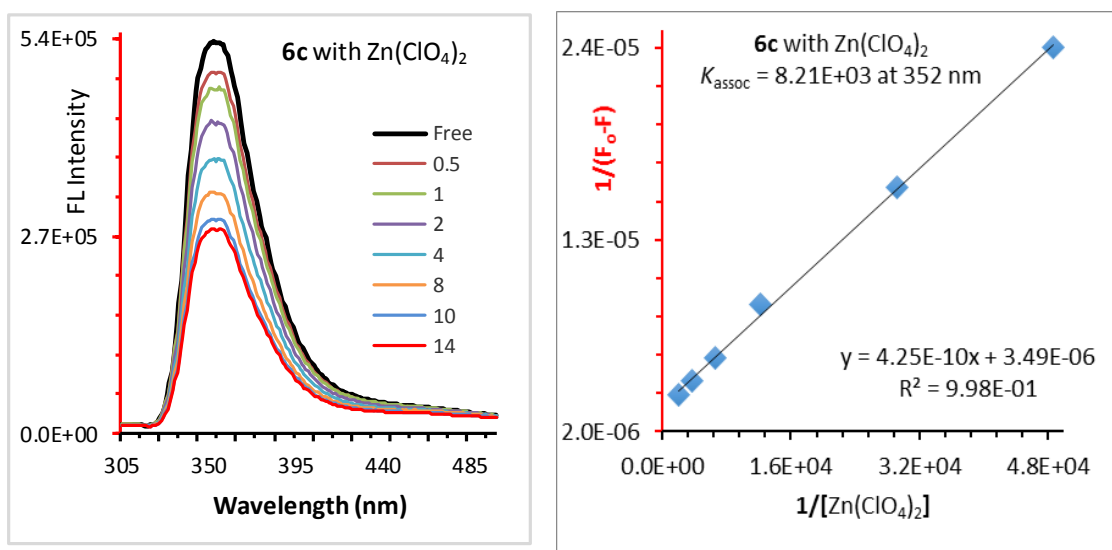


**Figure 4-34.** *Left:* Fluorescence response of chemosensor **6c** (1.50  $\mu\text{M}$ ) to various equivalents of  $\text{Zn}(\text{ClO}_4)_2$  in acetonitrile/chloroform (v/v= 9:1) solutions. The excitation wavelength was  $\lambda$  291 nm. *Right:* Benesi-Hildebrand plot of  $1/(F_0-F)$  versus  $1/[\text{Zn}(\text{ClO}_4)_2]$  for **6c** upon titration with  $\text{Zn}(\text{ClO}_4)_2$  (0-14 equivalents). The linear fit showed a 1:1 complexation between **6c** and  $\text{Zn}^{2+}$  ions. The association constant was calculated at 352 nm wavelength.

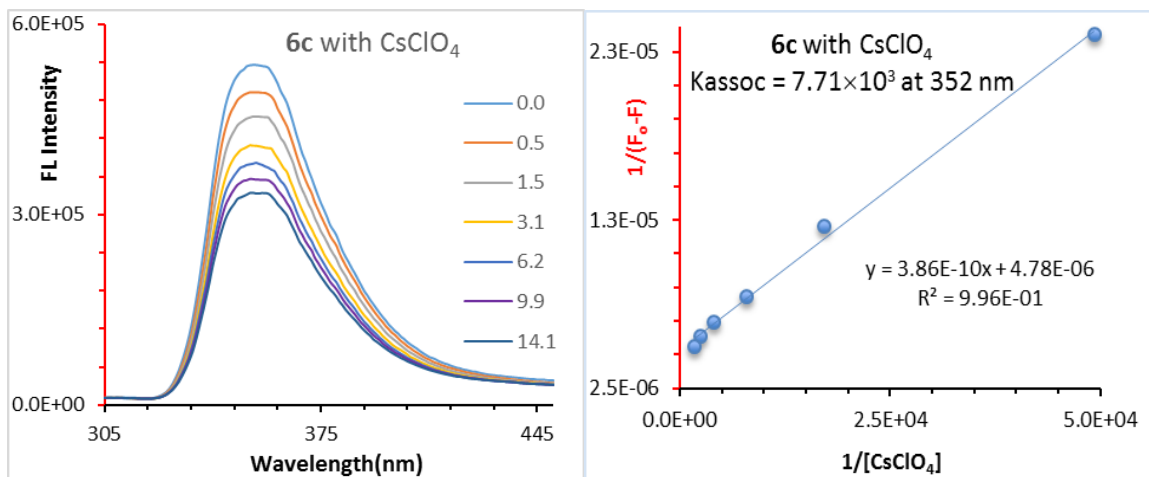


**Figure 4-35.** *Left:* Fluorescence response of chemosensor **6c** (1.50  $\mu\text{M}$ ) to various equivalents of  $\text{CsClO}_4$  in acetonitrile/chloroform (v/v= 9:1) solutions. The excitation wavelength was  $\lambda$  291 nm. *Right:* Benesi-Hildebrand plot of  $1/(F_0-F)$  versus  $1/[\text{CsClO}_4]$  for **6c** upon titration with  $\text{CsClO}_4$  (0-14.1 equivalents). The linear fit showed a 1:1 complexation between **6c** and  $\text{Cs}^+$  ions. The association constant was calculated at 352 nm wavelength.

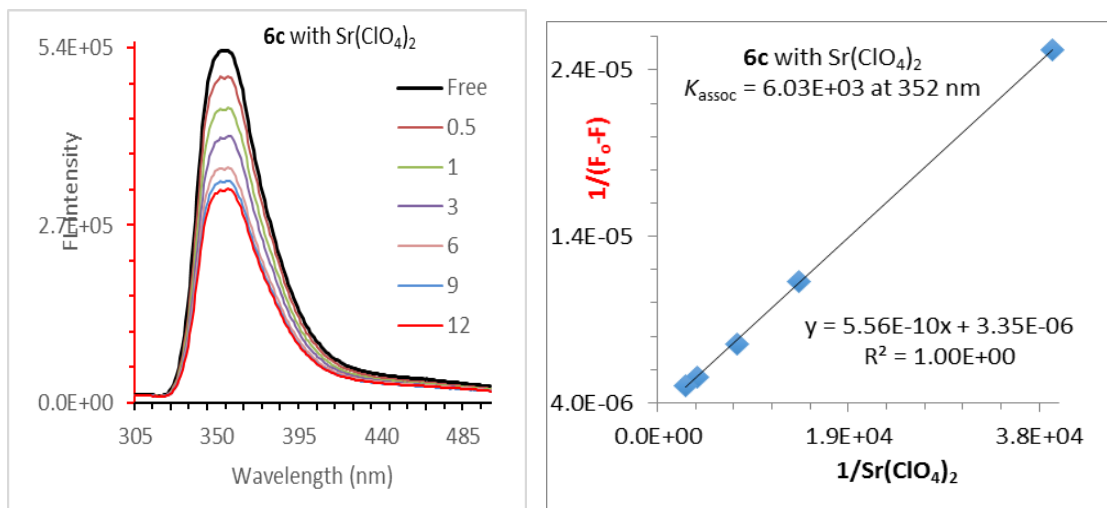


**Figure 4-36.** *Left:* Fluorescence response of chemosensor **6c** (1.50 μM) to various equivalents of Sr(ClO<sub>4</sub>)<sub>2</sub> in acetonitrile/chloroform (v/v= 9:1) solutions. The excitation wavelength was λ 291 nm. *Right:* Benesi-Hildebrand plot of 1/(F<sub>0</sub>-F) versus 1/[Sr(ClO<sub>4</sub>)<sub>2</sub>] for **6c** upon titration with Sr(ClO<sub>4</sub>)<sub>2</sub> (0-12 equivalents). The linear fit showed a 1:1 complexation between **6c** and Sr<sup>2+</sup> ions. The association constant was calculated at 352 nm wavelength.

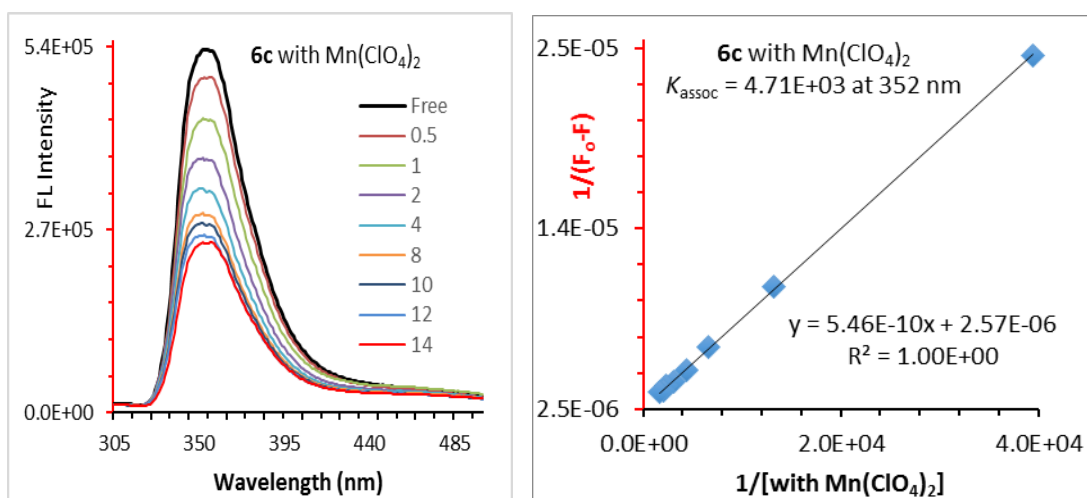


**Figure 4-37.** *Left:* Fluorescence response of chemosensor **6c** (1.50 μM) to various equivalents of Mn(ClO<sub>4</sub>)<sub>2</sub> in acetonitrile/chloroform (v/v= 9:1) solutions. The excitation wavelength was λ 291 nm. *Right:* Benesi-Hildebrand plot of 1/(F<sub>0</sub>-F) versus 1/[Mn(ClO<sub>4</sub>)<sub>2</sub>] for **6c** upon titration with Mn(ClO<sub>4</sub>)<sub>2</sub> (0-14 equivalents). The linear fit showed a 1:1 complexation between **6c** and Mn<sup>2+</sup> ions. The association constant was calculated at 352 nm wavelength.

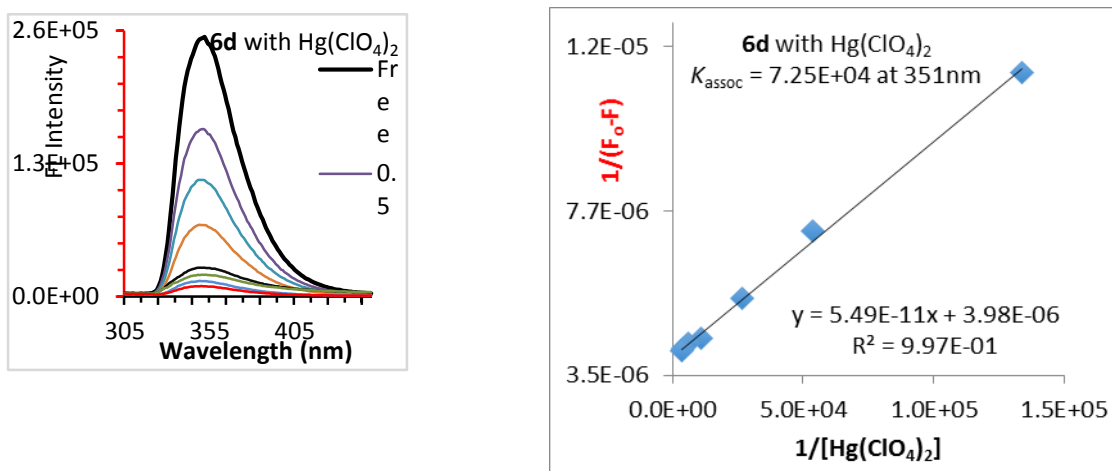


**Figure 4-38.** *Left:* Fluorescence response of chemosensor **6d** (1.50  $\mu\text{M}$ ) to various equivalents of  $\text{Hg}(\text{ClO}_4)_2$  in acetonitrile/chloroform (v/v= 9:1) solutions. The excitation wavelength was  $\lambda$  291 nm. *Right:* Benesi-Hildebrand plot of  $1/(F_0 - F)$  versus  $1/[\text{Hg}(\text{ClO}_4)_2]$  for **6d** upon titration with  $\text{Hg}(\text{ClO}_4)_2$  (0-14 equivalents). The linear fit showed a 1:1 complexation between **6d** and  $\text{Hg}^{2+}$  ions. The association constant was calculated at 351 nm wavelength.

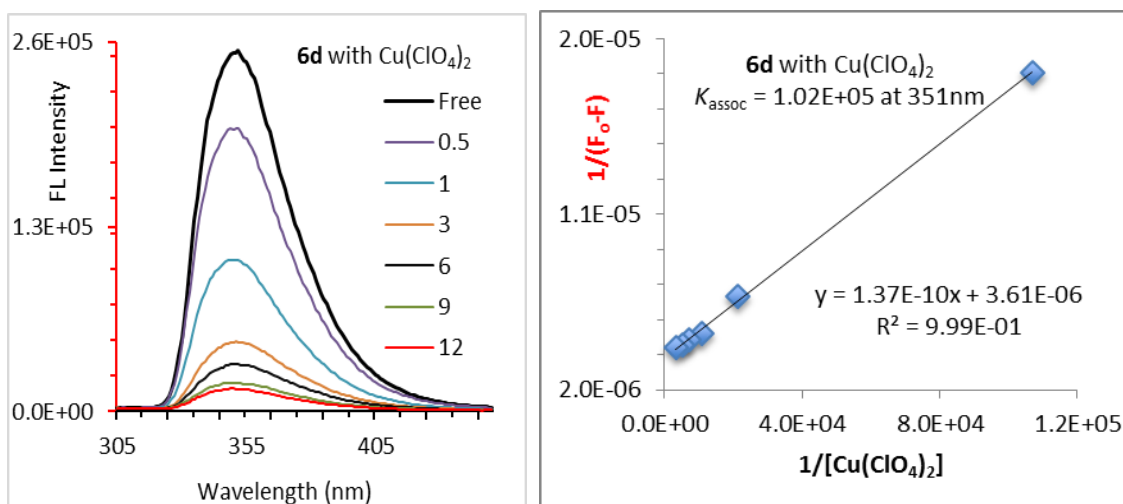


**Figure 4-39.** *Left:* Fluorescence response of chemosensor **6d** (1.50  $\mu\text{M}$ ) to various equivalents of  $\text{Cu}(\text{ClO}_4)_2$  in acetonitrile/chloroform (v/v= 9:1) solutions. The excitation wavelength was  $\lambda$  291 nm. *Right:* Benesi-Hildebrand plot of  $1/(F_0 - F)$  versus  $1/[\text{Cu}(\text{ClO}_4)_2]$  for **6d** upon titration with  $\text{Cu}(\text{ClO}_4)_2$  (0-12 equivalents). The linear fit showed a 1:1 complexation between **6d** and  $\text{Cu}^{2+}$  ions. The association constant was calculated at 351 nm wavelength.

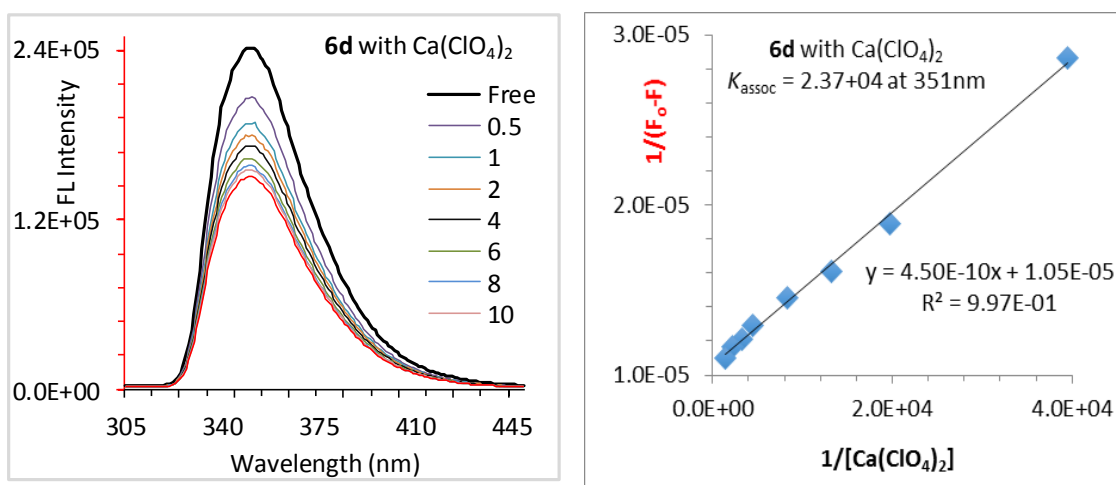


**Figure 4-40.** *Left:* Fluorescence response of chemosensor **6d** (1.50 μM) to various equivalents of  $\text{Ca}(\text{ClO}_4)_2$  in acetonitrile/chloroform (v/v= 9:1) solutions. The excitation wavelength was  $\lambda$  291 nm. *Right:* Benesi-Hildebrand plot of  $1/(F_0-F)$  versus  $1/[\text{Ca}(\text{ClO}_4)_2]$  for **6d** upon titration with  $\text{Ca}(\text{ClO}_4)_2$  (0-10 equivalents). The linear fit showed a 1:1 complexation between **6d** and  $\text{Ca}^{2+}$  ions. The association constant was calculated at 351 nm wavelength.

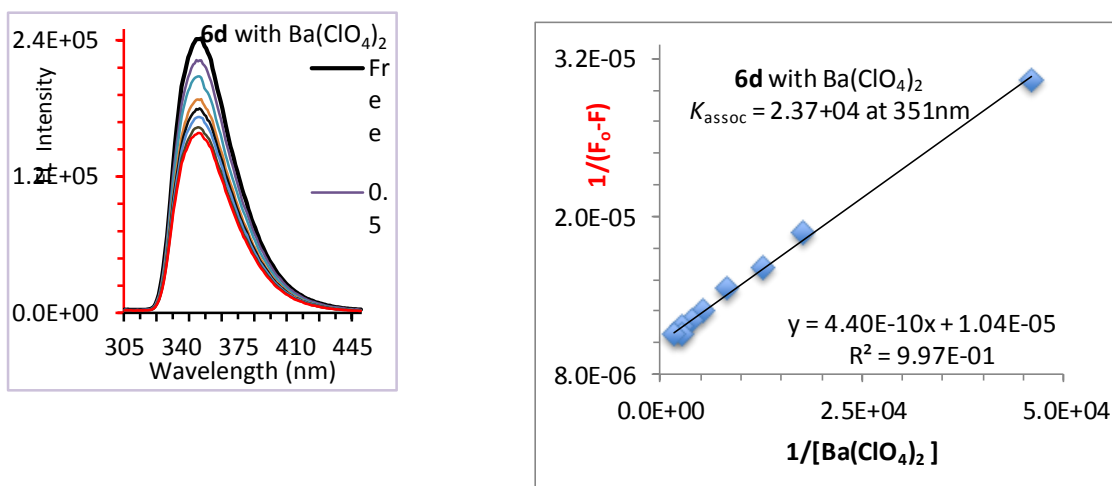


**Figure 4-41.** *Left:* Fluorescence response of chemosensor **6d** (1.50 μM) to various equivalents of  $\text{Ba}(\text{ClO}_4)_2$  in acetonitrile/chloroform (v/v= 9:1) solutions. The excitation wavelength was  $\lambda$  291 nm. *Right:* Benesi-Hildebrand plot of  $1/(F_0-F)$  versus  $1/[\text{Ba}(\text{ClO}_4)_2]$  for **6d** upon titration with  $\text{Ba}(\text{ClO}_4)_2$  (0-14 equivalents). The linear fit showed a 1:1 complexation between **6d** and  $\text{Ba}^{2+}$  ions. The association constant was calculated at 351 nm wavelength.

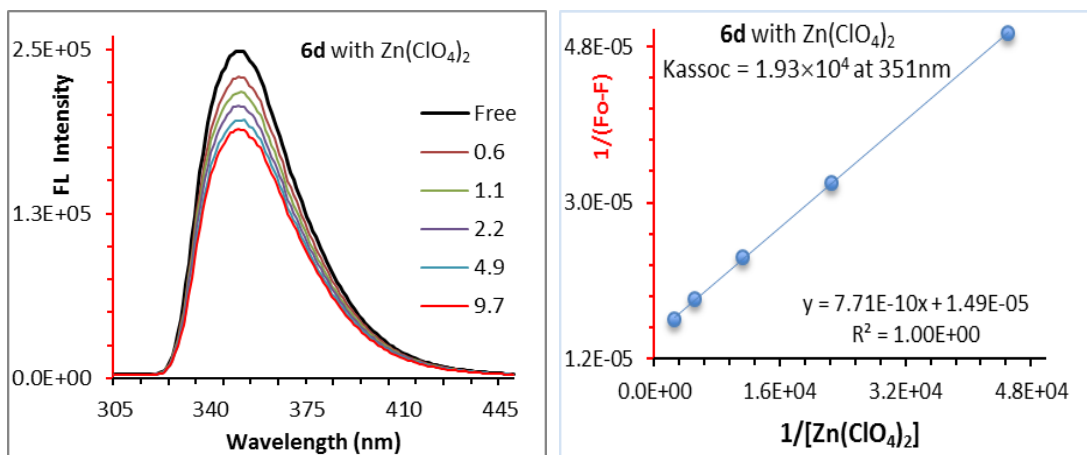


**Figure 4-42.** *Left:* Fluorescence response of chemosensor **6d** (1.50  $\mu\text{M}$ ) to various equivalents of  $\text{Zn}(\text{ClO}_4)_2$  in acetonitrile/chloroform (v/v= 9:1) solutions. The excitation wavelength was  $\lambda$  291 nm. *Right:* Benesi-Hildebrand plot of  $1/(F_0-F)$  versus  $1/[\text{Zn}(\text{ClO}_4)_2]$  for **6d** upon titration with  $\text{Zn}(\text{ClO}_4)_2$  (0-9.7 equivalents). The linear fit showed a 1:1 complexation between **6d** and  $\text{Zn}^{2+}$  ions. The association constant was calculated at 351 nm wavelength.

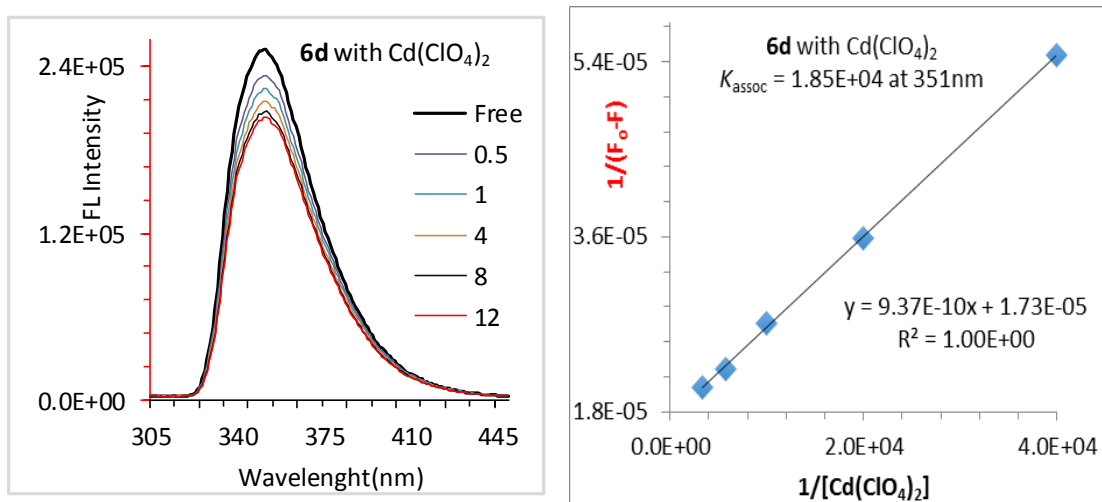


**Figure 4-43.** *Left:* Fluorescence response of chemosensor **6d** (1.50  $\mu\text{M}$ ) to various equivalents of  $\text{Cd}(\text{ClO}_4)_2$  in acetonitrile/chloroform (v/v= 9:1) solutions. The excitation wavelength was  $\lambda$  291 nm. *Right:* Benesi-Hildebrand plot of  $1/(F_0-F)$  versus  $1/[\text{Cd}(\text{ClO}_4)_2]$  for **6d** upon titration with  $\text{Cd}(\text{ClO}_4)_2$  (0-12 equivalents). The linear fit showed a 1:1 complexation between **6d** and  $\text{Cd}^{2+}$  ions. The association constant was calculated at 351 nm wavelength.

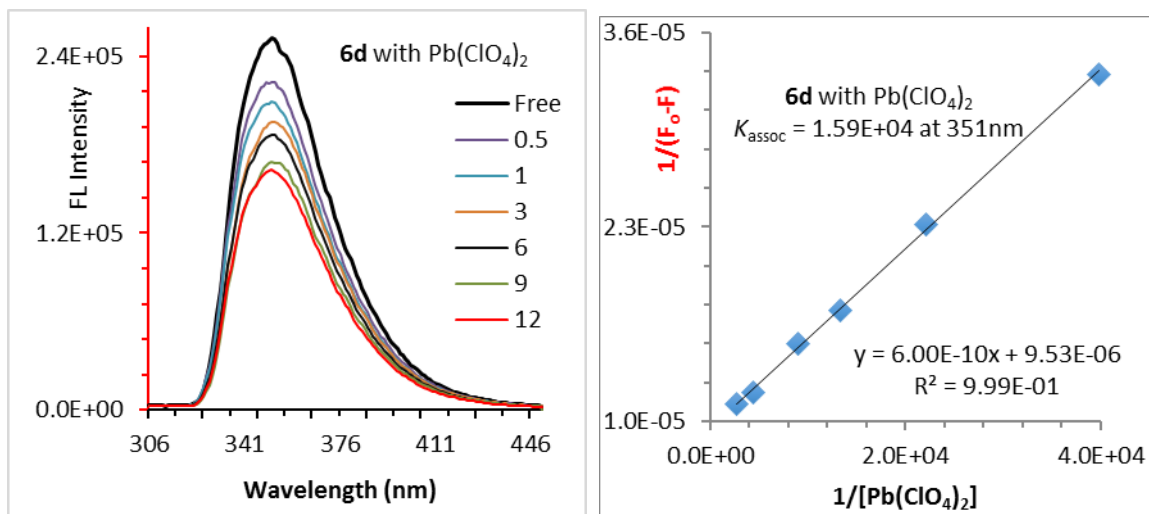


**Figure 4-44.** *Left:* Fluorescence response of chemosensor **6d** (1.50 μM) to various equivalents of  $\text{Pb}(\text{ClO}_4)_2$  in acetonitrile/chloroform (v/v= 9:1) solutions. The excitation wavelength was  $\lambda$  291 nm. *Right:* Benesi-Hildebrand plot of  $1/(F_0-F)$  versus  $1/[\text{Pb}(\text{ClO}_4)_2]$  for **6d** upon titration with  $\text{Pb}(\text{ClO}_4)_2$  (0-12 equivalents). The linear fit showed a 1:1 complexation between **6d** and  $\text{Pb}^{2+}$  ions. The association constant was calculated at 351 nm wavelength.

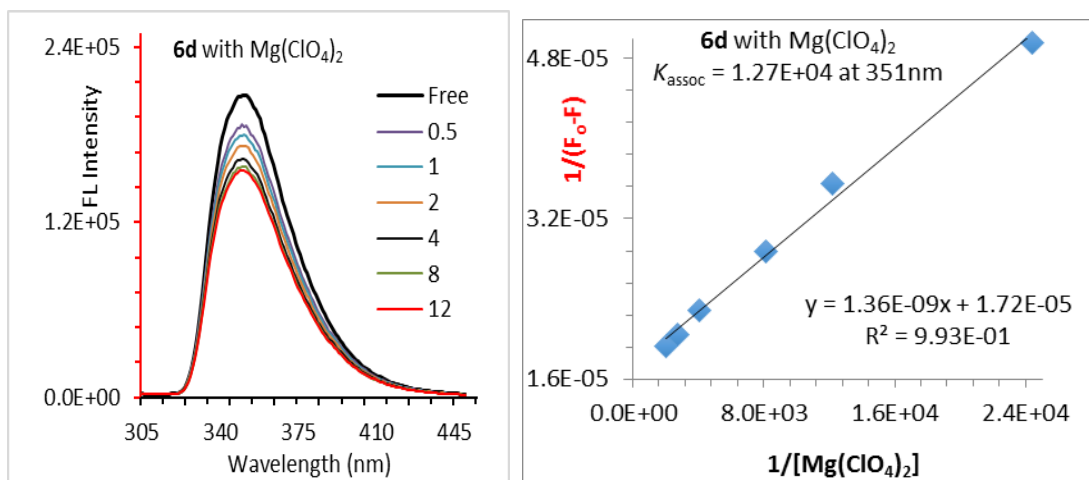


**Figure 4-45.** *Left:* Fluorescence response of chemosensor **6d** (1.50 μM) to various equivalents of  $\text{Mg}(\text{ClO}_4)_2$  in acetonitrile/chloroform (v/v= 9:1) solutions. The excitation wavelength was  $\lambda$  291 nm. *Right:* Benesi-Hildebrand plot of  $1/(F_0-F)$  versus  $1/[\text{Mg}(\text{ClO}_4)_2]$  for **6d** upon titration with  $\text{Mg}(\text{ClO}_4)_2$  (0-12 equivalents). The linear fit showed a 1:1 complexation between **6d** and  $\text{Mg}^{2+}$  ions. The association constant was calculated at 351 nm wavelength.

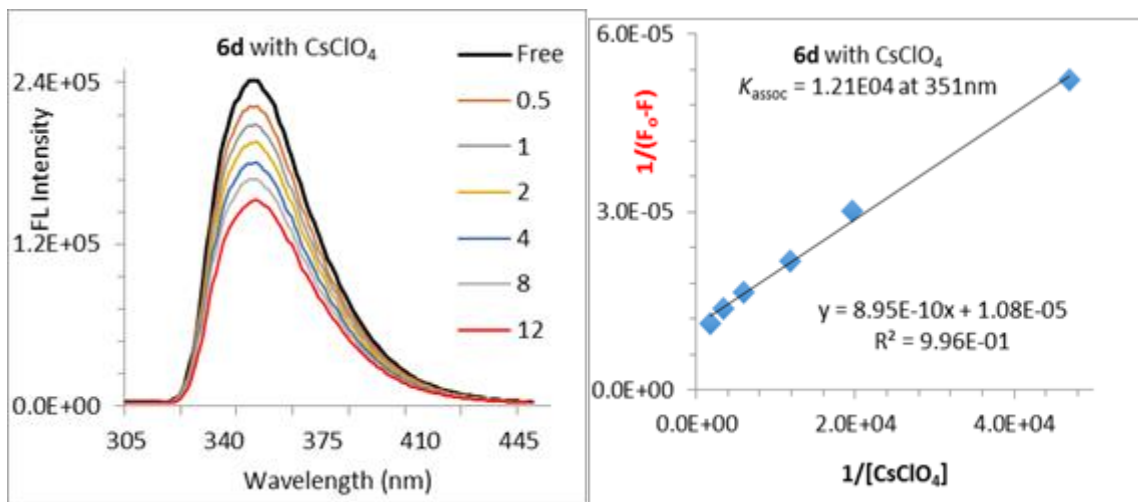


**Figure 4-46.** *Left:* Fluorescence response of chemosensor **6d** (1.50  $\mu\text{M}$ ) to various equivalents of  $\text{CsClO}_4$  in acetonitrile/chloroform (v/v= 9:1) solutions. The excitation wavelength was  $\lambda$  291 nm. *Right:* Benesi-Hildebrand plot of  $1/(F_0-F)$  versus  $1/[\text{CsClO}_4]$  for **6d** upon titration with  $\text{CsClO}_4$  (0-12 equivalents). The linear fit showed a 1:1 complexation between **6d** and  $\text{Cs}^+$  ions. The association constant was calculated at 351 nm wavelength.

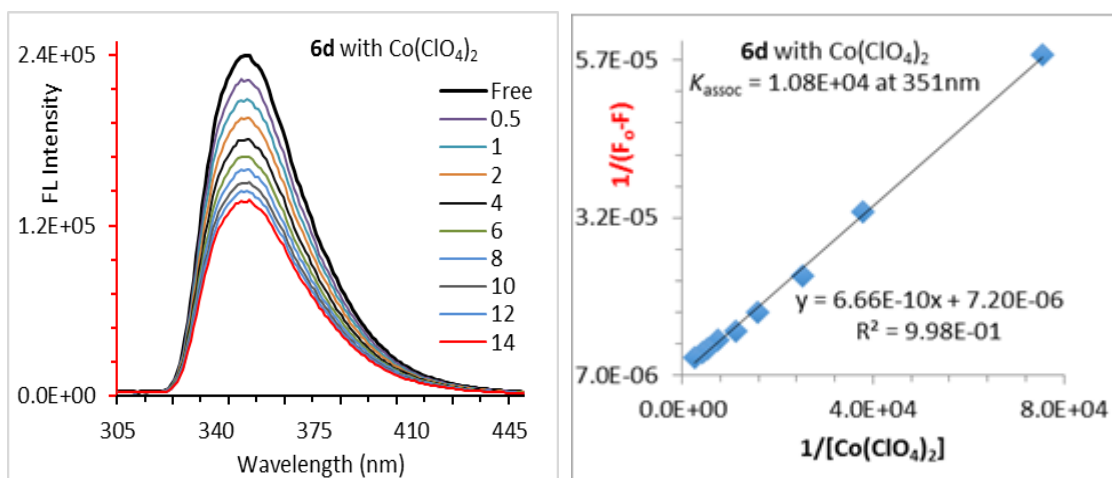


**Figure 4-47.** *Left:* Fluorescence response of chemosensor **6d** (1.50  $\mu\text{M}$ ) to various equivalents of  $\text{Co}(\text{ClO}_4)_2$  in acetonitrile/chloroform (v/v= 9:1) solutions. The excitation wavelength was  $\lambda$  291 nm. *Right:* Benesi-Hildebrand plot of  $1/(F_0-F)$  versus  $1/[\text{Co}(\text{ClO}_4)_2]$  for **6d** upon titration with  $\text{Co}(\text{ClO}_4)_2$  (0-14 equivalents). The linear fit showed a 1:1 complexation between **6d** and  $\text{Co}^{2+}$  ions. The association constant was calculated at 351 nm wavelength.

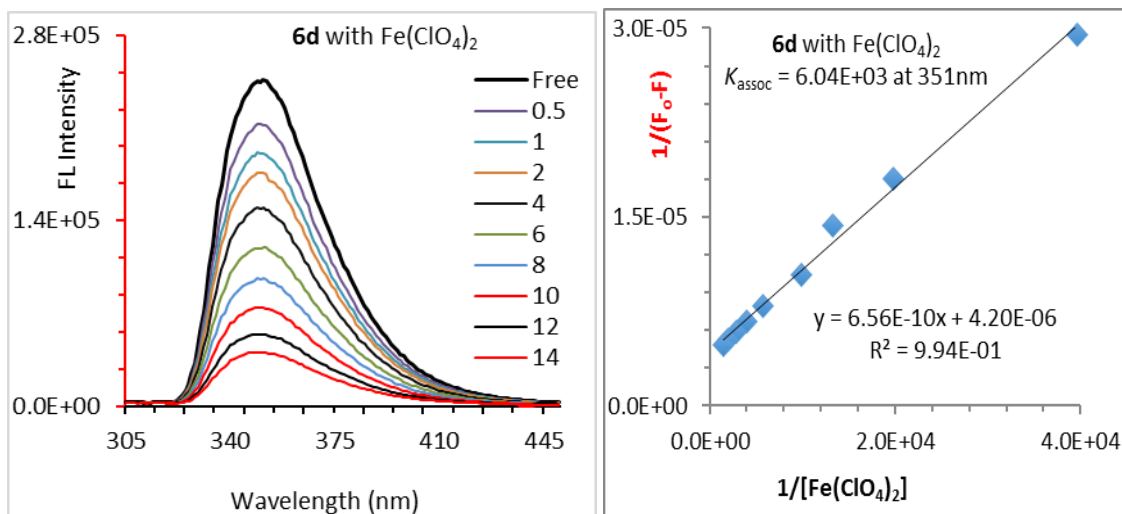


**Figure 4-48.** *Left:* Fluorescence response of chemosensor **6d** (1.50 μM) to various equivalents of Fe(ClO<sub>4</sub>)<sub>2</sub> in acetonitrile/chloroform (v/v= 9:1) solutions. The excitation wavelength was λ 291 nm. *Right:* Benesi-Hildebrand plot of 1/(F<sub>0</sub>-F) versus 1/[Fe(ClO<sub>4</sub>)<sub>2</sub>] for **6d** upon titration with Fe(ClO<sub>4</sub>)<sub>2</sub> (0-14 equivalents). The linear fit showed a 1:1 complexation between **6d** and Fe<sup>2+</sup> ions. The association constant was calculated at 351 nm wavelength.

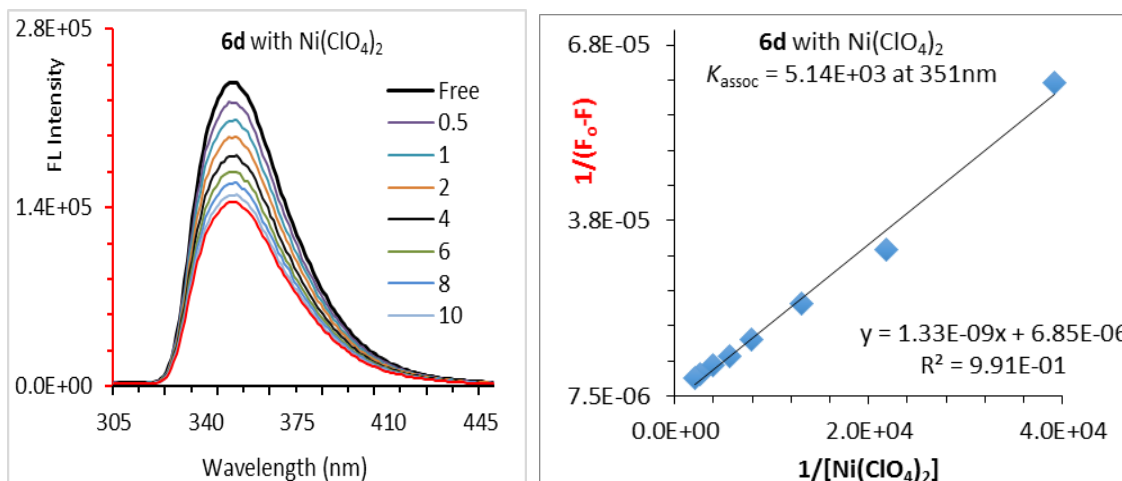


**Figure 4-49.** *Left:* Fluorescence response of chemosensor **6d** (1.50 μM) to various equivalents of Ni(ClO<sub>4</sub>)<sub>2</sub> in acetonitrile/chloroform (v/v= 9:1) solutions. The excitation wavelength was λ 291 nm. *Right:* Benesi-Hildebrand plot of 1/(F<sub>0</sub>-F) versus 1/[Ni(ClO<sub>4</sub>)<sub>2</sub>] for **6d** upon titration with Ni(ClO<sub>4</sub>)<sub>2</sub> (0-10 equivalents). The linear fit showed a 1:1 complexation between **6d** and Ni<sup>2+</sup> ions. The association constant was calculated at 351 nm wavelength.

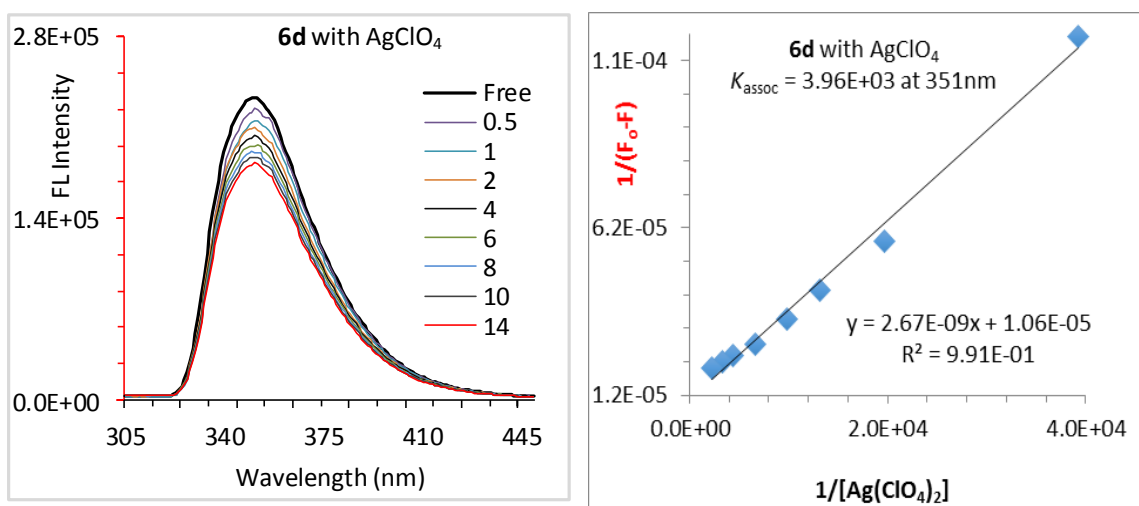


**Figure 4-50.** *Left:* Fluorescence response of chemosensor **6d** (1.50  $\mu\text{M}$ ) to various equivalents of  $\text{AgClO}_4$  in acetonitrile/chloroform (v/v= 9:1) solutions. The excitation wavelength was  $\lambda$  291 nm. *Right:* Benesi-Hildebrand plot of  $1/(F_0 - F)$  versus  $1/[\text{AgClO}_4]$  for **6d** upon titration with  $\text{AgClO}_4$  (0-14 equivalents). The linear fit showed a 1:1 complexation between **6d** and  $\text{Ag}^+$  ions. The association constant was calculated at 351 nm wavelength.

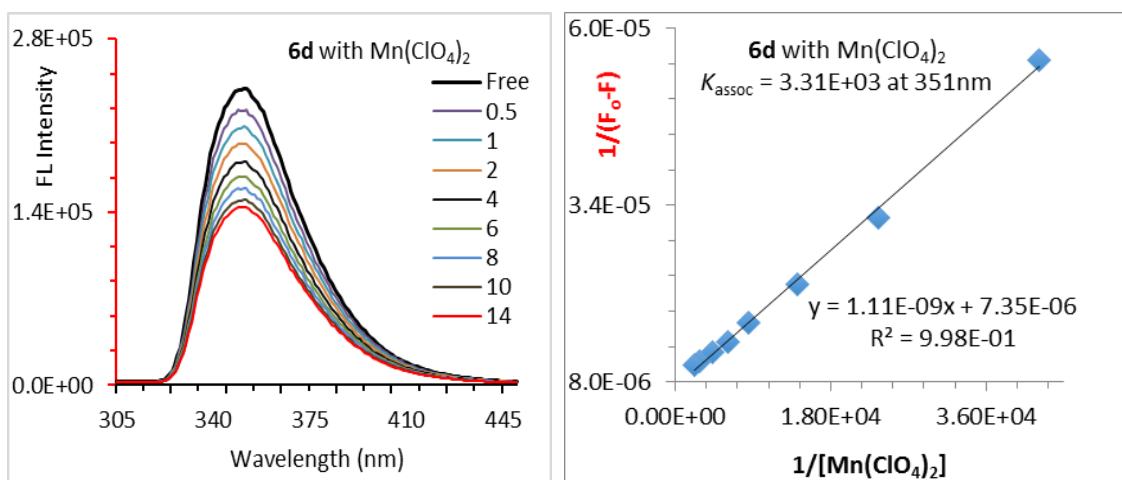


**Figure 4-51.** *Left:* Fluorescence response of chemosensor **6d** (1.50  $\mu\text{M}$ ) to various equivalents of  $\text{Mn}(\text{ClO}_4)_2$  in acetonitrile/chloroform (v/v= 9:1) solutions. The excitation wavelength was  $\lambda$  291 nm. *Right:* Benesi-Hildebrand plot of  $1/(F_0 - F)$  versus  $1/[\text{Mn}(\text{ClO}_4)_2]$  for **6d** upon titration with  $\text{Mn}(\text{ClO}_4)_2$  (0-14 equivalents). The linear fit showed a 1:1 complexation between **6d** and  $\text{Mn}^{2+}$  ions. The association constant was calculated at 351 nm wavelength.